LIQUID-MEDIATED ADHESION BETWEEN CONTACTING ROUGH SURFACES

A Dissertation
Presented to
The Academic Faculty

by

Amir Rostami

In Partial Fulfillment
of the Requirements for the Degree
Doctor of Philosophy in the
George W. Woodruff School of Mechanical Engineering

Georgia Institute of Technology
May 2017

LIQUID-MEDIATED ADHESION BETWEEN CONTACTING ROUGH SURFACES

Approved by:

Dr. Jeffrey L. Streator, Advisor
School of Mechanical Engineering
Georgia Institute of Technology

Dr. Scott Bair
School of Mechanical Engineering
Georgia Institute of Technology

Dr. Itzhak Green
School of Mechanical Engineering
Georgia Institute of Technology

Dr. Robert L. Jackson
School of Mechanical Engineering
Auburn University

Dr. Michael Varenberg
School of Mechanical Engineering
Georgia Institute of Technology

Date Approved: January 9th 2017

This thesis is dedicated to my beloved family.

ACKNOWLEDGEMENTS

This Ph.D. thesis is developed during working on the project entitled “Liquid-Mediated Adhesion: Forces and Flows” sponsored by the National Science Foundation (NSF) of the United States. I began working on this project in August 2013 along with my Ph.D. studies in mechanical engineering under the supervision of Dr. Jeffery L. Streator at Georgia Institute of Technology.

First of all, I would like to thank Dr. Streator who helped me significantly during my Ph.D. studies, and I’ve benefited from his suggestions and ideas countlessly during the course of the project. He has been completely involved in every step of the project and decisions made during the course of the project. I would also like to thank Dr. Scott Bair, Dr. Itzhak Green, Dr. Robert L. Jackson, and Dr. Michael Varenberg for serving on my thesis committee and for their constructive comments and suggestions. Thanks also goes to the tribology research group at Georgia Institute of Technology for their friendship and support and many shared laughs and hard work.

I should mention the support and encouragement of the most important people in my life, my parents, which of course they are far away from me, but, they have always been close to me in my heart.

TABLE OF CONTENTS

LIST OF TABLES

LIST OF FIGURES

LIST OF SYMBOLS AND ABBREVIATIONS

a	Radius of pressurized region
A_w	Wetted area
A_k	Contact area of an asperity at frequency scale k
b	Liquid film radius
b_0	Initial liquid film radius
C_{ij}	Influence coefficients
Δ_k	Amplitude of sinusoidal asperity at frequency scale k
Δg_k	Reduction in the average surface separation at frequency scale k
Δp	Capillary pressure drop
Δr	Grid spacing in r direction
Δt	Time step
ΔV_{loss-c}	Volume loss due to compressive stresses
ΔV_{loss-t}	Volume loss due to tensile stresses
E	Elastic modulus
E^*	Reduced or effective elastic modulus
E_c	Complete elliptic integral of the second kind
η	Dynamic viscosity of the liquid film
η_k	Areal density of asperities at frequency scale k
F_c	Compressive force
F_f	Friction force
F_t	Tensile force
$F_{t\max}$	Maximum tensile force
$F(k_x, k_y)$	2D FFT coefficients

f_k	Spatial frequency (reciprocal of wavelength)
φ	Transverse pressure flow factor
g	Acceleration of gravity
$\overline{g}_k$	Average surface separation at frequency scale k
γ	Surface tension of liquid film
$h(r)$	Liquid film thickness or average spacing at each radial location
h_b	Liquid film thickness at the free surface
h_{ave}	Average film thickness within the wetted region
K_c	Complete elliptic integral of the first kind
$k_{x,y}$	Indices correspond to spatial frequencies in x and y directions
l	Free surface location in capillary tube
$L_{x,y}$	Scan lengths in x and y directions
λ_k	Wavelength of sinusoidal asperity at frequency scale k
$n_{x,y}$	Indices correspond to spatial coordinate in x and y directions
$N_{x,y}$	Number of nodal points in x and y directions
υ	Poisson's ratio
p	Pressure
p_f	Liquid film pressure
p_{ext}	Pressure due to external load
$\overline{p}_k$	Average contact pressure of an asperity at frequency scale k
p_k^*	Complete contact pressure of an asperity at frequency scale k
p'	Normalized pressure
P_{ext}	External load
Q	Liquid flow rate

Q_{avg}	Average liquid flow rate
ρ	Liquid film density
r	Radial coordinate
r'	Normalized radial coordinate
r_e	Edge radius
R	Capillary tube radius
R_1	Inner radius of the rigid flat surface
R_2	Outer radius of the rigid flat surface
$R_{I,II}$	Principal radii of curvature at the free surface of the liquid
σ	Root mean square of rough surface heights
u	Surface deformation
u_t	Surface deformation due to tensile stresses
v_r	Radial velocity
$\bar{v}_r$	Average radial velocity
t	Time scale
$\theta_{A,B}$	Contact angles between the liquid and the contacting surfaces
z	Surface heights
$z_{\max}$	Maximum surface height

SUMMARY

Surface forces become important at small scales due to the small spacing present and high surface area to volume ratio. Liquid-mediated adhesion is defined as the adhesion between two solid surfaces in contact or close proximity in the presence of liquid film. Familiar examples in nature include: plants, which transport fluid from roots to leaves in opposition of gravity through xylem conduits, and soils whose strength characteristics depend on the way water interacts between solid particles. Among engineering systems, there are several small scale devices such as nano/micro-electro-mechanical devices (NEMS/MEMS), magnetic storage head/disk interface (HDI), the tip of atomic force microscope (AFM) for which liquid films are present in confined regions during fabrication or during operation due to condensation (humid environment), contamination, or lubrication. In many small-scale devices, the presence of the liquid film causes excessive adhesive or friction forces, and "stiction" happens. Stiction is one of the main causes of the failure in these devices. On the positive side, in the operation of nanofluidic devices, capillary forces operating in submicron channels are used to pump liquids from one location to another.

In this study, a liquid film within the confined region defined by the interface between contacting elastic rough surfaces is considered. The wetting liquid film entrapped within the small spacing between the contacting surfaces possess large concave curvatures at the free surface, which in turn, causes large pressure drop across the free surface. The pressure drop can be quantified using the Laplace-Young relation. This pressure drop induces tensile stresses between the contacting surfaces, which leads to

reduction in spacing between the surfaces. Opposing these tensile stresses, are the compressive stresses developed at solid-solid contact spots. The interaction between these tensile and compressive stresses are studied both numerically and experimentally under static equilibrium condition and during capillary-driven flow.

CHAPTER 1

INTRODUCTION

1.1 Problem Motivation

Liquid-mediated adhesion or adhesion due to the wetting of solid-solid interfaces often arises in small scale devices, where the liquid film is interposed between two solids in close proximity. In small-scale devices such as nano/micro-electromechanical systems (NEMS/MEMS), magnetic storage head/disk interface (HDI), and the tip of atomic force microscope (AFM) [1-7], a liquid film could be present in confined regions during fabrication or during operation (see Fig. 1.1). Fig. 1.1a shows a liquid droplet bridging the gap between the tip of atomic force microscopy and the measured surface. Fig. 1.1b depicts a magnetic head-disk interface (HDI) and reveals a wear track that could be induced by excessive adhesion force caused by the presence of liquid film. A potential failure caused by large adhesive forces between surfaces in microelectromechanical system (MEMS) is shown in Fig. 1.1c. In many cases, the presence of liquid film causes excessive adhesive forces and device failure [8-14]. For instance, the well-known problem of high adhesion (stiction) in microelectromechanical systems (MEMS) and head/disk interface (HDI) largely depends on the forces induced by the presence of a thin liquid film [13,14]. Under certain conditions, the elastic surfaces of these devices may adhere together permanently and cause device failure.

The interfacial liquid film could be present in these devices due to condensation, contamination, or lubrication. It would be beneficial to engineers of micro-devices to have a comprehensive mathematical model for the interaction between liquid film and elastically deforming rough surfaces in contact. It would be valuable to understand how

mechanical equilibrium is achieved for such an interface and thereby be able to predict the magnitude of adhesive forces at equilibrium.

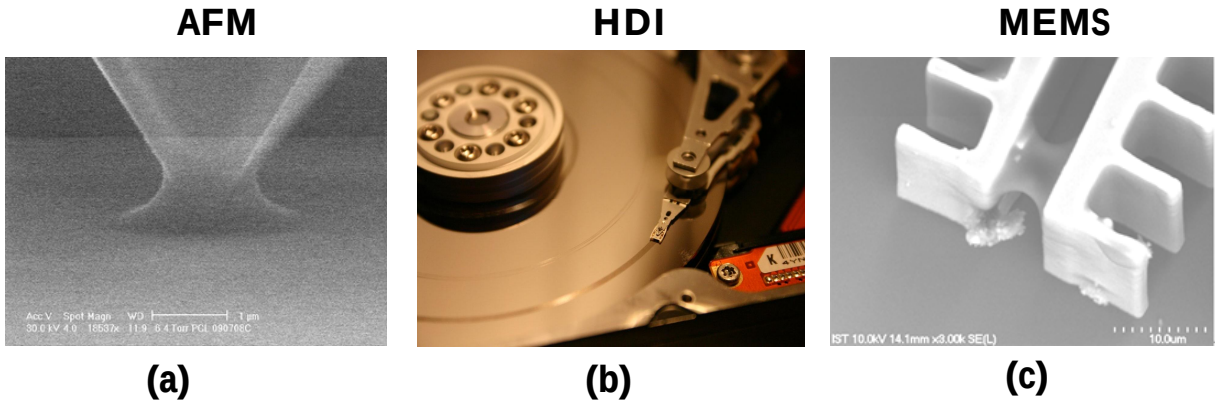

Fig. 1.1 Small-scale devices that are subject to liquid-mediated adhesion.

Liquid-mediated adhesion is also happens in natural systems (see Fig. 1.2). Examples include plants, which transport fluid from roots to leaves in opposition of gravity through xylem conduits (Fig. 1.2a). Soils whose strength characteristics depend on the way water interacts between solid particles (Fig. 1.2b). Adhesive pads of insects which allows them to walk on a vertical wall [15] (Fig. 1.2c). There pads could be hairy as are shown in the top three pictures in Fig. 1.2c or smooth as are shown in the bottom three pictures in Fig. 1.2c.

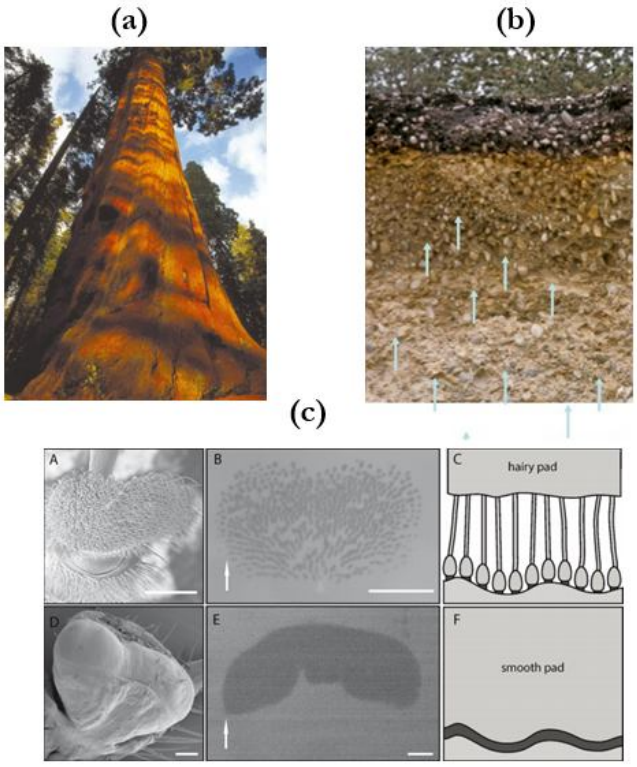

Fig. 1.2 Natural systems that are subject to liquid mediated adhesion.

The interaction between two surfaces in the presence of liquid film is considered in this work. The concentration is on the role of liquid film in regimes where gravitational effects are negligible, which corresponds to small vertical length scale. At micro and nano scales the surface forces tend to dominate the gravitational and inertial forces. This fact is readily seen by appealing to simple scaling arguments. Pressures arising from gravitational forces, for example, on a hemispherical droplet would be approximated by ρgR where, ρ is the mass density of the liquid, g is the acceleration of gravity and R is the droplet radius. On the other hand, the liquid, having surface tension γ, would experience a capillary pressure given approximately by $2\gamma / R$, so that the ratio of hydrostatic pressure to capillary pressure would be on the order of $\rho gR^2 / 2\gamma$. For a

$1\mu m$ radius droplet of water, with $\rho = 10^3 kg/m^3$ and $\gamma = 0.0727 mN/m$, this ratio takes on a value of 6.7×10^{-8}, or vanishingly small. Thus the micron and sub-micron realms are dominated by surface-driven effects, with gravity having essentially no influence.

1.2 Literature Review

The effect of liquid-mediated adhesion between surfaces is studied both numerically [16-40] and experimentally [41-48]. The previous numerical models on the liquid mediated can be categorized based on the gross interface geometry (flat or curved), surface topography (smooth or rough), structural properties (rigid or deforming), meniscus type (constant-volume or constant-pressure), and separating process (quasi-static or dynamic.

1.2.1 Previous Numerical Work

Zheng and Streator [16-18] modeled the interaction between two elastic smooth flat and spherical surfaces in the presence of fixed volume of liquid to investigate the interface stability. Matthewson and Mamin [19] modeled the liquid film adhesion between two elastic rough surfaces where different regimes were identified by differing the quantities of liquid between the surfaces. Persson [22] studied the effect of relative humidity (RH) on the work of adhesion and the contact area between two elastic solids with randomly rough surfaces. DelRio et al. [25] presented a model for the capillary adhesion between contacting micro-machined rough surfaces and the effect of plastic deformation and relative humidity (RH) were studied. De Boer and De Boer [28] considered both constant volume and constant pressure capillary adhesion between

different rigid geometries (spheres and flats). Marmur [33] calculated the capillary adhesion force between the rigid spherical, paraboloidal, and conical tips and a rigid flat surface numerically. Poon and Bhushan [34] presented a numerical contact model for the contact between three-dimensional rough surfaces in the presence of a liquid film. Tian and Bhushan [35] used the same approach to study the effect of ultra-thin liquid film on the static friction of rough surface contact. Streator [36] developed a model to account for the effect of an intervening capillary film on the friction force between a rigid, nominally flat, rough surface and an elastic flat. Streator and Jackson [37] and Streator [38] used spectral and deterministic approaches, respectively, to model the contact between 2D elastic rough surfaces in the presence of a liquid film. The tensile force between the surfaces due to liquid-mediated adhesion is calculated and a "surface collapse" phenomenon is observed in their work which corresponds to a sudden jump in the tensile force between the surfaces. Streator [39] presented a model for the separation of a sphere from a flat in a fully flooded with the focus on the point of separation. Cai and Bhushan [40] investigated the dynamic separation of rigid rough surfaces in the presence of liquid film considering both meniscus and viscous effects.

1.2.2 Previous Experimental Work

There has been a lot of experimental study on the liquid-mediated adhesion between contacting surfaces [41-51]. Bhushan and Dugger [41] measured the adhesive force between magnetic heads and thin film disks under different environmental conditions. The adhesion forces between a smooth spherical particle and flat surfaces of alumina, silver, and titanium-coated Si wafers were measured with an atomic force microscope (AFM) under various humidity conditions are measured by Ata et al. [49].

Yang et al. [42] used atomic force microscope (AFM) to measure the pull-off force between a nano-scale AFM tip and a silicon wafer in air and in ultrahigh vacuum (UHV). Xiao and Qian [50] have measured the adhesion force as a function of humidity for SiO2 and OTE/SiO2 against an AFM Si3N4 tip. Nosonovsky and Bhushan [44] showed experimentally several examples of instabilities during liquid-mediated adhesion in nano scales. Rabinovich et al. [45-47] verified the results of a simple theoretical model through the measurements of capillary force between glass microspheres and silica substrates.

1.2.3 Deficiency in Literature

Despite the ample theoretical and experimental work on liquid-mediated adhesion, very little work has been performed considering (1) the liquid-mediated adhesion between contacting rough surfaces, and (2) the capillary-driven flow between contacting rough surfaces. Thus, there is a need to develop numerical models to predict the behavior of the contact interface for these cases, and to study the effect of different material and geometrical properties on the liquid-mediated adhesion.

1.3 Problem Statement

In this work, liquid-mediated adhesion between two contacting rough surfaces is studied both numerically and experimentally. Numerical models are developed for the interaction between tensile and compressive stresses, and to investigate the role of different material and geometrical properties on the liquid-mediated adhesion between the two surfaces. The liquid-mediated adhesion model is presented under two different

conditions: (1) a static (no-flow) condition, and (2) a capillary-driven flow condition. Next, experiments are performed to validate the results of the numerical model.

For the static condition, a constant volume of liquid is introduced between the two contacting rough surfaces. A numerical algorithm is developed to model the interaction between tensile stresses caused by the presence of the liquid film and the compressive stresses developed at the solid-solid contact spots within the contact interface. The tensile force, average spacing, liquid film spread, and contact area between contacting rough surfaces for different material and geometrical properties are calculated and studied. It is shown that, under certain conditions, a contact instability occurs leading to unbounded rates of change of tensile force, average gap, liquid film spread, and contact area. The effects of liquid volume, liquid surface tension, surface topography, nominal contact area, and external load on the stability of contact interface are studied. Key dimensionless ratios are identified that govern the equilibrium state and onset of instability.

Two different measurements are performed to assess the extent of liquid-mediated interfacial adhesion: (1) a pull-off test and (2) a friction force test. The results are compared with the results of previously developed numerical model. The pull-off test is performed by separating the two surfaces from contact in the normal direction. The force corresponding to the moment of separation is recorded as the pull-off force. The results are obtained for different material and geometrical properties. The friction force test is performed by applying a lateral force to the upper surface and measuring the friction force at the moment of initial slip. The areal coverage of the liquid film between the two contacting surfaces is also measured by collecting images of the contact interface using a digital camera and performing image processing on them.

For the capillary flow condition, a liquid film is introduced via a central hole between two contacting rough surfaces, which begins to flow between the rough surfaces due to pressure gradient inside the liquid film. The capillary pressure drop at the liquid film leading edge compared to the ambient pressure at the source (central hole) causes the liquid film to spread between the two surfaces. The liquid film continues to spread radially between the two surfaces until it reaches the edge of the contact or the supply of liquid is depleted. An iterative numerical algorithm is developed to solve equations of elasticity, capillarity and lubrication simultaneously. The results are obtained for the liquid flow rate, tensile force, and average spacing versus time as the liquid film spreads between the two surfaces.

To validate the results of the numerical model, an experimental setup is developed to visualize the liquid film spread between the contacting surfaces as a function of time. A digital camera collects images of the interfacial liquid film during its spreading. The time-stamped images provide a record of the rate of spread of the liquid, which can be compared to model predictions.

CHAPTER 2

LIQUID MEDIATED ADHESION: STATIC CONDITION

The liquid-mediated adhesion between two contacting surfaces is now considered for the case that the liquid film is in static equilibrium. A constant volume of liquid is introduced between two contacting rough surfaces, where after the equilibrium, the liquid is in a static condition with uniform pressure throughout. The interaction between the tensile stresses induced by the liquid film and the compressive stresses developed at the solid-solid contact spots is solved numerically. Two different contact models: 1. Spectral (multiscale) contact model and 2. Deterministic contact model are used to model the compressive stresses developed at solid-solid contact spots.

2.1 Spectral (Multiscale) Approach

In this approach, the contact model developed by Jackson and Streator (JS) [52] for the contact between two rough surfaces is used to determine the surface deformation developed at the solid-solid contact spots. The JS contact model is based on a multi-scale representation of compressive rough surface deformation, and it employs the Fourier series to decompose a rough surface into multiple scales of frequency.

Figure 2.1 shows, schematically, the interface of interest. It consists of a rough surface with nominal contact area having side length L in x and y directions ($A_n = L^2$) and with surface heights in z direction. A rigid flat surface (which is shown as transparent in Fig. 2.1) with the same nominal contact area deforms the rough surface in the presence of a liquid film bridging the two surfaces. It should be noted that the combination of a rigid flat and a rough surface used in this work is a model of two hypothetical elastic rough surfaces, whereby the rough surface of the model is given the combined roughness and flexibility of the hypothetical surface pair. It is well-known that if the liquid wets the two surfaces, a sub-ambient pressure will be developed within the liquid bridge which

induces tensile (adhesive) stresses between the two surfaces [53]. This pressure drop depends on the curvature at the free surface of the liquid film, and the curvature, in turn is inversely proportional to the local gap at the free surface of the liquid film. The thinner is the local gap, the greater is the pull effect between the two surfaces. As the surfaces are pulled together and the gap between them decreases, the more the liquid tends to pull them further together. As the surfaces are brought into closer proximity, the compressive stresses begin to rise at points of solid-solid contact. There are two potential scenarios [18, 19]: (1) the tensile and compressive forces come into balance with an average gap in the order of composite surface roughness, or (2) the tensile stresses dominate the compressive stresses, and the interface collapses such that the average gap is a very small fraction of composite surface roughness. Equations of elasticity and capillarity need to be solved, simultaneously, in order to predict the equilibrium configuration for the contact of rough surfaces in the presence of liquid film given the surface topography, elastic properties, liquid volume, liquid surface tension, and external load.

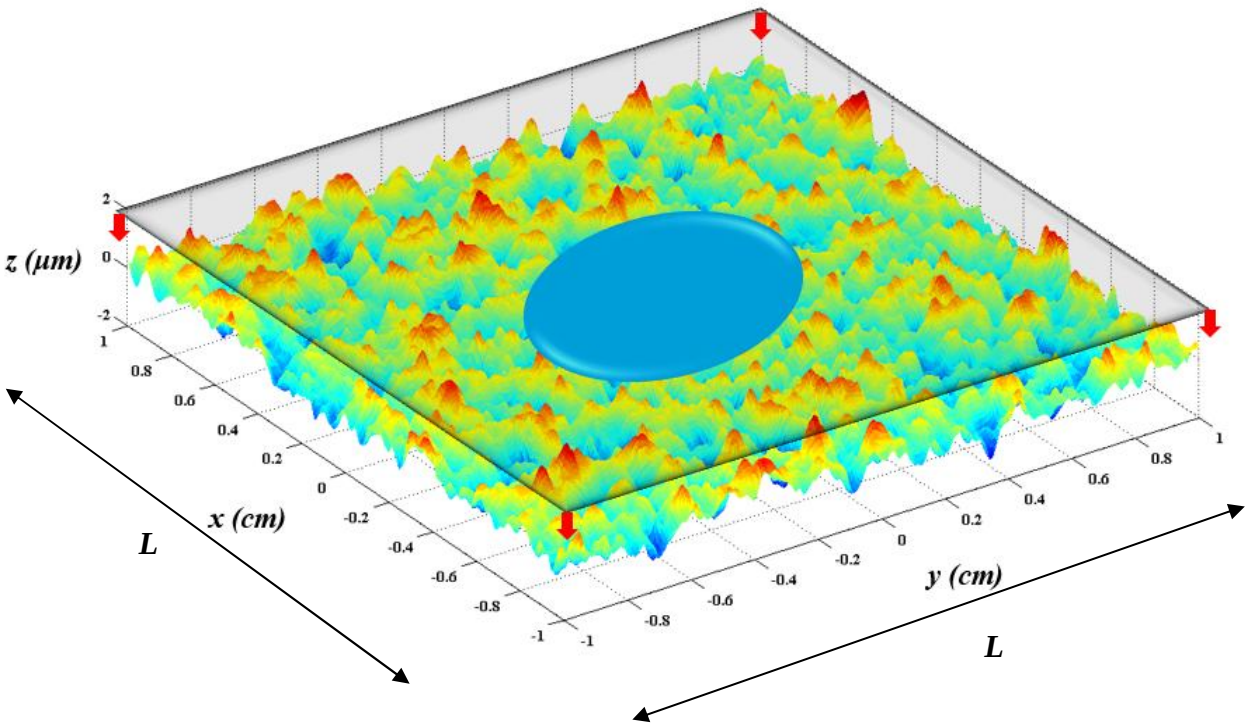

Fig. 2.1 Schematic depiction of the modeled interface: contact of a rigid flat surface and an elastic rough surface in the presence of a liquid film.

2.1.1 Tensile Stresses

As previously mentioned, a liquid film that wets the two contacting surfaces induces a pressure drop across the free surface. This pressure drop can be obtained based on the Laplace-Young equation (e.g. [53])

$$\Delta p = \gamma\left(\frac{1}{R_I} + \frac{1}{R_{II}}\right) \tag{2.1}$$

where Δp is the pressure drop across the free surface of liquid film, γ is the liquid film surface tension, $R_{I,II}$ are the principal radii of curvature at the free surface of the liquid, as illustrated in Fig. 2.2. In this model, the effect of gravity is neglected and, due to

assumed continuity, the liquid film is in static equilibrium with uniform pressure throughout.

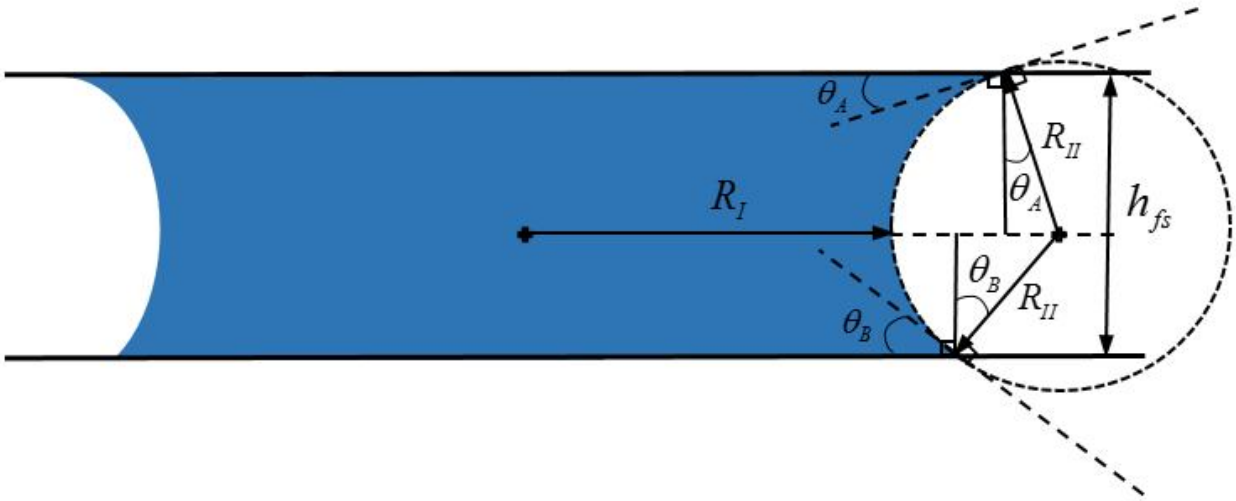

Fig. 2.2 The free surface of the liquid along with radii of curvature and the gap between the surfaces, which are depicted here as smooth and planar.

While Fig. 2.1 depicts an axisymmetric liquid film, in a real contact, the liquid film will assume a configuration that is consistent with maintaining a constant pressure throughout and with the local variations in surface height due to the surface topography. Thus the projection of the liquid film on the horizontal plane may deviate a bit from being circular. Nevertheless, for the purposes of the present study we assume a circular liquid film whose areal coverage is specified by a wetted radius. According to Fig. 2.2, setting $R_I = -r_w$ and $R_{II} = R$ in Eq. (2.1), we have

$$\Delta p = \gamma\left(\frac{1}{R} - \frac{1}{r_w}\right) \tag{2.2}$$

The assumption $R << r_w$ seems reasonable since the gap between the contacting surfaces at the free surface, h_{fs}, is expected to be very small (in the order of microns). Thus, we have

$$\Delta p = \frac{\gamma}{R} \tag{2.3}$$

Hence, according to Eq. (2.3), the radius of curvature is the same at any point along the free surface of the liquid. Therefore, the free surface at any cross section cut by a vertical plane is part of a circle (Fig. 2.2). The radius of curvature at the free surface, R, can be related to the gap at the free surface, h_{fs}, by

$$h_{fs} = R\left(\cos\theta_A + \cos\theta_B\right) \tag{2.4}$$

where $\theta_{A,B}$ are the contact angles of the liquid film with lower and upper surfaces, respectively. Now, replacing for R in Eq. (2.3) from Eq. (2.4), the following relation between the pressure drop and the gap at the free surface can be obtained

$$\Delta p = \frac{\gamma}{h_{fs}}\left(\cos\theta_A + \cos\theta_B\right) \tag{2.5}$$

To simplify the calculations, the average gap between the two rough surfaces in the wetted region, $\bar{h}$, will be used in the current work in place of h_{fs}. With this approximation, we have

$$\Delta p = \frac{\gamma}{\bar{h}}\left(\cos\theta_A + \cos\theta_B\right) \tag{2.6}$$

For convenience, the gage pressure is considered in this work. Relative to the ambient pressure, the liquid film pressure is then $-\Delta p$, which means that tensile stresses are

exerted on each of the opposing surfaces wherever in contact with the liquid film. In reality, the absolute value of the liquid film pressure is generally positive. Opposing the effects of these tensile stresses are the compressive stresses that are developed at the solid-solid contact points, which resist reduction in spacing between the two contacting surfaces.

2.1.2 Compressive Stresses

As the average gap between the two surfaces reduces due to tensile stresses induced by the liquid film, the asperities on the two surfaces further interact with each other and increase the extent of solid-solid contact. The elastic contact between the two rough surfaces is investigated using the multi-scale contact model developed by Jackson and Streator [52]. The JS model is based on representing the rough surface in multiple scale of roughness using a Fourier series. Thus, the surface profile is divided into different scales of frequency, and the deformation of each spectral component is calculated separately using an appropriate model for the contact of a single asperity. In this work, a sinusoidal shape is considered for the asperities at each frequency level. The analytical solutions of Johnson, Greenwood, and Higginson (JGH) [54] for early contact and near complete contact of sinusoidal asperities, and the empirical equation developed by Jackson and Streator [52] for contact area, along with the surface separation relations developed by Rostami and Jackson [55] are used in the framework of the JS model to solve the contact problem.

2.1.2.1 Single sinusoidal asperity contact

The current analysis uses the same sinusoidal shape used in Johnson, Greenwood, and Higginson (JGH) [54] for the asperity. The shape is described by

$$h = \Delta\left(1-\cos\left(\frac{2\pi x}{\lambda}\right).\cos\left(\frac{2\pi y}{\lambda}\right)\right) \tag{2.7}$$

where h is the height of the points on the sinusoidal asperity from its base, Δ is the amplitude of the sinusoidal asperity, and λ is the wavelength. The contour plot of the sinusoidal surface is shown in Fig. 2.3.

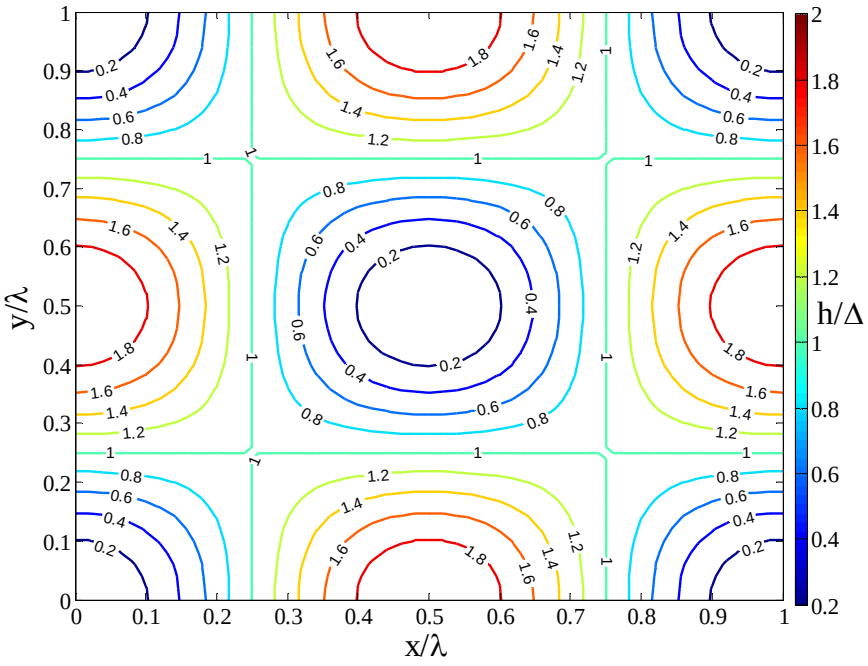

Fig. 2.3 Contour plot of the sinusoidal asperity.

JGH [54] presented two asymptotic solutions analytically for the early and near complete contact of sinusoidal asperities. Complete contact between contacting sinusoidal asperities happens when the two asperities are completely flattened out and there is no spacing between them. Jackson and Streator [52] presented an empirical equation for the

contact area connecting the two asymptotic solutions based on the numerical data provided by JGH [1]. JGH solutions for contact area only consider elastic deformation during contact of three-dimensional sinusoidal shaped surfaces. In their work, $\bar{p}$ is defined as the average pressure (considering both contacting and non-contacting regions) acting on the surfaces, and p^* is defined as the average pressure that when applied to the asperity causes complete contact. p^* is given as

$$p^* = \sqrt{2}\pi E^* \Delta f \tag{2.8}$$

where Δ is the amplitude of the sinusoidal asperity, f is the spatial frequency or reciprocal of the wavelength, λ $\left(f = 1/\lambda\right)$, and E^* is the equivalent elastic modulus which is given by

$$\frac{1}{E^*} = \frac{1-\nu_1^2}{E_1} + \frac{1-\nu_2^2}{E_2} \tag{2.9}$$

E_1, ν_1 and E_2, ν_2 are the elastic moduli and Poisson's ratios of the contacting surfaces. The contacting flat surface is rigid, so, Eq. (2.9) reduces to

$$E^* = \frac{E_1}{1-\nu^2} \tag{2.10}$$

The JGH solutions are applicable when $\bar{p} << p*$ i.e. at the early stages of contact, and when $\bar{p}$ approaches p^* ($\bar{p} \to p*$) i.e. near the complete contact. The equations are given as shown

$$\bar{p} << p*: \quad (A_{JGH})_1 = \frac{\pi}{f^2}\left[\frac{3}{8\pi}\frac{\bar{p}}{p^*}\right]^{2/3} \tag{2.11}$$

$$\bar{p} \to p^* \ : (A_{JGH})_2 = \frac{1}{f^2}\left(1 - \frac{3}{2\pi}\left[1 - \frac{\bar{p}}{p^*}\right]\right) \tag{2.12}$$

Empirical equations developed by Jackson and Streator [21] based on data provided by JGH, linking Eqs. (2.11) and (2.12) are given by

$$\text{for } \frac{\bar{p}}{p^*} < 0.8 \ : \ A = (A_{JGH})_1\left(1 - \left[\frac{\bar{p}}{p^*}\right]^{1.51}\right) + (A_{JGH})_2\left(\frac{\bar{p}}{p^*}\right)^{1.04} \tag{2.13}$$

$$\text{for } \frac{\bar{p}}{p^*} \geq 0.8 \ : \ A = (A_{JGH})_2 \tag{2.14}$$

Also, the asymptotic solutions for the surface separation, $\bar{g}$, for the early and near complete contact conditions of sinusoidal asperities developed by JGH are presented as

$$\text{for } \frac{\bar{p}}{p^*} << 1: \ \left(\frac{\bar{g}}{\Delta}\right)_1 = 1 - \frac{1}{2}\left(3\pi^2 \frac{\bar{p}}{p^*}\right)^{2/3} + 4\ln\left(\sqrt{2}+1\right)\left(\frac{\bar{p}}{p^*}\right) \tag{2.15}$$

$$\text{for } \frac{\bar{p}}{p^*} \to 1: \ \left(\frac{\bar{g}}{\Delta}\right)_2 = \frac{16}{15\pi^2}\left(\frac{3}{2}\right)^{3/2}\left[1 - \frac{\bar{p}}{p^*}\right]^{5/2} \tag{2.16}$$

Rostami and Jackson [55] developed an empirical equation for the average surface separation between sinusoidal asperities for the whole range of elastic contact connecting Eqs. (2.15) and (2.16) which is given by

$$\frac{\bar{g}}{\Delta} = \left(1 - \left(\frac{\bar{p}}{p^*}\right)^{1/2}\right)^{5/2} \tag{2.17}$$

A two-dimensional schematic representation of the surface separation in sinusoidal asperity contacts before and during contact stages is shown in Fig 2.4. The average surface separation, $\bar{g}$, is equal to the amplitude of the sinusoidal asperity, Δ, when the two surfaces touch each other, while during the contact, the average surface separation,

$\bar{g}$, is smaller than the amplitude of the sinusoidal asperity, Δ. In other words, when the average pressure between the two surfaces, $\bar{p}$, is equal to the complete contact pressure, p^*, the sinusoidal surface is completely flattened out and there is no gap between the surfaces, whereby $\bar{g} = 0$.

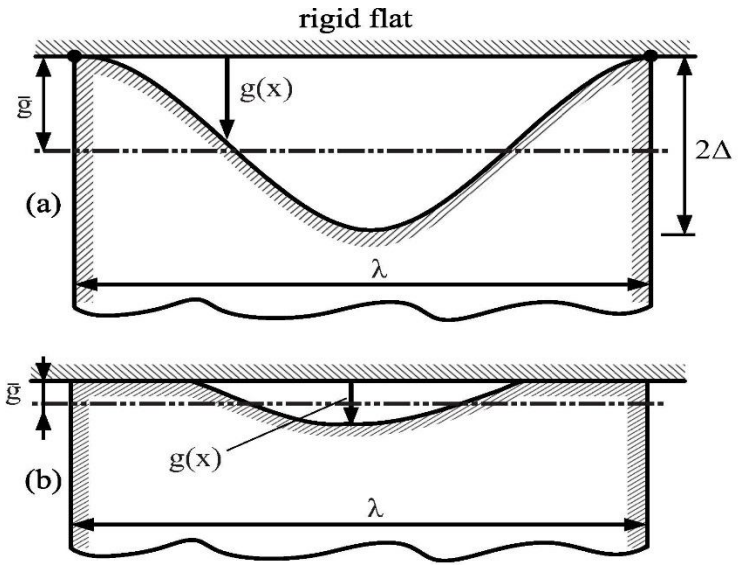

Fig. 2.4 A 2D representation of contact between a sinusoidal asperity and a rigid flat (a) before, and (b) during contact.

Eqs. (2.13), (2.14), and (2.17) are embedded in the JS multi-scale contact model to solve the solid-solid contact of rough surfaces in the current work.

2.1.2.2 Multi-scale contact model

JS multi-scale model for the contact between rough surfaces is briefly summarized here. The model is based on the following assumptions [52]:

1. Asperities of smaller cross-sectional surface area are located on top of larger asperities.

2. Each scale or level of frequency carries the same total load.
3. At each frequency level, the load is shared equally among the contacting asperities.
4. At each frequency level, each asperity deforms according to a chosen asperity contact model (elastic sinusoidal asperity contact in the current work).
5. The asperities of a certain level of frequency cannot be deformed more than the amplitude or height of the asperities at that level.

The average pressure, $\overline{p}_k$, at frequency level, k, can be obtained based on the assumptions #2 and #3

$$\overline{p}_k = \frac{F}{A_{k-1}} \tag{2.18}$$

where F is the total force between the contacting rough surfaces, and A_{k-1} is the contact area at the frequency level $k-1$ which acts as the nominal contact area for the frequency level k. Using the single asperity relations, the contact area and average surface separation of a single sinusoidal asperity at frequency level k under the contact pressure $\overline{p}_k$ can be calculated from Eqs. (2.13), (2.14), and (2.17) i.e. $\overline{A}_k = f\left(\overline{p}_k\right)$ and $\overline{g}_k = f\left(\overline{p}_k\right)$. Then, the contact area at the frequency level k can be calculated

$$A_k = N_k \overline{A}_k \tag{2.19}$$

In Eq. (2.19), N_k is the number of asperities in contact at frequency level k, and can be calculated by

$$N_k = \eta_k A_{k-1} \tag{2.20}$$

where η_k is the number of asperities per unit area and is related to the k level frequency $f_k = 1/\lambda_k$ by

$$\eta_k = 2 f_k^{\ 2} \tag{2.21}$$

The 3D rough surface considered in this work is comprised of oscillations both in x and y directions (Fig. 2.3). In JS multi-scale model, a single amplitude for each frequency scale is required based on a 1D discrete Fourier transform (DFT), of a 2D surface profile (i.e. $z(x)$), while for a 3D surface profile (i.e. $z(x,y)$) a matrix of coefficients is obtained by calculating the 2D DFT. Therefore, to apply the JS model to a 3D topography, an equivalent amplitude is calculated from the matrix of Fourier coefficients arising from the 2D DFT. Now, the 2D DFT can be expressed as

$$F(k_x,k_y) = \frac{1}{N_x N_y} \sum_{n_x=0}^{N_x-1} \sum_{n_y=0}^{N_y-1} z(n_x,n_y) e^{-i2\pi(k_x n_x/L_x + k_y n_y/L_y)} \tag{2.22}$$

where k_x and k_y correspond to the spatial frequencies in x and y directions, while n_x and n_y correspond to the spatial coordinates in x and y directions. The output is a $N_x \times N_y$ matrix comprising of complex elements. As the current model requires a single amplitude for each frequency scale, an equivalent 1D Fourier coefficient is calculated based on [56]

$$\beta_k = \frac{1}{2}\left[\sqrt{\sum_{k_y=0}^{N_y-1} \left|F\left(k,k_y\right)\right|^2} + \sqrt{\sum_{k_x=0}^{N_x-1} \left|F\left(k_x,k\right)\right|^2} \right] \tag{2.23}$$

The above equation is based on calculating the r.m.s. values of 1D Fourier coefficients in x and y directions and then averaging the two values. It can be shown that Δ_k is related

to the equivalent 1D amplitude coefficient, β_k, via the simple relation, $\Delta_k = 2\beta_k$, except at $k = N/2$, where $\Delta_{N/2} = \beta_{N/2}$.

2.1.3 Interaction between tensile and compressive stresses

In order to consider the effect of liquid film in contact between rough surfaces, the average gap between two surfaces and also the area over which the liquid film acts are needed to be determined. A volume-loss approach, which is based on the calculation of surface deformation due to both compressive and tensile stresses, is implemented. This approach is based on calculating the reduction in the average gap between the two surfaces in the wetted region based on the compressive and tensile volume losses, as detailed below.

2.1.3.1 Volume loss due to compressive stresses

The deformation volume or the loss in available volume due to compressive stresses can be calculated by summing up the volume losses at different frequency scales based on the JS multi-scale model. Each frequency scale experiences a separate volume loss. In order to calculate the volume loss in each frequency scale, the reduction in the average gap in each frequency scale is calculated. The initial average gap at each frequency scale is equal to the amplitude at that frequency scale when there is no force acting on the contacting surfaces. In the presence of force the average gap reduction at frequency scale k can be calculated as

$$\left(\Delta\bar{g}_k\right)_c = \Delta_k - \bar{g}_k = \Delta_k\left(1-\left(1-\left(\frac{\bar{p}_k}{p_k^*}\right)^{1/2}\right)^{5/2}\right) \tag{2.24}$$

where $\left(\Delta\bar{g}_k\right)_c$ is the reduction in average gap at frequency scale k due to compressive stresses. This reduction multiplied by the contact area at frequency level $k-1$ (which acts as a nominal contact area for frequency scale k) gives the volume loss associated with the frequency scale k. Therefore, the total volume loss due to compressive stresses, ΔV_c, can be calculated by

$$\Delta V_c = \sum_{k=1}^{k_{\max}} \left(\Delta\bar{g}_k\right)_{comp} A_{k-1} \tag{2.25}$$

2.1.3.2 Volume loss due to tensile stresses

The liquid film also tends to cause surface deformation by inducing tensile stresses between surfaces due to capillary pressure. In the presence of a liquid film, the solutions for the solid-solid contact are not strictly valid anymore. However, the solutions are still used in the current work to calculate contributions of the compressive stresses in the contact between surfaces. In calculation of the volume loss due to tensile stresses, it is assumed that the real contact area is a small fraction of the nominal contact area (an assumption that is to be validated later). Thus, ignoring the regions of solid-solid contact, it follows that the tension throughout the wetted region is uniform and equal in magnitude to the Laplace-Young pressure. This assumption of pressure uniformity is invalid after the point of surface collapse because then the ratio of real contact area to nominal contact area is no longer expected to be small. Therefore, the methods used here to solve the contact problem are valid up to the point where instability occurs (i.e., to the point of surface collapse). For a uniform pressure, Δp, acting on a circular wetted area with radius, r_w, the deformation in the wetted region can be obtained by [57]

$$u_t(r) = \frac{4}{\pi E'} \Delta p r_w E(r / r_w) \qquad r \le r_w \tag{2.26}$$

where $u_t(r)$ denotes the elastic deformation at radial position r measured from the center of rectangular domain (Fig. 2.1), and $E(r / r_w)$ is the complete elliptic integral of the second kind. Integrating Eq. (2.26) over the wetted region, the volume loss due to tensile stresses, ΔV_t, can be calculated by

$$\Delta V_t = \int_0^{r_w} u_t(r)(2\pi r dr) \tag{2.27}$$

Substituting and rearranging Eq. (2.26) in Eq. (2.27), the following relation can be obtained

$$\Delta V_t = \frac{8 \Delta p r_w}{E'} \int_0^{r_w} r E(r / r_w) dr \tag{2.28}$$

Integrating Eq. (2.28), the following relation for volume loss due to tensile stresses can be obtained

$$\Delta V_t = \frac{16}{3} \frac{\Delta p}{E'} r_w^3 \tag{2.29}$$

Substituting for the pressure drop from Eq. (2.6) in Eq. (2.29), the following relation for the volume loss due to tensile stresses can be obtained

$$\Delta V_t = \frac{16}{3} \frac{\gamma(\cos\theta_A + \cos\theta_B)}{\bar{h} E'} r_w^3 \tag{2.30}$$

where the volume loss due to tensile stresses for a certain liquid is only a function of average gap, $\bar{h}$, and the wetted radius, r_w. Also, the tensile force, F_t, can be related to the Laplace-Young pressure according to the following relation

$$F_t = \pi r_w^2 \Delta p \tag{2.31}$$

where F_t is the tensile force between the rough surfaces. Substituting for the Laplace-Young pressure from Eq. (2.6), the relation below can be obtained

$$F_t = \frac{\pi \gamma r_w^2}{\bar{h}}\left(\cos\theta_A + \cos\theta_B\right) \tag{2.32}$$

The total volume loss in the wetted region, ΔV_{tot}, is calculated by summing the volume loss due to compressive stresses in the wetted region, and the volume loss due to tensile stresses, ΔV_t.

$$\Delta V_{tot} = \left(\frac{\pi r_w^2}{A_n}\right)\Delta V_c + \Delta V_t \tag{2.33}$$

The coefficient multiplying ΔV_c (which is the compressive volume loss over the entire nominal contact region) is needed to account for the fact that we are interested in the total volume loss within the wetted region.

When the two surfaces come into contact at zero load, the gap between the two surfaces is the maximum height of the rough surface, $z_{\max}$. During loading, the deformation due to both compressive and tensile stresses causes a change in the average gap between the surfaces. The new average gap within the wetted region can be obtained using the total volume loss

$$\bar{h} = z_{\max} - \frac{\Delta V_{tot}}{\pi r_w^2} = z_{\max} - \frac{\Delta V_c}{A_n} - \frac{\Delta V_t}{\pi r_w^2} \tag{2.34}$$

Enforcing the volume conservation of the liquid film, the following relation between the average gap and the radius of the wetted region can be obtained

$$V_0 = \pi r_w^2 \bar{h} \tag{2.35}$$

This relationship can be written alternatively by

$$r_w = \left(V_0 / \pi \bar{h}\right)^{1/2} \tag{2.36}$$

Substituting for the average gap between the surfaces from Eq. (2.34)

$$r_w = \left(\frac{V_0}{\pi \left(z_{\max} - \frac{\Delta V_c}{A_n} - \frac{\Delta V_t}{\pi r_w^2} \right)} \right)^{1/2} \tag{2.37}$$

Due to the nonlinear dependency of the both compressive and tensile stresses on the radius of the wetted region, Eq. (2.37) must be solved iteratively. It should be noted that the compressive volume loss depends on the total force between the two surfaces, which is the sum of the external load, P, and the tensile force, F_t. The compressive force, F_c, is given by

$$F_c = P + F_t \tag{2.38}$$

where F_t can be calculated from Eq. (2.32).

2.1.4 Numerical Algorithm

The numerical algorithm used to solve the liquid-mediated adhesion in contact between rough surfaces is shown in Fig 2.5. The material and geometrical properties of the contacting rough surfaces and the liquid are needed in the numerical algorithm. When the two surfaces touch each other, the initial average gap is equal to the maximum height of the rough surface. As the surfaces come into contact, the average gap will change, and the new average gap and radius of wetted region are obtained using Eqs. (2.34) and (2.37). The iteration process will continue until convergence is acquired.

Convergence or divergence of the iteration process is determined based on the relative error of the tensile force in two successive iterations ($\left|F_{t-new} - F_{t-old}\right| / F_{t-old}$. Convergence is accomplished when the relative error is less than 10^{-5} .

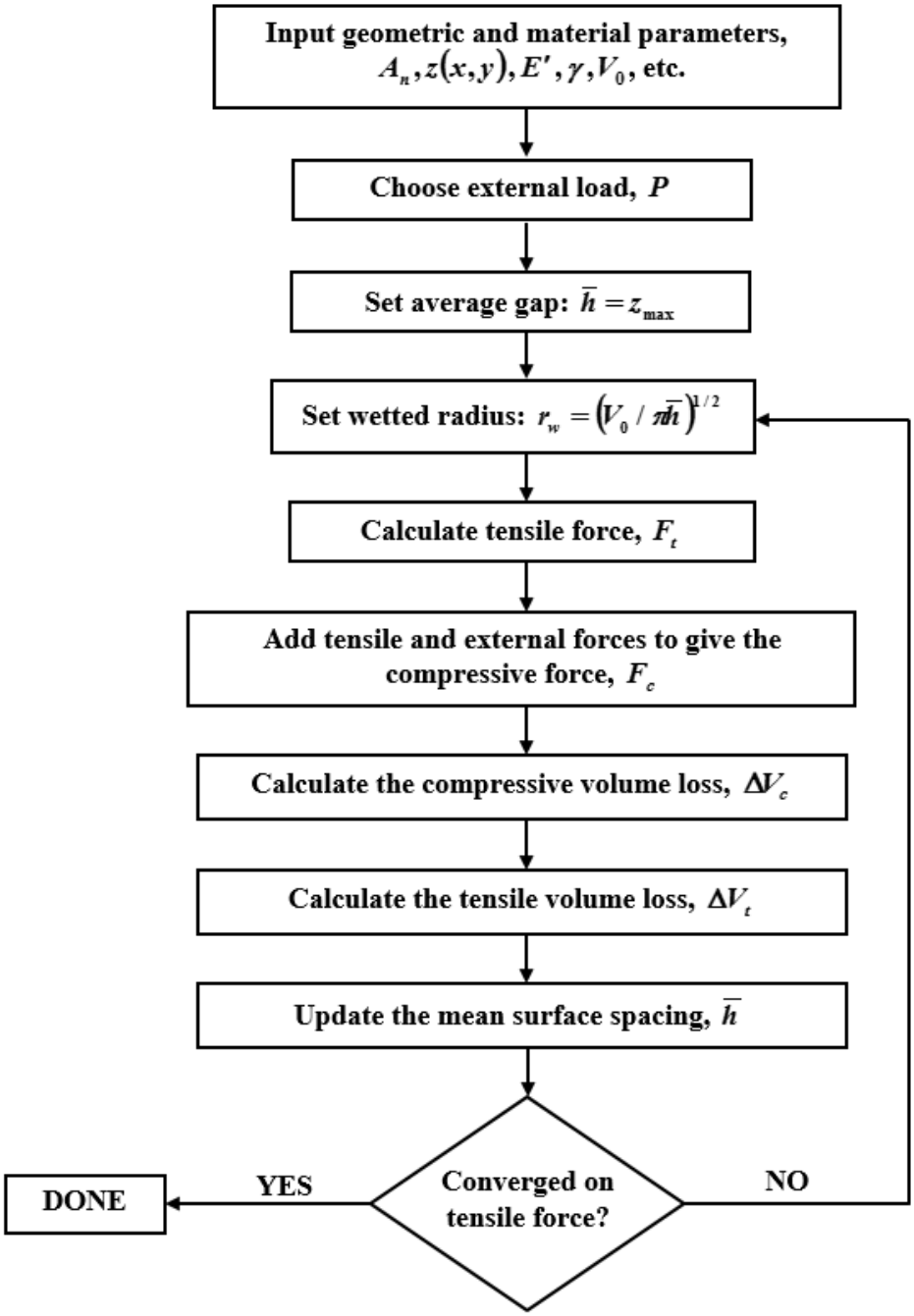

Fig. 2.5 Flowchart of the numerical algorithm.

2.1.5 Results

The results of the numerical model developed for the contact between rough surfaces in the presence of liquid film are presented in this section. The input parameters such as rough surface nominal contact area, A_n, surface topography, $z(x,y)$, effective elastic modulus, E', liquid volume, V_0, liquid surface tension, γ, and contact angles, $\theta_{A,B}$, are needed to obtain a set of results. For convenience, a zero value is selected for contact angles of the liquid film with upper and lower surfaces, $\theta_{A,B} = 0$. Three-dimensional Gaussian isotropic surfaces generated by computer are used for the simulations. It was shown [58] that the statistical features of many random profiles such as distribution of heights, curvatures, slopes, and peak density could be expressed in terms of two parameters, namely the r.m.s. roughness, σ, and the correlation length, l_c. In this work, a surface generation method outlined by Garcia and Stoll [59] is implemented, where an uncorrelated distribution of surface points using a random number generator is convolved with a Gaussian filter to achieve a random Gaussian rough surface with a prescribed standard deviation and having an exponential autocorrelation function with a prescribed correlation length.

The numerical algorithm shown in Fig. 2.5 is used to obtain the equilibrium configuration for a given surface topography with the reference material and geometrical properties given in Table 2.1. The simulated rough surface has a Gaussian isotropic distribution with correlation length to side length ratio of $l_c / L = 1/200$. The results for the tensile force, F_t, average gap, $\bar{h}$, wetted radius, r_w, and real contact area, A_r, versus the

flexibility of the rough surface, $1/E'$, in the absence of external load, $P=0$, are shown in Fig. 2.6.

Table 2.1 Reference properties

$V_0 = 0.1\ \text{mm}^3$	$\sigma = 0.4\ \mu\text{m}$
$\gamma = 72.7\ \text{mN/m},$	$A_n = 4\ \text{cm}^2$

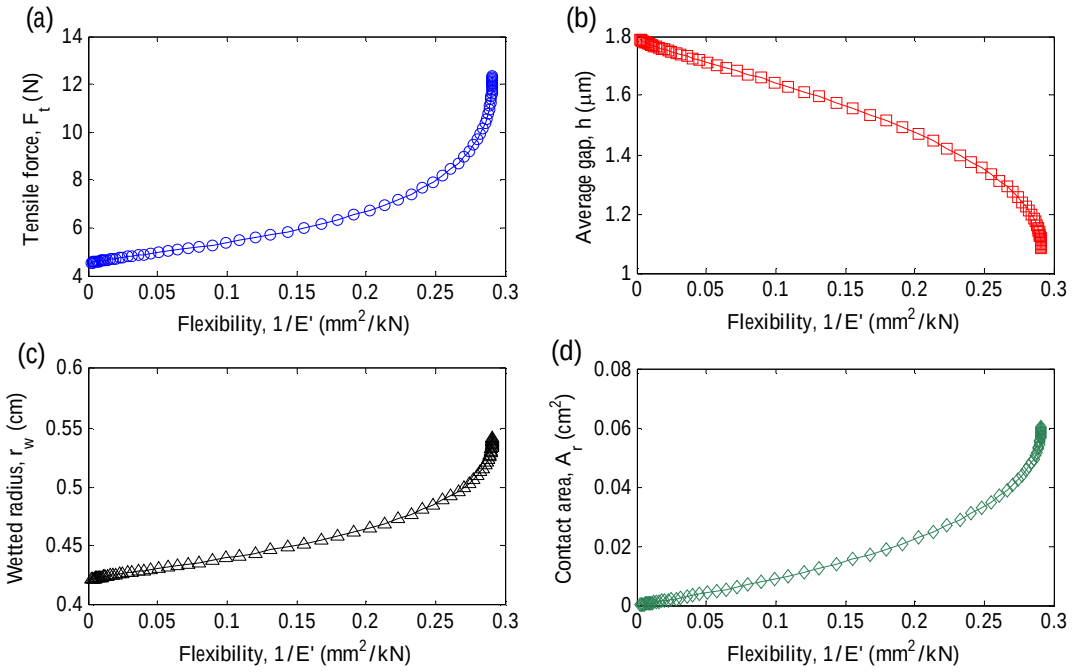

Fig. 2.6 The results for (a) tensile force, (b) average gap, (c) wetted radius, and (d) contact area versus the flexibility of the rough surface.

In Fig. 2.5, tensile force, F_t, contact area, A_r, and the radius of wetted region, r_w, increase, while the average gap decreases with the flexibility of the rough surface until the slope of the curve becomes vertical. The last data point on the curve (to a resolution of $10^{-9}\ mm^2/kN$ in the value of flexibility) is taken as the point of instability, and it means that no equilibrium configuration could be obtained for the contact problem for

higher values of flexibility. For higher flexibilities, then, the tensile force overwhelms the compressive force and the two surfaces are predicted to experience near-complete or complete contact (i.e. surface collapse).

The results for the tensile force, average gap, wetted radius, and contact area versus the external load applied between the contacting rough surfaces for the material and geometrical properties given in Table 2.1 are shown in Fig. 2.7. It should be noted the results in Fig. 2.7 are obtained based on the flexibility value of $1/E' = 0.02\ \ mm^2/kN$.

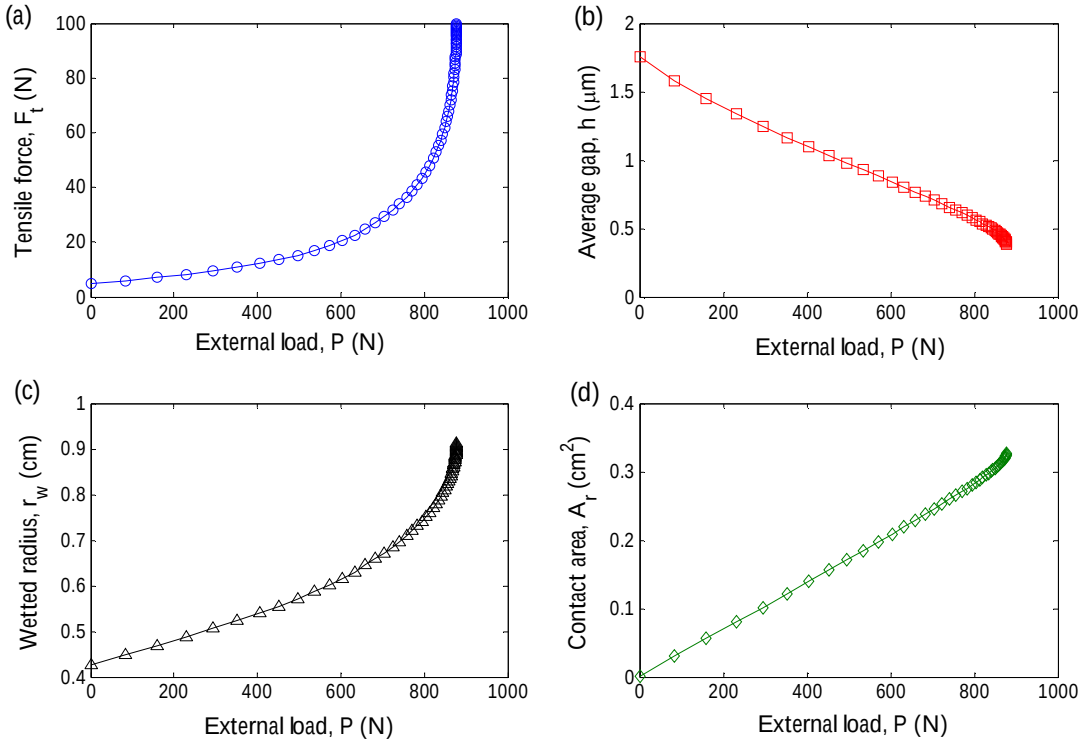

Fig. 2.7 The results for (a) tensile force, (b) average gap, (c) wetted radius, and (d) contact area versus the external load between contacting surfaces.

As it can be seen in Fig. 2.7, the tensile force, wetted radius, and contact area increase while the average gap decreases with the external load. As external load, P, increases, it causes more interaction between the contacting surfaces, which causes a reduction in average gap, $\bar{h}$, between the surfaces and also an increase in the contact area, A_r, between the surfaces. As the gap between the surfaces decreases, the liquid volume between the surfaces spreads over a wider area, which means that the radius of wetted region, r_w, increases. The reduction in average gap and the increase in the wetted area causes the tensile force, F_t, to increase.

2.1.5.1 Non-dimensionalization

In this section, we seek normalization to present the results in the most general way. By substituting for the radius of wetted region, r_w, from Eq. (2.36) in Eq. (2.32), we have

$$F_t = \frac{\gamma V_0}{\bar{h}^2}\left(\cos\theta_A + \cos\theta_B\right) \tag{2.39}$$

Considering the case with no external load, $P = 0$, the compressive force on a given surface balances the tensile force ($F_c = F_t$). Also, ignoring the effect of tensile stresses on the average gap in initial contact, the average gap for the first frequency scale $(k = 1)$ can be related to the load by Eq. (2.17)

$$\frac{g_1}{\Delta_1} = \left(1 - \left(\frac{F_t}{A_n p_1^*}\right)^{1/2}\right)^{5/2} \tag{2.40}$$

where the average pressure in the first frequency, $\bar{p}_1$, is calculated by dividing the tensile force, F_t, by the nominal contact area at the first frequency level, A_n. The complete contact pressure at the first frequency can be calculated using Eq. (2.8) with Eq. (2.40)

$$\frac{g_1}{\Delta_1} = \left(1 - \left(\frac{F_t}{\sqrt{2}\pi E' A_n^{1/2} \Delta_1}\right)^{1/2}\right)^{5/2} \tag{2.41}$$

Now substituting Eq. (2.39) in (2.41)

$$g_1 = \Delta_1 \left(1 - \left(\frac{\gamma V_0 \left(\cos\theta_A + \cos\theta_B\right)}{\sqrt{2}\pi A_n^{1/2} E' \Delta_1 \bar{h}^2}\right)^{1/2}\right)^{5/2} \tag{2.42}$$

Supposing that the average gap at frequency level 1, $\bar{g}_1$, is related to the overall gap, $\bar{h}$, by some factor X such that $\bar{g}_1 = X\bar{h}$. Then we can conclude

$$\frac{\bar{h}}{\sigma} = \frac{1}{X}\frac{\Delta_1}{\sigma}\left(1 - \left(\frac{\gamma V_0 \left(\cos\theta_A + \cos\theta_B\right)}{\sqrt{2}\pi A_n^{1/2} E' \sigma^3 \left(\Delta_1/\sigma\right)\left(\bar{h}/\sigma\right)^2}\right)^{1/2}\right)^{5/2} \tag{2.43}$$

where the r.m.s. roughness, σ, is used as a scaling factor. It can be deduced from Eq. (2.43)

$$\frac{\bar{h}}{\sigma} = \tilde{f}\left(\frac{\gamma V_0 \left(\cos\theta_A + \cos\theta_B\right)}{\sqrt{2}\pi A_n^{1/2} E' \sigma^3}, \frac{\Delta_1}{\sigma}, X\right) \tag{2.44}$$

where $\tilde{f}$ is an unknown function, Δ_1 and σ are specified by the undeformed surface profile, so, Δ_1/σ is a geometric parameter. In contrast, X relates the parameters that result from deformation, i.e. $\bar{g}_1$ and $\bar{h}$. However, it can be shown that, for a given σ, X depends only on the details of the surface profile (i.e. the set of amplitude

coefficients). Therefore, Eq. (2.43) implies that the equilibrium gap for a given surface profile depends only on the dimensionless parameter $\gamma V_0\left(\cos\theta_A+\cos\theta_B\right)/\sqrt{2}\pi A_n^{1/2}E'\sigma^3$. Therefore, an adhesion parameter is defined as

$$\Gamma=\frac{\gamma V_0\left(\cos\theta_A+\cos\theta_B\right)}{\sqrt{2}\pi A_n^{1/2}E'\sigma^3} \tag{2.45}$$

Considering the external load introduces another parameter into the dependence of $\bar{h}/\sigma$ on the input parameters. Also, consideration of the direct effect of tensile stresses introduces the additional dimensionless ratio $V_0/A_n\sigma$ which we label as V_0^* and refer to as the dimensionless volume. The dimensionless tensile force, F_t^*,and external force, P^*, can be expressed as

$$F_t^*=\frac{F_t}{\gamma V_0\left(\cos\theta_A+\cos\theta_B\right)/\sigma^2}=\left(\frac{\sigma}{\bar{h}}\right)^2 \tag{2.46}$$

$$P^*=\frac{P}{\gamma V_0\left(\cos\theta_A+\cos\theta_B\right)/\sigma^2} \tag{2.47}$$

In general, for a given rough surface profile, we can write

$$\frac{\bar{h}}{\sigma}=\tilde{f}'\left(\Gamma,P^*,V_0^*\right) \tag{2.48}$$

where $\tilde{f}'$ is an unknown function. Alternatively, using Eq. (2.46), we obtain

$$F_t^*=\tilde{f}''\left(\Gamma,P^*,V_0^*\right) \tag{2.49}$$

where $\tilde{f}''$ denotes another unknown function. For a given surface topography, Eqs. (2.48) and (2.49) are the most general expressions for the equilibrium average gap and tensile force, respectively.

2.1.5.2 Equilibrium curves

In this section, the results for non-dimensional tensile force, F_t^*, versus the non-dimensional adhesion parameter, Γ, for different material and geometrical parameters are presented. A convergence test is performed to obtain the number of numerical nodes needed along both x and y axes to get accurate results for a 3D Gaussian isotropic surface. As shown in Fig. 2.8, for each case the tensile force increases with increasing adhesion parameter until the curve becomes vertical. It can be seen that convergence is acquired for node numbers higher than 2000 along coordinate axis for a Gaussian isotropic surface with $l_c / L = 1/200$. Performing an extensive number of simulations for different Gaussian isotropic surfaces varying correlation length, l_c, and side length, L, it is shown that the convergence is guaranteed for simulated surfaces with at least 10 nodal points per correlation length. In the current work, the numerical results are obtained for the nominal contact area with $L = 2$ cm.

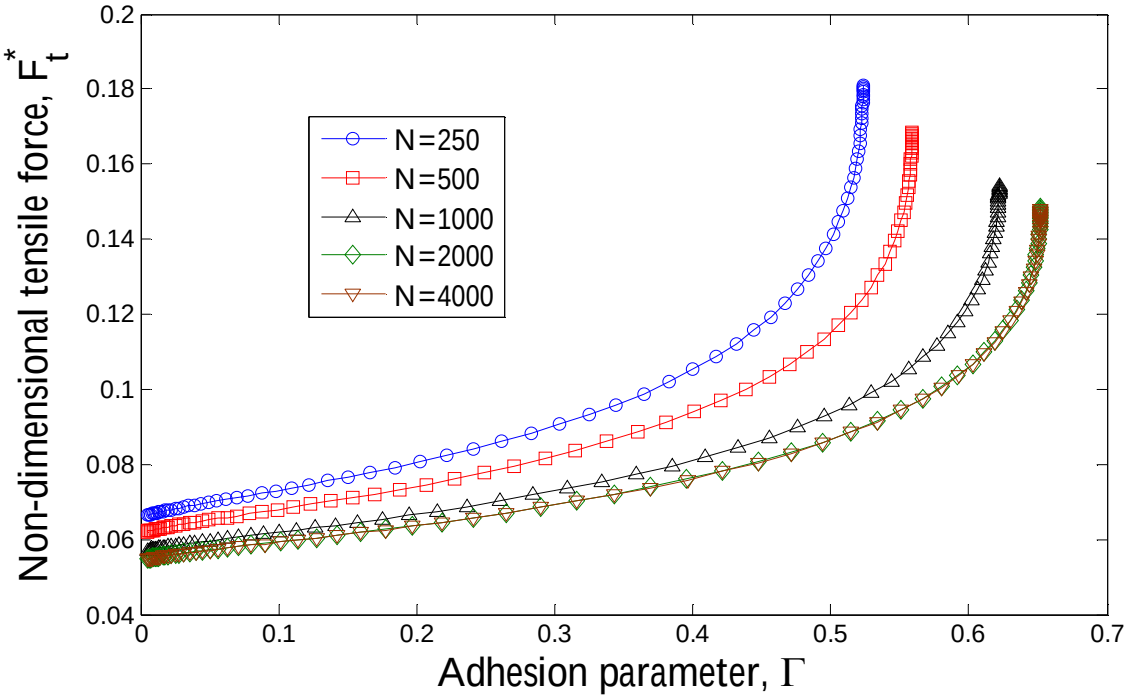

Fig. 2.8 Non-dimensional tensile force results versus adhesion parameter for different number of nodes, N, along each coordinate axis.

As mentioned previously, the non-dimensional tensile force, F_t^*, is a function of adhesion parameter, Γ, non-dimensional external load, P^*, and non-dimensional liquid volume, V_0^*. The results for the dimensionless tensile force, F_t^*, versus the adhesion parameter, Γ, for different values of dimensionless volume, V_0^*, in the absence of external load ($P^* = 0$) are shown in Fig 2.9. As expected, the normalized adhesion force increases with adhesion parameter for different values of the dimensionless volume until it reaches a vertical slope, suggestive of surface collapse. As the non-dimensional liquid volume increases, the instability occurs at higher values of the adhesion parameter; however, the non-dimensional tensile force at the point of instability is nearly the same at each of the non-dimensional liquid volumes.

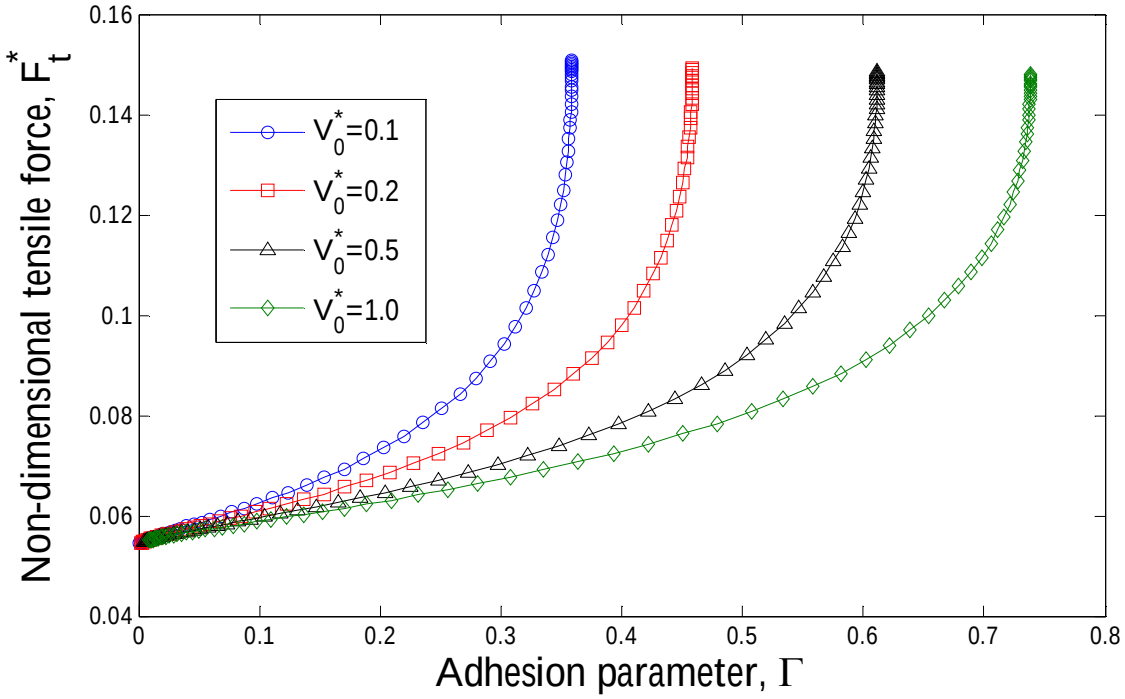

Fig. 2.9 Non-dimensional tensile force versus adhesion parameter for different values of non-dimensional liquid volumes.

Fig. 2.10 shows the results for non-dimensional tensile force, F_t^*, versus the adhesion parameter, Γ, for different values of dimensionless external load, P^*. A constant value is selected for the non-dimensional liquid volume for all the cases in Fig. 2.10 ($V_0^* = 0.5$). It can be seen in Fig. 2.10, as the external load, P^*, increases, the instability occurs at lower values of the adhesion parameter, Γ. Also, the non-dimensional tensile force, F_t^*, at the point of instability increases as the non-dimensional external load, P^*, increases.

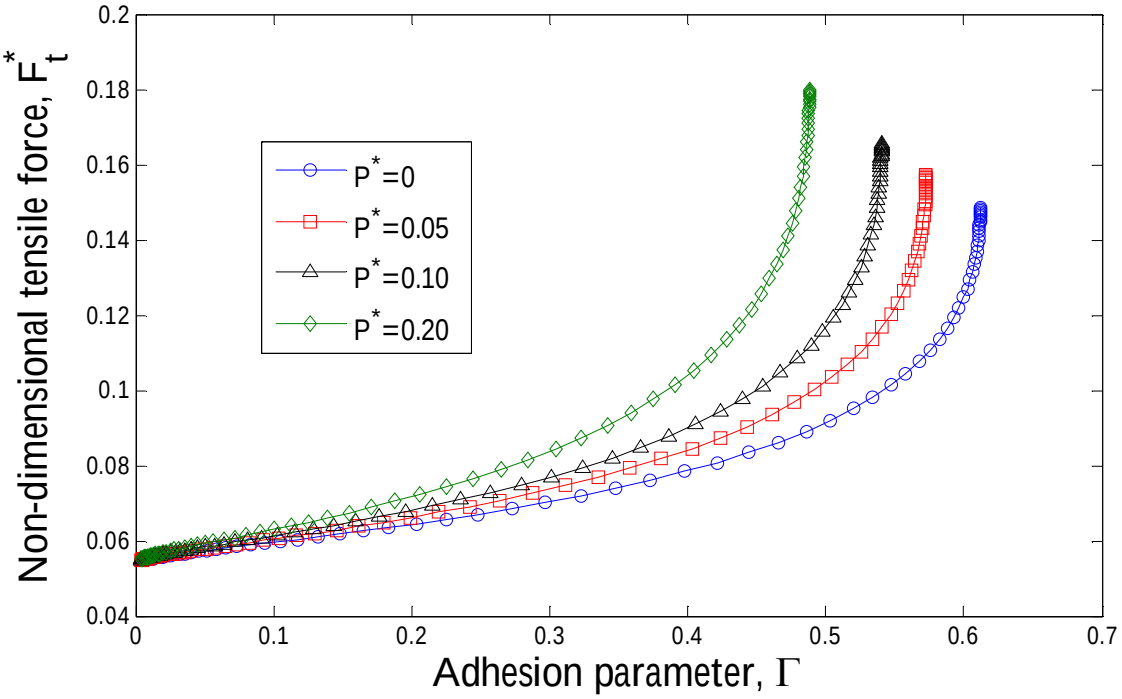

Fig. 2.10 Non-dimensional tensile force versus adhesion parameter for different values of non-dimensional external load.

Results for the average gap normalized by the r.m.s. surface roughness, $h^* = \bar{h}/\sigma$, versus the adhesion parameter, Γ, are shown in Fig. 2.10 for different non-dimensional liquid volumes, V_0^*, where $P^* = 0$, and shown in Fig. 2.11 for non-dimensional external loads, P^*, where $V_0^* = 0.5$. As observed in Fig. 2.11, the non-dimensional average gap, h^*, decreases as the adhesion parameter, Γ, increases until the slope of the curve becomes vertical. Additionally, the instability occurs at higher values of adhesion parameter, Γ, as the non-dimensional liquid volume, V_0^*, increases. In Fig. 2.12, the instability happens at lower values of adhesion parameter, Γ, as the non-dimensional external load, P^*, increases. Also, Fig. 2.12 shows that as the non-dimensional external

load, P^*, increases, the non-dimensional average gap, h^*, at the point of instability decreases.

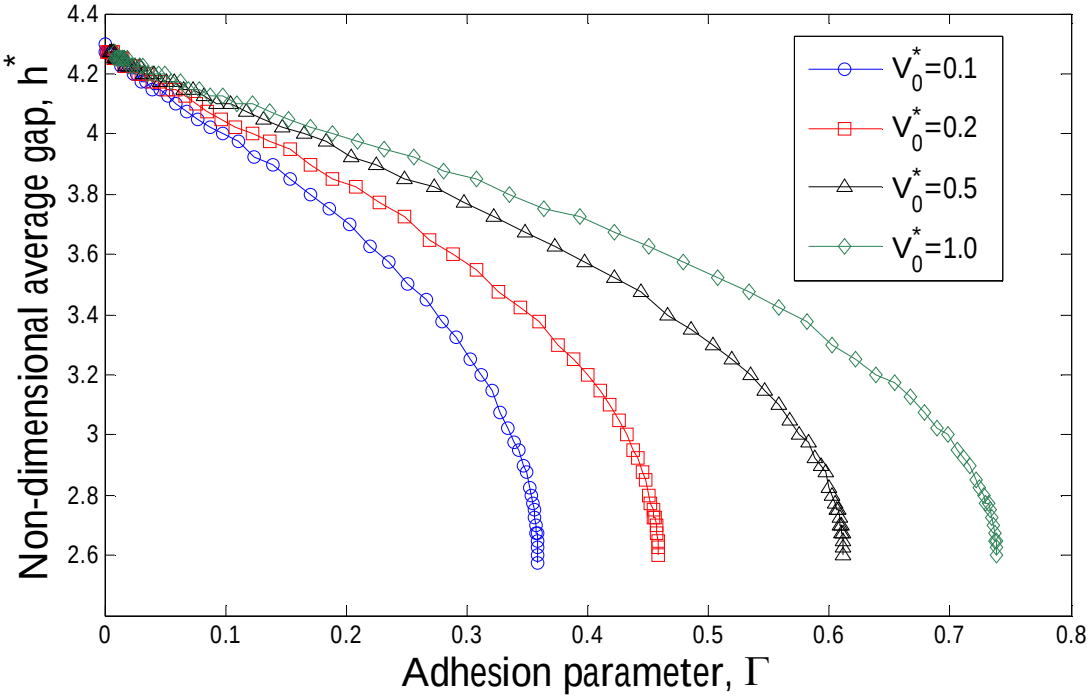

Fig. 2.11 Non-dimensional average gap versus adhesion parameter for different values of non-dimensional liquid volume.

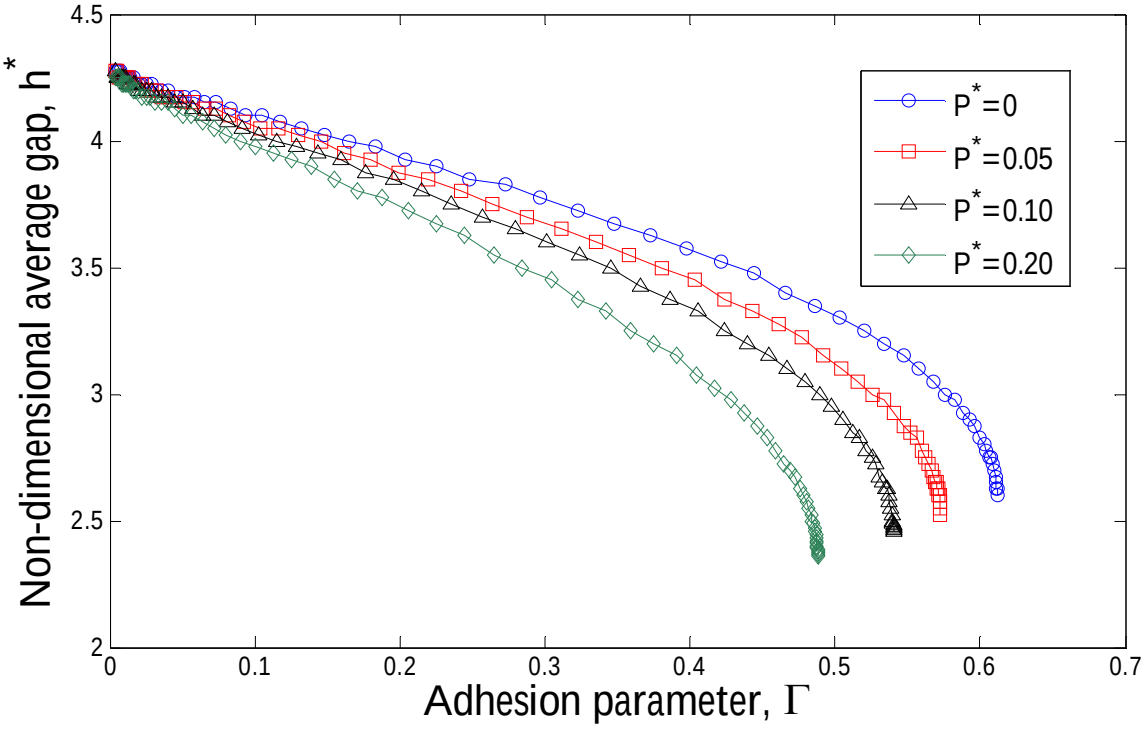

Fig. 2.12 Non-dimensional average gap versus adhesion parameter for different values of non-dimensional external load.

The results for non-dimensional contact area, $A_r^* = A_r / A_n$, versus the adhesion parameter, Γ, are shown in Fig. 2.13 for different non-dimensional liquid volumes, V_0^*, where $P^* = 0$, and in Fig. 2.14 for non-dimensional external loads, P^*, where $V_0^* = 0.5$. As the non-dimensional liquid volume, V_0^*, increases, the non-dimensional contact area, A_r^*, at the point of instability also increases (Fig. 2.13). Likewise, as the non-dimensional external load, P^*, increases, the non-dimensional contact area, A_r^*, at the point of instability increases (Fig. 2.14). As it can be seen from Figs. 2.13 and 2.14, the non-dimensional contact area, A_r^*, is less than 2% at the point of instability, which validates the model assumption that the real contact area is a small fraction of nominal contact area.

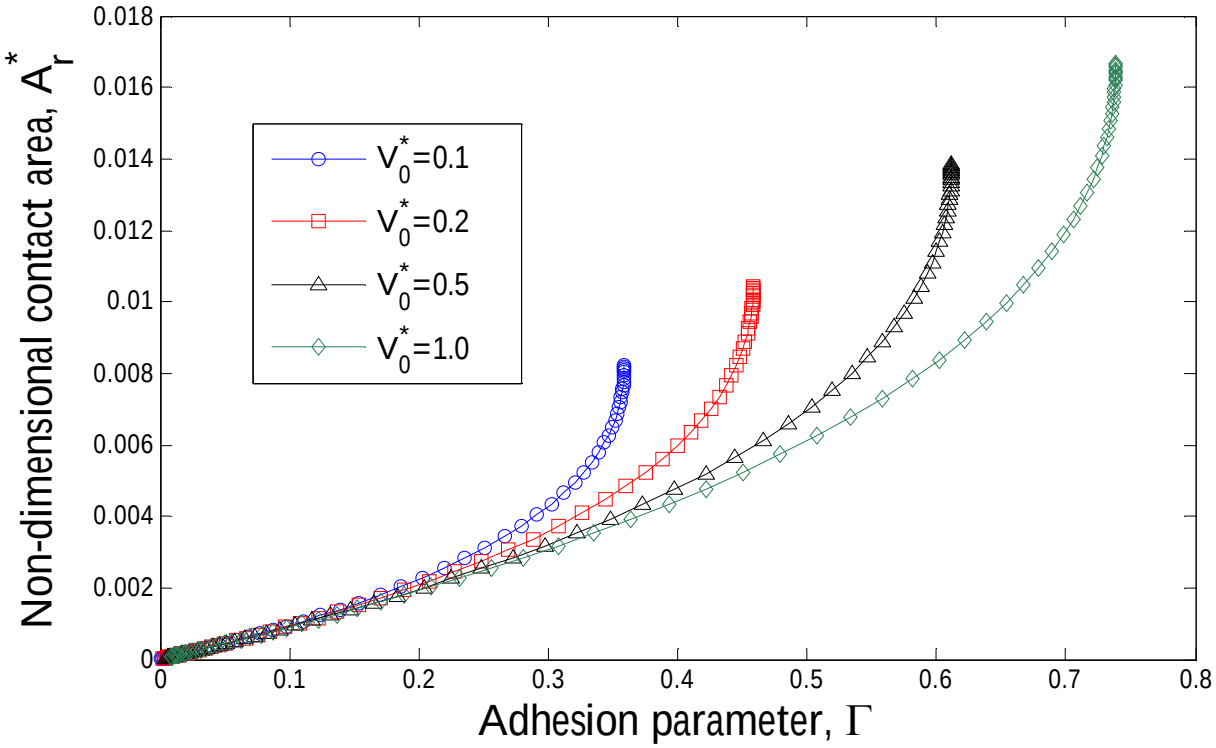

Fig. 2.13 Non-dimensional contact area versus adhesion parameter for different values of non-dimensional liquid volume.

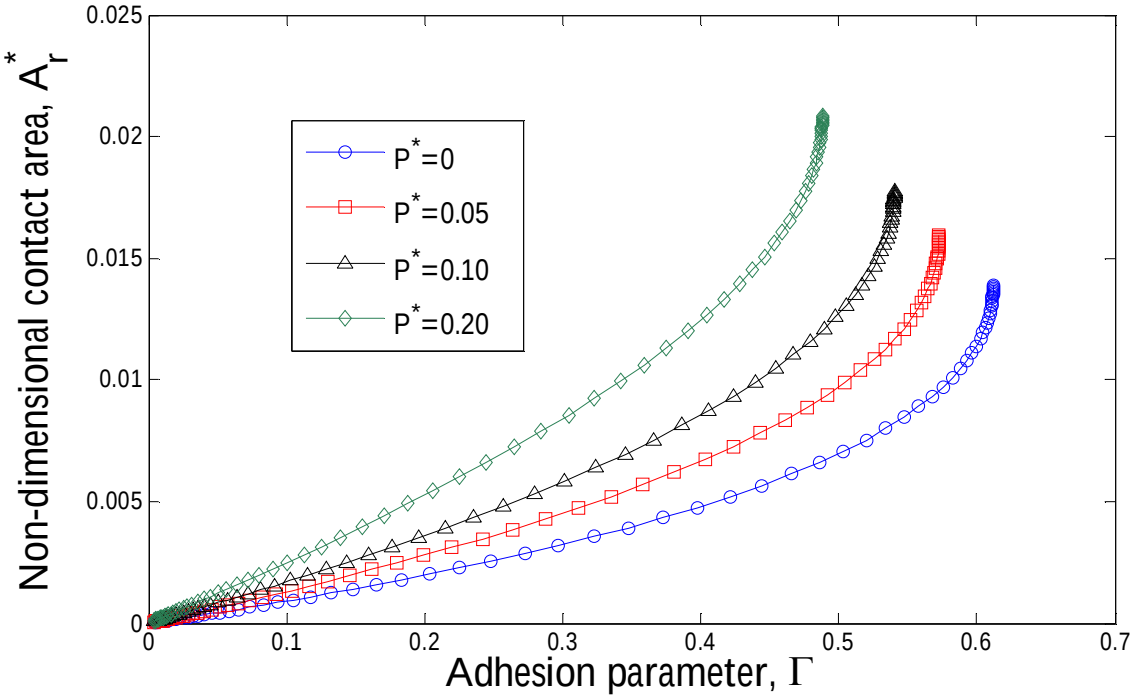

Fig. 2.14 Non-dimensional contact area versus adhesion parameter for different values of non-dimensional external load.

2.1.5.3 Critical adhesion parameter

It is of interest to predict the point of instability in liquid-mediated contact between solid surfaces, as beyond this point, the surfaces would experience strong adhesion or stiction. In this section, the goal is to obtain a relation for the point of instability based on material and geometrical properties of the rough surfaces and the liquid film. Presenting a general relation that is applicable to all rough surfaces including both Gaussian and non-Gaussian random rough surfaces is not feasible. However, restricting our attention to rough surfaces with an isotropic Gaussian distribution simplifies the task. It can be concluded from Figs. (2.9-2.14) that the critical adhesion parameter, Γ_{cr}, for a given rough surface is a function of non-dimensional liquid volume, V_0^*, and non-dimensional external load, P^*, i.e. $\Gamma_{cr} = f\left(V_0^*, P^*\right)$. The results in Figs. (2.9-2.14) were obtained for a given rough surface with r.m.s. roughness of $\sigma = 0.4\,\mu\text{m}$, and having an isotropic Gaussian distribution with correlation length to side ratio of $l_c / L = 1/200$. The dependency of the critical adhesion parameter, Γ_{cr}, on the correlation length, l_c, of a Gaussian isotropic rough surface with a given r.m.s. roughness, σ, is investigated in Fig. 2.15. The results in Fig. 2.15 are obtained for the critical adhesion parameter, Γ_{cr}, versus the non-dimensional maximum height, $z_{\max}^* = z_{\max} / \sigma$, of a Gaussian isotropic rough surface with r.m.s. roughness of $\sigma = 0.4$ μm. It can be seen that the critical adhesion parameter, Γ_{cr}, increases as the maximum height of the surface, $z_{\max}^*$, increases, and it is independent of correlation length, l_c.

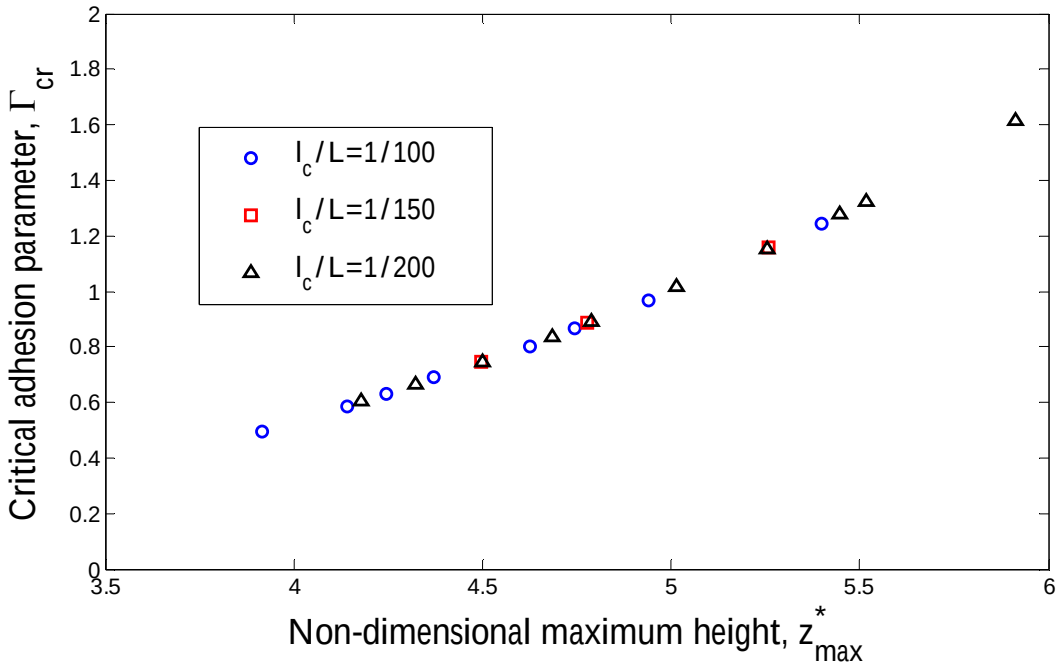

Fig. 2.15 Critical adhesion parameter versus the non-dimensional maximum height for different values of correlation length.

In Fig. 2.16, the results are obtained for the critical adhesion parameter, Γ_{cr}, versus the non-dimensional maximum height, z^*_{max}, for different values of r.m.s. roughness, σ, while the correlation length is constant and set to $l_c/L=1/200$. The results show that the critical adhesion parameter, Γ_{cr}, is also independent of r.m.s. roughness, which is a consequence of the normalization considered in this work. The results in Figs. 2.15 and 2.16 lead us to conclude that by considering the effect of maximum surface height, z^*_{max}, a general relation for critical adhesion parameter can be obtained, which is applicable to different Gaussian isotropic rough surfaces.

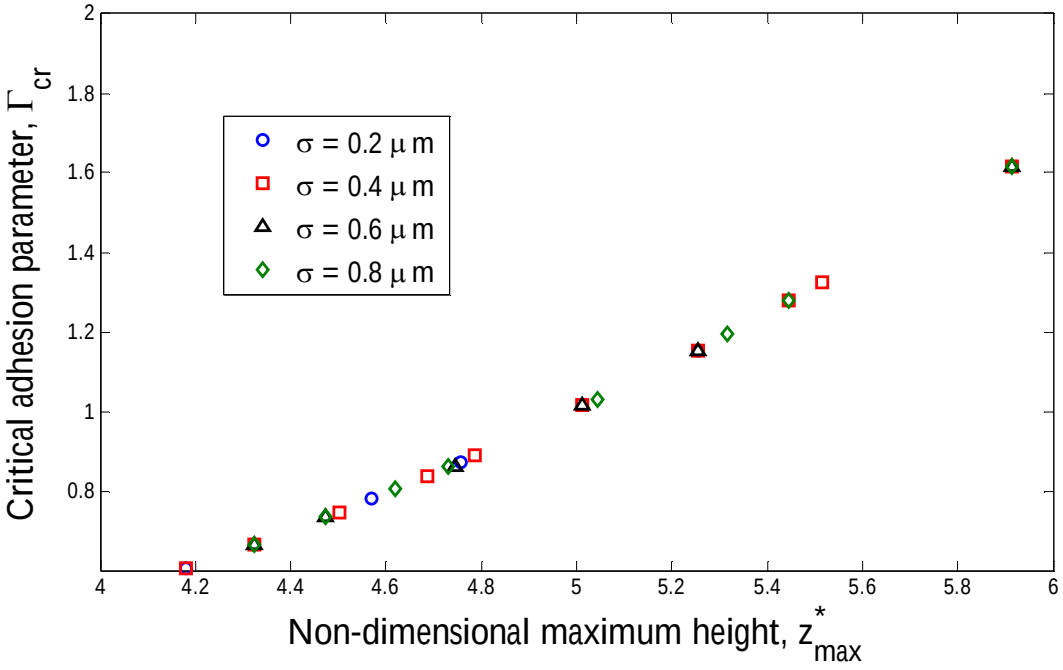

Fig. 2.16 Critical adhesion parameter versus the non-dimensional maximum height for different values of r.m.s. roughness.

Therefore, the critical adhesion parameter, Γ_{cr}, for different Gaussian isotropic rough surfaces is a function of three different parameters, non-dimensional liquid volume, V_0^*, non-dimensional external load, P^*, and non-dimensional maximum height, $z_{\max}^*$, i.e.

$$\Gamma_{cr} = f\left(V_0^*, P^*, z_{\max}^*\right) \tag{2.50}$$

In the absence of external load, $P^* = 0$, Γ_{cr} is dependent only on V_0^* and $z_{\max}^*$. An empirical relation is developed for Γ_{cr} based on the extensive results obtained for critical adhesion parameter for different combinations of $z_{\max}^*$ and V_0^* (Fig. 2.17). The relation is given by

$$\Gamma_{cr} = 0.011 {z_{\max}^*}^{2.87} {V_0^*}^{0.32} \tag{2.51}$$

The above relation is valid for the non-dimensional liquid volume range, $0.05 < V_0^* < 2$, and non-dimensional surface height range, $4.18 < z_{max}^* < 5.91$[1]. The average relative error between the empirical Eq. (2.50) and the numerical results in Fig. 2.17 is 2.9 %. For cases with $0 < \Gamma < \Gamma_{cr}$, the instability does not occur in the interface of contact; when $\Gamma = \Gamma_{cr}$, the interface is at the critical point, and when $\Gamma > \Gamma_{cr}$, the interface experiences instability, and no equilibrium configuration can be found.

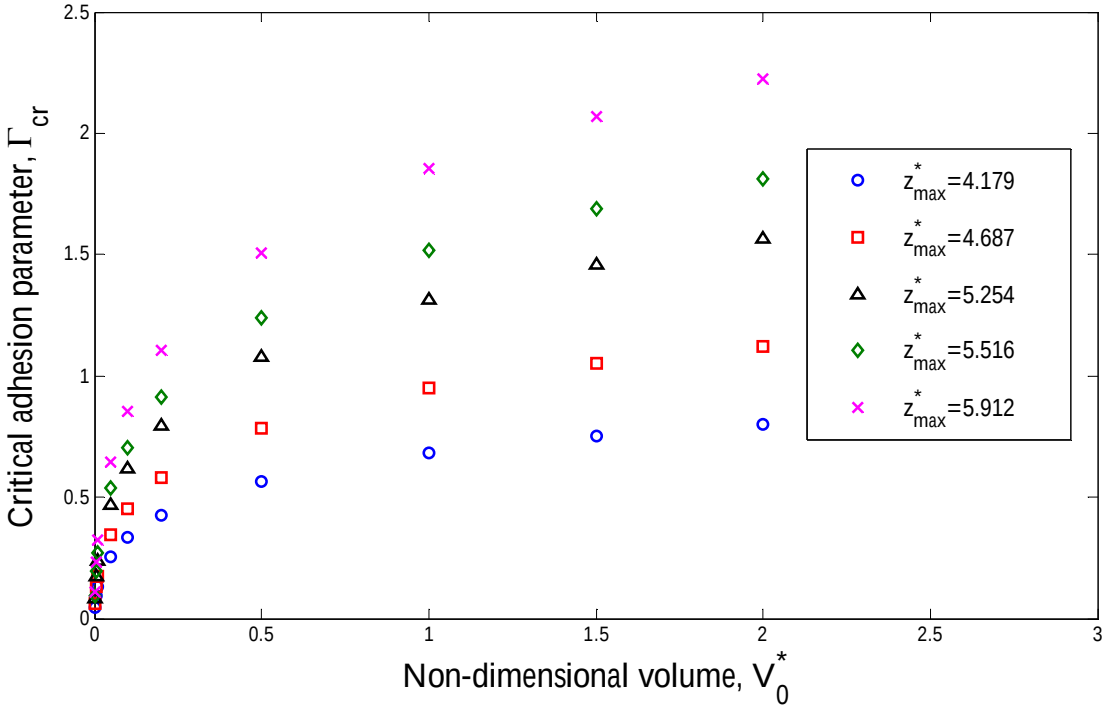

Fig. 2.17 Critical adhesion parameter versus the non-dimensional liquid volumes for different values of non-dimensional maximum surface height.

---

[1] Statistically speaking, depending on the number of nodal points, z_{max}^* will tend to fall within certain bounds. In the current study, we considered 500 surfaces each having 4 million nodal points and the above range represents the total variation observed.

A 3D plot of Γ_{cr} versus $z^*_{\max}$ and V_0^* is shown in Fig. 2.18. Points above the critical surface represent unstable conditions, while those below are stable.

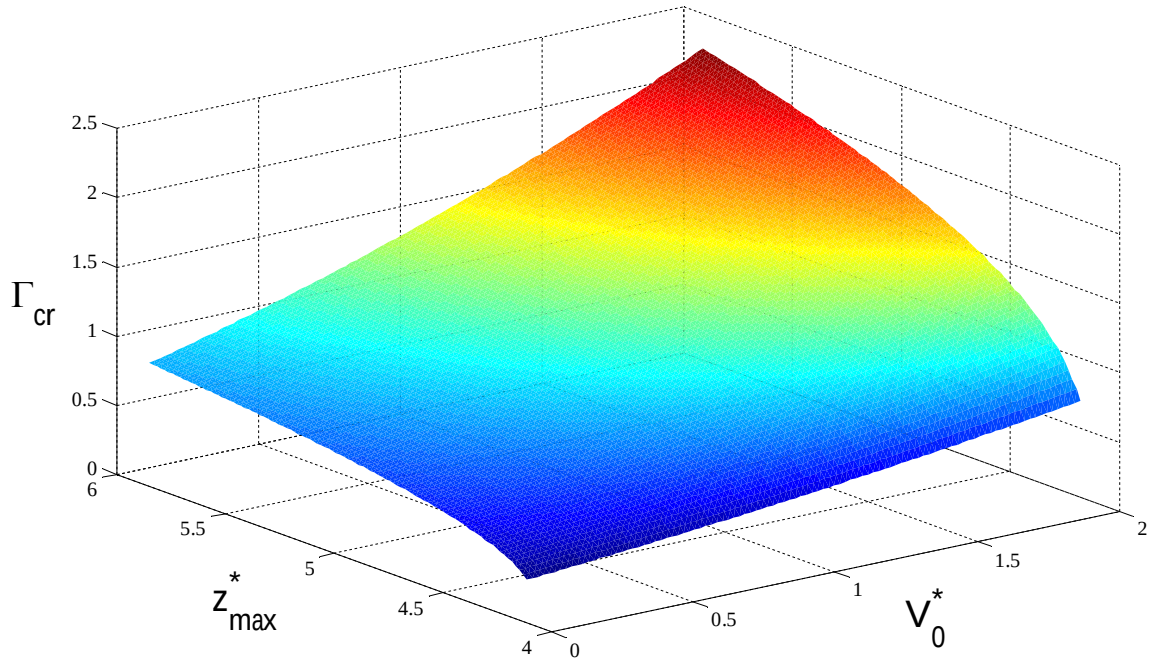

Fig. 2.18 The 3D plot of the critical adhesion parameter versus the non-dimensional liquid volume and non-dimensional maximum surface height for $P^* = 0$.

If the liquid volume, V_0, between the rough surfaces is controlled, the following relation can be obtained for the liquid volume that causes instability, based on Eq. (2.51) via substitution for the non-dimensional parameters

$$\frac{\gamma V_0\left(\cos\theta_A + \cos\theta_B\right)}{\sqrt{2}\pi A_n^{1/2} E'\sigma^3} = 0.011\left(\frac{z_{\max}}{\sigma}\right)^{2.87}\left(\frac{V_0}{A_n\sigma}\right)^{0.32} \tag{2.52}$$

Simplifying and rearranging Eq. (2.52), the following relation can be obtained for the critical liquid volume

$$\left(V_0\right)_{cr} = 0.012\left(\frac{E'}{\gamma\left(\cos\theta_A + \cos\theta_B\right)}\right)^{\frac{1}{0.68}}\left(\frac{z_{\max}}{\sigma}\right)^{4.22} A_n^{\,0.26}\sigma^{3.94} \tag{2.53}$$

Since the practical range for $z^*_{\max}$ is limited, it is better to keep $z_{\max}/\sigma$ as one term, and it denotes that $z_{\max}$ and σ cannot be chosen completely independently. The above expression highlights the role of certain material properties on the critical volume, $\left(V_0\right)_{cr}$, necessary for interface collapse. For example, it shows that the critical volume is quite sensitive to the surface roughness. That is, with $z_{\max}/\sigma$ assumed to be around 5, the critical liquid volume scales approximately with the forth power of σ. It is also observed that the critical volume increases faster than linearly with elastic modulus.

In the presence of external load, P^*, the following relation can be obtained for the critical adhesion parameter, Γ_{cr}, based on extensive number of numerical simulations.

$$\Gamma_{cr} = \frac{1}{\left(8.94V_0^* + 17.15\right) z^{*\,-1.55V_0^{*0.11}}_{\max} P^{*0.85} + \dfrac{1}{0.011\, V_0^{*0.32} z^{*\,2.87}_{\max}}} \tag{2.54}$$

where the range $0 < P^* < 5$ is considered for the dimensionless external load, P^*, the range $4.18 < z^*_{\max} < 5.91$ is considered for the dimensionless surface height, $z^*_{\max}$, and the range $0.05 < V_0^* < 1.5$ is considered for the dimensionless liquid volume, V_0^*. The average relative error between Eq. (2.54) and the numerical data is 2.27 %. If the external load, P^*, is set to zero in Eq. (2.54), it reduces to Eq. (2.51).

A comparison between the numerically obtained critical adhesion parameter, Γ_{cr}, with the curve-fit Eq. (2.54) is shown in Fig. 2.19. In Fig. 2.19, the non-dimensional surface height, $z^*_{\max}$, is constant, and the plots for critical adhesion parameter, Γ_{cr}, versus non-dimensional external load, P^*, are obtained for 6 different values of non-dimensional liquid volume, V_0^*.

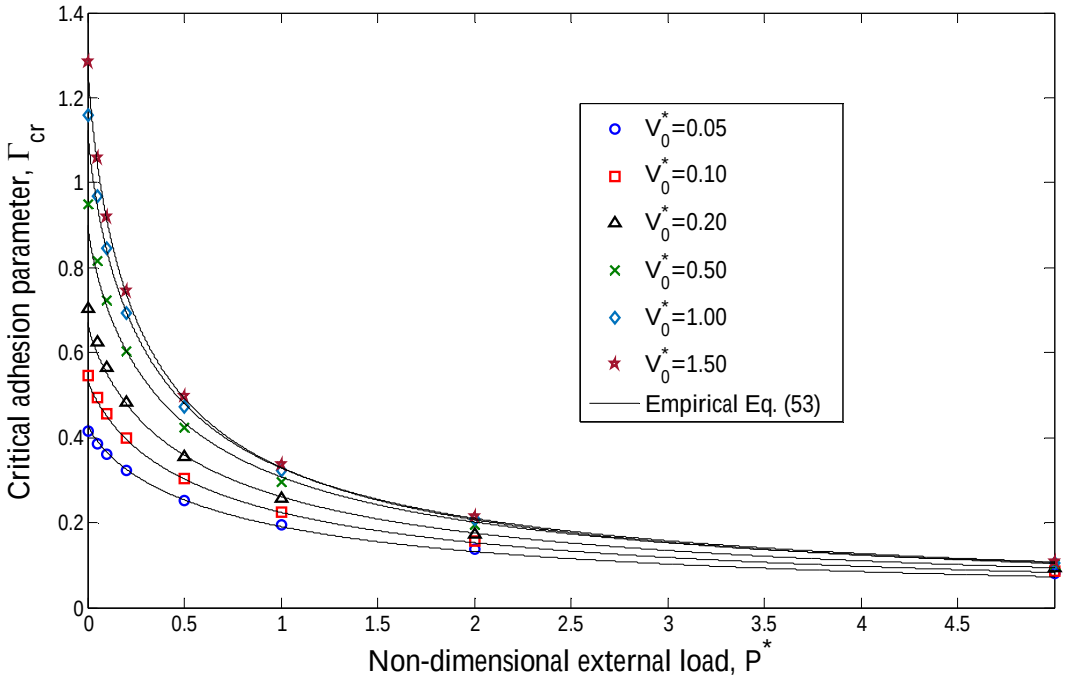

Fig. 2.19 Comparison between critical adhesion parameter results with the Empirical Eq. (2.54).

2.2 Deterministic Approach

In this section, a different contact model, called the deterministic model, is used to account for compressive stresses in the liquid-mediated adhesion between contacting rough surfaces along with the capillary equations governing the tensile stresses. The deterministic model, which is treated as the "exact solution", is based on the calculation of the deformation of each nodal point on the two contacting rough surfaces. Since the calculation of deformation of each point on the contacting rough surfaces is computationally costly, only a few cases are considered in this model. The purpose of this approach is to validate the results obtained based on the JS spectral contact model.

2.2.1 Compressive Stresses

In the current deterministic approach, the influence coefficients are employed to relate the deformation of each point to the contact pressure. The influence coefficients are developed from the surface deformation of a 3D homogeneous, isotropic, elastic half-space under a concentrated force, P, which is given by [60]

$$u(r) = \frac{(1-\nu^2)P}{\pi E r} \tag{2.55}$$

where u is the surface deformation of the half-space (taken to be positive into the body), which is a function of the radial distance, r, from the origin, E, ν are the elastic modulus and Poisson's ratio of the half-space, respectively. The deformation of a 3D homogenous, isotropic, elastic half-space under a uniform pressure p, acting within a circular region of radius a for the case where $r >> a$, can be approximated using Eq. (2.55)

$$u(r) = \frac{(1-\nu^2)pa^2}{Er} \tag{2.56}$$

where $P = \pi a^2 p$ is used in Eq. (2.56). The deformation of the half-space under a uniform pressure is shown schematically in Fig. 2.20.

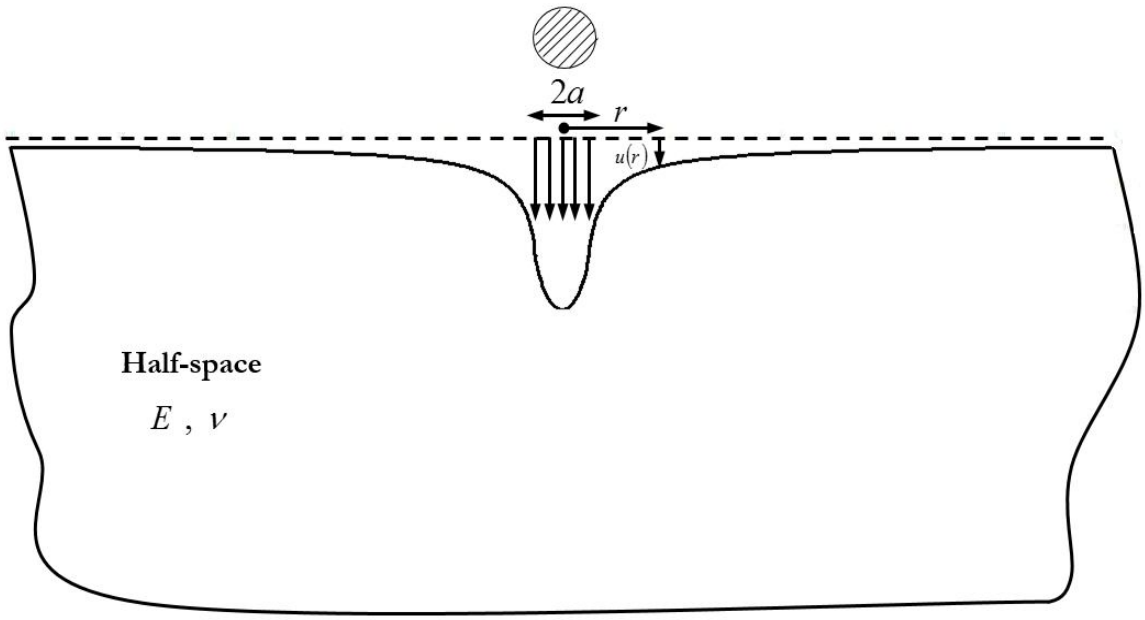

Fig. 2.20 Illustration of surface deformation due to constant pressure over circular region.

It can be shown that Eq. (2.56) only causes 3.3% error compared to the analytical solution derived in [60], when r is just twice a, and more importantly the error is acceptable (14.3%) even for cases with $r = 1.1a$.

In a similar way, it can be assumed that the relation between a uniform pressure acting on a rectangular grid and a nodal deformation is given by

$$u = \frac{(1-\upsilon^2)p\Delta x\Delta y}{\pi Er} \tag{2.57}$$

where r is measured from the center of the rectangular grid, and $\Delta x, \Delta y$ are the grid spacing in x and y directions, respectively. The influence coefficient, C_{ijmn}, which is defined as the deformation at node (i, j) due to a unit pressure at node (m,n), is obtained based on Eq. (2.57) (see Fig. 2.21)

$$C_{ijmn} = \frac{(1-\upsilon^2)\Delta x^2}{\pi E r_{ijmn}} \qquad (i, j) \neq (m,n) \tag{2.58}$$

where it is assumed equal grid spacing in x and y directions $\Delta x = \Delta y$.

when the deformation is needed at the point of application of the pressure, an equation due to Love [61], which is given in [60] is used, leading to

$$C_{ijij} = \frac{4(1-\upsilon^2)\Delta x}{\pi E} \ln\left(1+\sqrt{2}\right) \tag{2.59}$$

Equations (2.58) and (2.59) can be applied to the contact between rough surfaces by using the composite elastic modulus, E'. In this case, the surface deformation, $u(r)$, is the sum of the deformation of the contacting rough surfaces, and p is the contact pressure between the surfaces. In this case, the equivalent roughness is the sum of the roughness of the contacting rough surfaces.

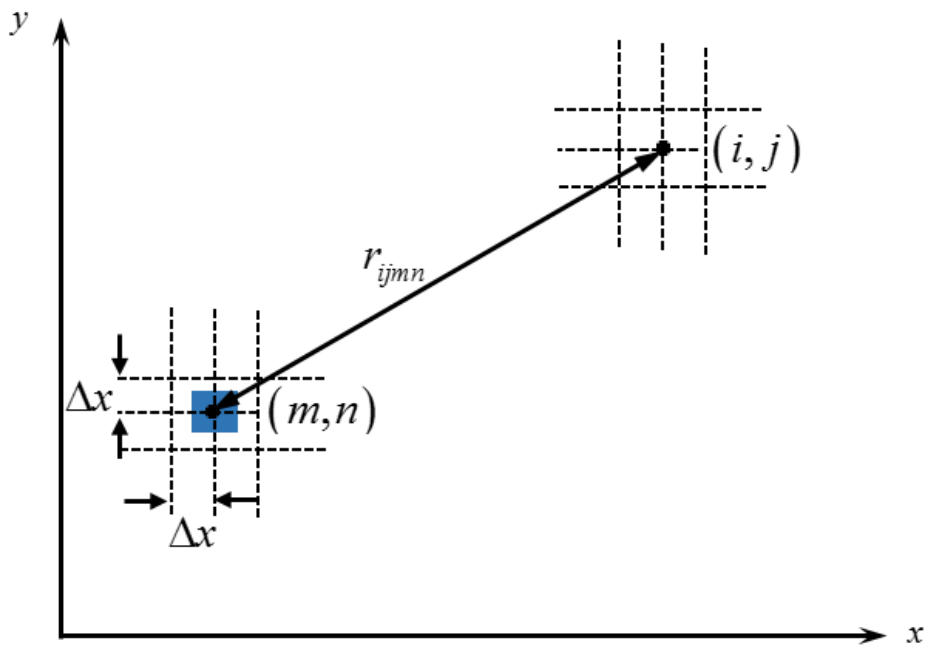

Fig. 2.21 Geometrical definition of key parameters used in influence coefficient formulation of Eqs. (2.58) and (2.59).

2.2.2 Numerical Problem Constraints

The original height of the 3D rough surface at each nodal point is denoted by z_{0ij}, which is selected to have a mean value of zero ($\frac{1}{N^2}\sum_{i=1}^{N}\sum_{j=1}^{N} z_{0ij} = 0$), while the deformed rough surface heights is denoted by z_{ij}. The surface separation, d, is the distance between the rigid flat surface and the mean line of the undeformed rough surface. The nodal contact pressures, p_{ij}, and surface deformations, u_{ij}, are made to satisfy the conditions in Table 2.2 at each of the $N \times N$ nodes (see Fig. 2.22).

Table 2.2 Constraints on the contact model

Condition	*Description*
1. $z_{ij} = z_{0ij} - u_{ij}$	surface height at any point is obtained by subtracting the surface deformation from the height of the undeformed surface at that point.
2. $u_{ij} = \sum_{m=0}^{N}\sum_{n=0}^{N} C_{ijmn} p_{mn}$	the surface deformation at any point can be obtained via influence coefficients and the pressure profile.
3. $z_{ij} = d$	if the point is in solid-solid contact.
4. $z_{ij} < d$	if the point is not in solid-solid contact.
5. $p_{ij} = -\Delta p$	if the point is not in solid-solid contact and it is inside the wetted region.
6. $p_{ij} = 0$	if the point is not in solid-solid contact and it is outside the wetted region.
7. $p_{ij} > 0$	if the point is in solid-solid contact and it is outside the wetted region.
8. $p_{ij} \geq -\Delta p$	if the point is in solid-solid contact and it is inside the wetted region.
9. $V = \pi r_w^2 \bar{h}$	the volume of liquid introduced in the contact region is constant.

$u_{ij} = \sum_{m=0}^{N}\sum_{n=0}^{N} C_{ijmn} p_{mn}$ The problem formulation follows that of Webster and Sayles [62] and Streator [38]. Condition 1 defines the relation between the deformed surface height and the original, undeformed surface height. Condition 2 expresses the relationship between deformation and pressure at each nodal point via the influence coefficients. Condition 3 states that, when a point on the rough surface is in contact with the rigid flat, its height is that of the rigid flat. The penetration of the rough surface into the rigid flat is avoided using Condition 4. Condition 5 states that the pressure for a non-contacting node

inside the wetted region is equal to capillary pressure. A non-contacting node outside the wetted region experiences zero pressure according to Condition 6. Condition 7 states that the pressure of a contacting node outside of the wetted region must be positive, while Condition 8 imposes that a solid-solid contact point inside the wetted region cannot be more negative than the capillary pressure. The conservation of mass is checked by Condition 9.

A comment is in order regarding Condition 8, where contact pressures within the wetted region are allowed to go negative, but no more negative than the capillary pressure. Perhaps a more natural restriction would be to require that all contact pressures be positive. However, implementing this condition tends to destabilize the iteration process. This destabilization seems to occur because there would often be a tremendous change in the pressure at a nodal point within the wetted region whose status changed from contact to non-contact between successive iterates. Hence, from a practical point of view, the present form of Condition 8 is more favorable for achieving convergence. Moreover, it also has a physical justification. The pressure at a given nodal point should represent the average surface pressure within the small surrounding region associated with that nodal point. Generally speaking, this nodal region will not be perfectly smooth but, instead, will have multiple contact points that are ‘‘overlooked’’ by the chosen resolution with which the surface is represented. That being the case, a nodal region in the wetted zone is likely to experience sub-regions of non-contact at the capillary pressure along with other sub-regions of compressive stress due to contact. Therefore, it is quite plausible that the mean pressure of the nodal region could be negative (but not more negative than the capillary pressure).

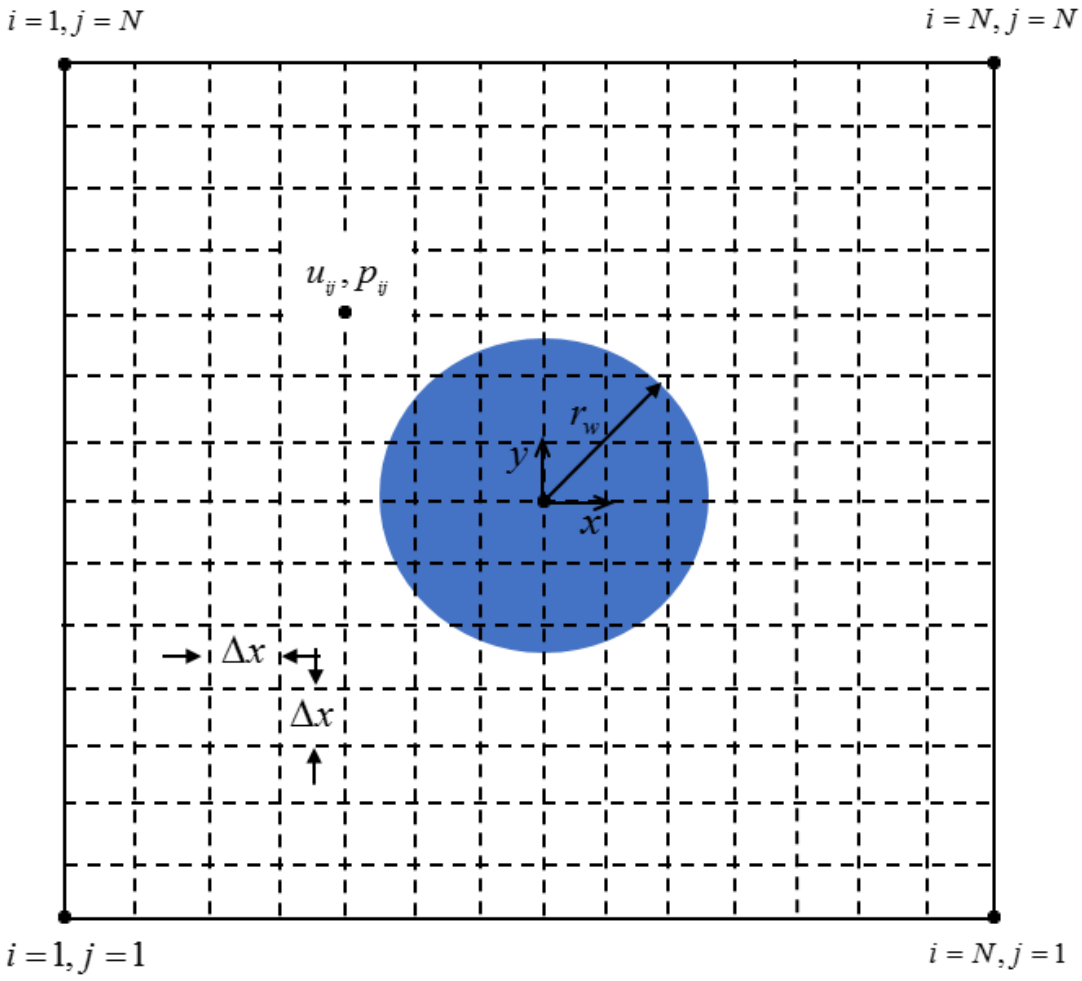

Fig. 2.22 A nodal representation of the contact interface between a rough surface and a rigid flat in the presence of a liquid film.

2.2.3 Numerical Algorithm

The numerical algorithm designed to solve the liquid-mediated adhesion between rough surfaces deterministically is outlined in the flow chart of Fig. 2.23. After introducing the input parameters, including the original surface profile, $z_0(x,y)$, the area of domain of interest, A_n, the external load, P , the material properties such as effective elastic modulus, E' , Poisson's ratio, ν , the surface tension of the liquid film, γ, and the

amount of liquid volume, V_0, an initial guess is made for the level of the rigid flat, d. Based on the initial guess for d, a contact index is assigned to the nodal points. The contact index of the nodal points with height more than d is set to unity suggesting that the nodal point is in contact; otherwise the contact index is set to zero. The surface deformation of the nodal points is adjusted where the contact index is unity so that the height is equal to the surface separation, d. Alternatively, where the contact index is zero, the pressure is set to zero for the nodal points outside the wetted region, and set to the capillary pressure for the nodal points inside the wetted region. Then, the matrix equation defined by the influence coefficients is solved to obtain the value of unknown nodal pressures and deformations. Once the surface deformation and contact pressure for each nodal point in the domain are obtained, the Conditions 4, 7, and 8 are checked to avoid interpenetration, and also to avoid negative pressures outside the wetted region, and pressures more negative than capillary pressure inside the wetted region. Wherever Condition 4 is violated, the contact index of the nodal point with the highest interpenetration is changed from zero to unity. A more natural process might be to adjust the status of all the nodal points of interpenetration to have contact index of unity, but this procedure tends to destabilize the computation. Whenever Conditions 7 and 8 are violated, the contact index is changed from unity to zero; i.e. the nodal point is "taken out" of contact. The iteration proceeds until all of the contact conditions are satisfied for the given interference. Then, the tensile force, F_t, and compressive force, F_c, are calculated by integrating the compressive and tensile stresses corresponding to the assumed surface separation, d. The wetted radius and capillary pressure are updated based on the calculation of the average gap, $\bar{h}$, until the tensile force converges (based on

achieving a relative error of 10^{-5} or less). When the tensile force is converged, the external load residual is calculated using the external load computed from the model, $P_{cal} = F_c - F_t$, and the input external load, P. The location of the rigid flat surface, d, is then updated in each iteration until the compressive force, F_c, balances the combined tensile force, F_t, and the external load, P, on the rigid flat surface. If the normalized external load residual, $\left|P_{cal} - P\right| / F_c$, is below the tolerance (10^{-5}), the program concludes; otherwise an adjustment is made in the assumed separation, d based on secant search algorithm and the process repeats.

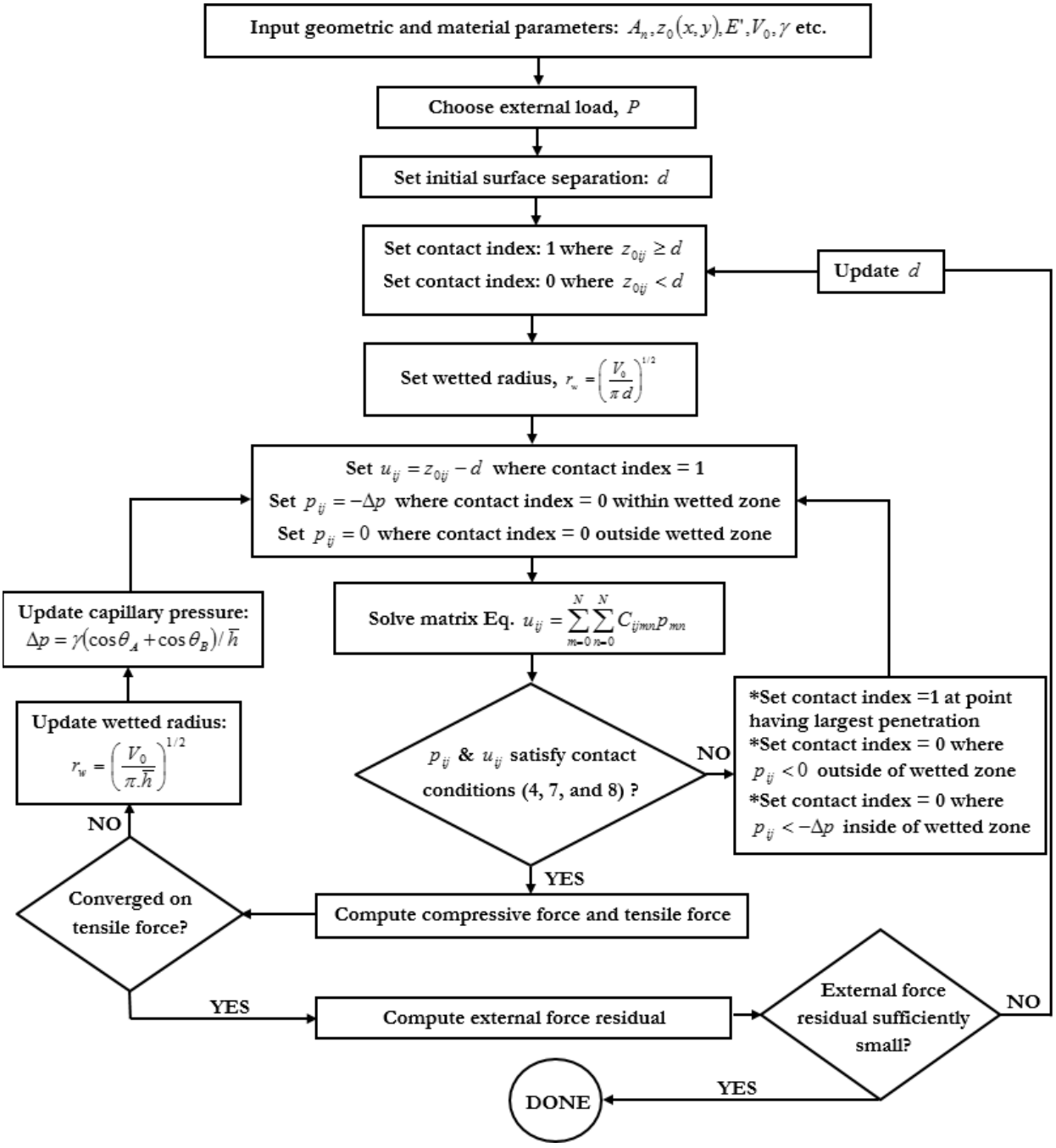

Fig. 2.23 Flowchart of the numerical algorithm.

In this work, the simulated rough surface is obtained employing the same surface profile generation method outlined earlier by Garcia and Stoll [59]. A plot of 4 different Gaussian isotropic rough surface profiles with 101 nodes in each direction generated using this method is outlined in Fig. 2.24, where the surfaces have the same r.m.s. value, $\sigma = 0.4\,\mu$m, but different correlation lengths, l_c . A convergence test was performed on different randomly generated Gaussian isotropic rough surfaces with different number of nodal points, N, which led to the conclusion that the convergence is guaranteed for surfaces with at least 10 nodal points per correlation length, l_c. In this work, Gaussian isotropic rough surfaces with 101 nodal points in each direction ($N = 101$) is considered with correlation length ratio of $l_c / L = 0.1$.

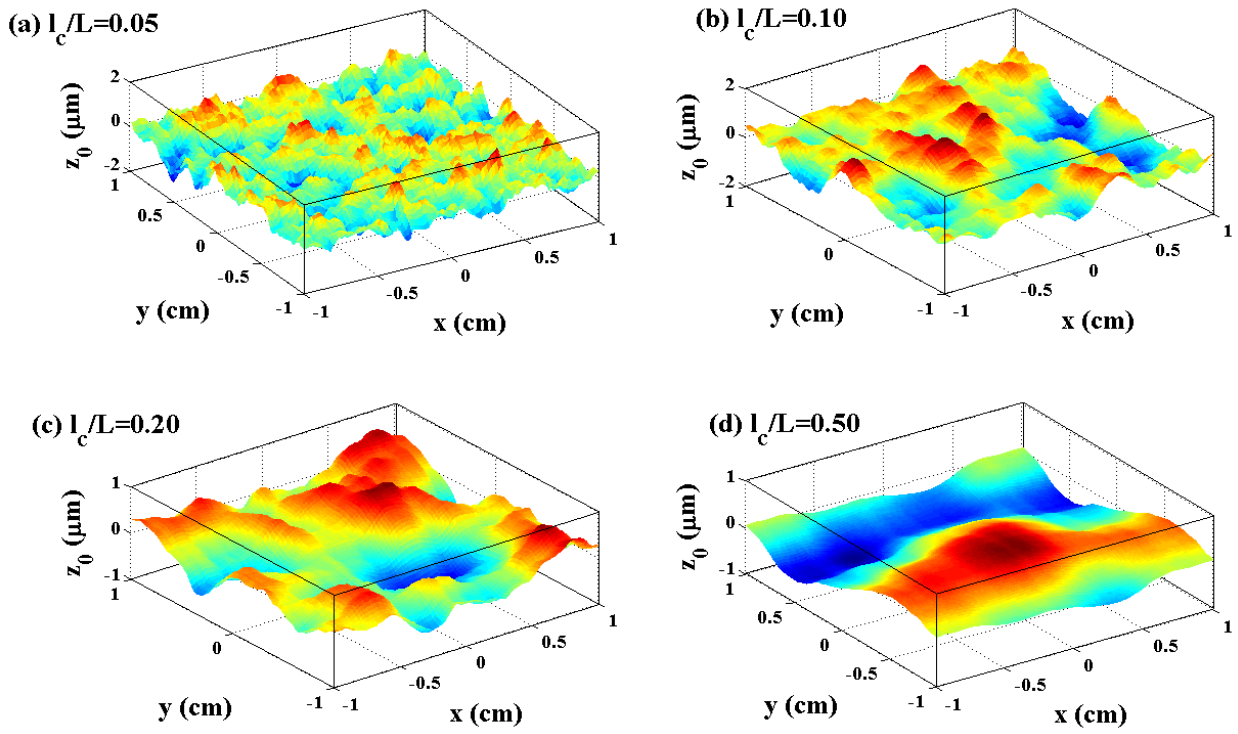

Fig. 2.24 Generated Gaussian isotropic rough surfaces with different values of correlation length ratio, l_c / L : (a) $l_c / L = 0.05$, (b) $l_c / L = 0.10$, (c) $l_c / L = 0.20$, and (d) $l_c / L = 0.50$.

2.2.4 Results

In this section, the numerical results for the 3D deterministic contact model are presented. Unless stated otherwise the computations are performed using the parameter values shown in Table 2.3. Note that the surface tension value considered in this work is that of water at 20℃. For convenience, a zero value is selected for contact angles of the liquid film with upper and lower surfaces, $\theta_{A,B} = 0$. Fig. 2.25 shows the distribution of pressure for a case corresponding to composite elastic modulus E' of 15 GPa and an external load P of zero. In Fig. 2.25, the negative pressure in the central circular region of the nominal contact area shows where the liquid film is located. Positive spikes in the

pressure due to solid-solid contact occur at the various isolated contact points. For the case of zero external load the net tensile force in the circular wetted region balances the net compressive force due from the isolated solid-solid contact spots.

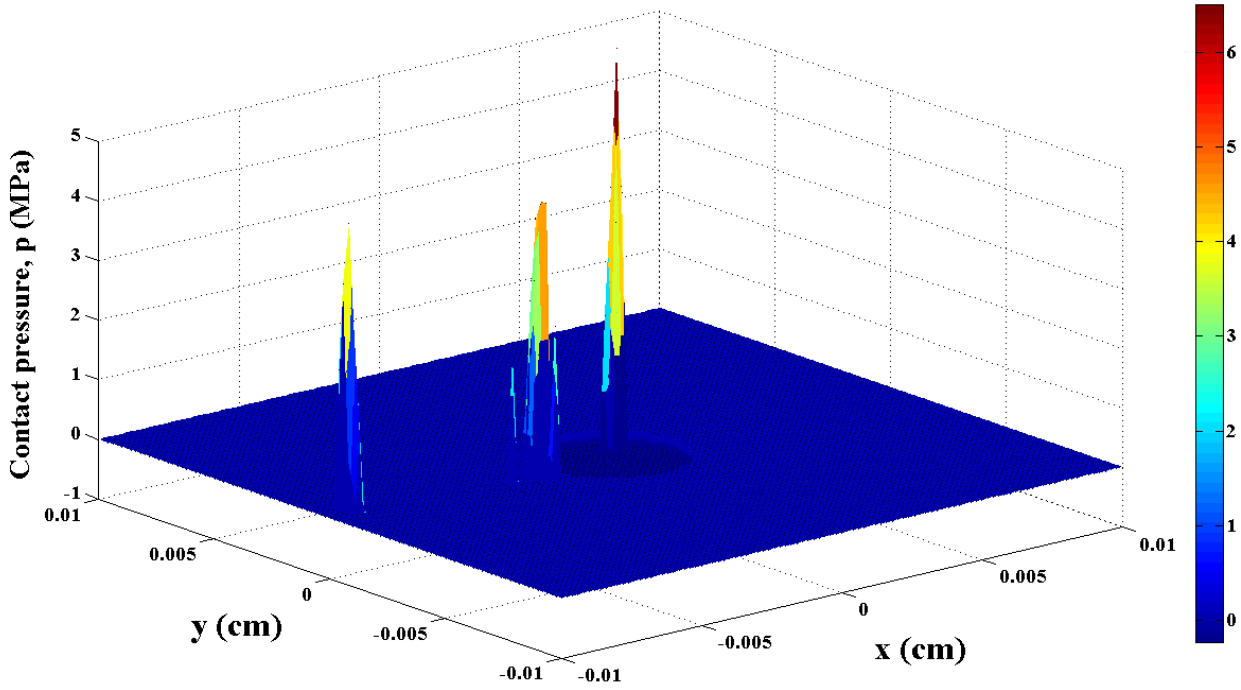

Fig. 2.25 The pressure profile within the nominal contact area in the absence of external load.

The results for the key features of the contact interface such as tensile force, F_t, contact area, A_r, average gap, $\bar{h}$, and wetted radius, r_w, versus the flexibility of the rough surface, $1/E'$, in the case of no external load, $P=0$, are shown in Fig. 2.26 for the reference properties given in Table 2.3.

Table 2.3 Reference properties

Name	Symbol	Value
Liquid volume	V_0	0.01 mm^3
Liquid surface tension	γ	72.7 mN/m
r.m.s. surface roughness	σ	0.4 μm
Auto-correlation length ratio	l_c / L	0.10
Nominal contact area	A_n	4 cm^2

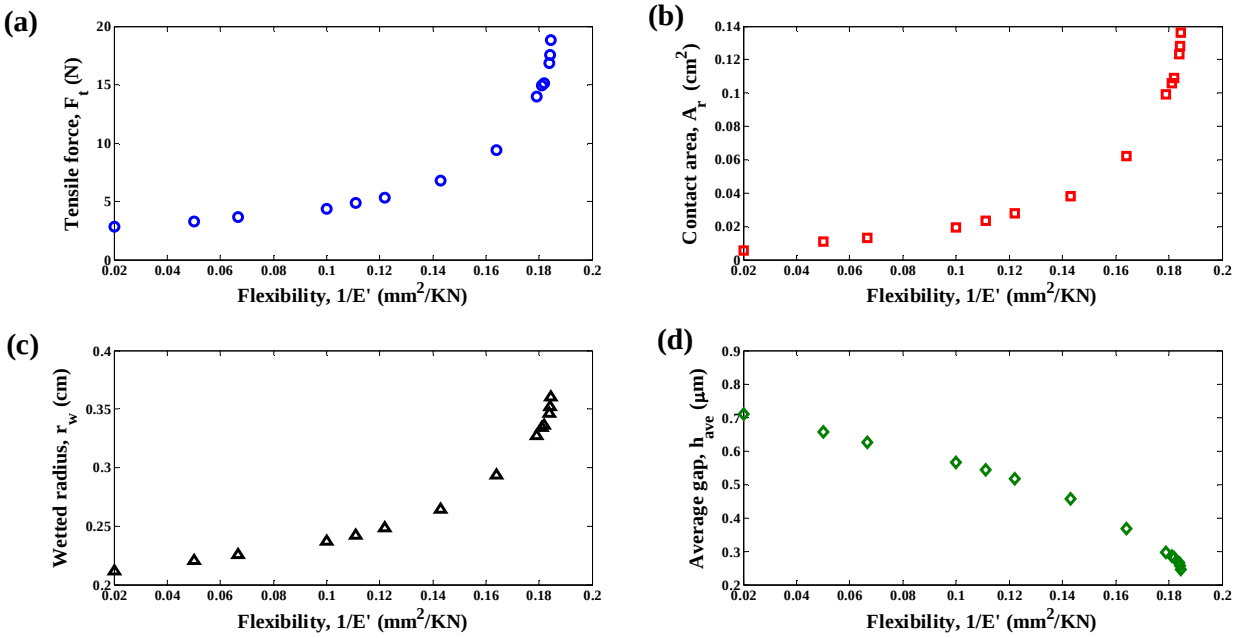

Fig. 2.26 The results for (a) tensile force, (b) contact area, (c) wetted radius, and (d) average gap versus the flexibility of the rough surface.

As results in Fig. 2.26 suggest, the tensile force, F_t, wetted radius, r_w, and contact area, A_r, increase with the flexibility, $1/E'$, of the rough surface while the average gap, $\bar{h}$,

decreases with the increasing surface flexibility. Rough surfaces with higher flexibility experience more deformation under the same total load which cause higher contact area and lower average gap between the contacting surfaces. The reduction in average gap causes the liquid film to spread over a larger area. Both the reduction in the average gap and the increase in the wetted radius boost the increase in the tensile force. These parameters vary with the rough surface flexibility until the curves approaches an approximately vertical slope. The last data point on the curve (to a resolution of 10^{-3} mm^2/kN in the value of flexibility) is taken as the point of instability, and no equilibrium configuration could be obtained for the contact problem for higher values of surface flexibility. It means that the rough surface is too flexible that the compressive force developed at solid-solid contact spots cannot balance the tensile force within the nominal contact area.

A parametric study is performed to analyze the effect of different parameters on the tensile force, F_t, contact area, A_r, and average gap, $\bar{h}$, results. The normalization introduced earlier is also used in this work to present the results. Fig. 2.27 displays the results for the normalized tensile force, F_t^*, versus the adhesion parameter, Γ (Eq. 2.45), for $V_0^* = 0.0625$ and $P^* = 0$, for selected parameter values falling within the ranges given in Table 2.3 (Note that the maximum selected value of surface tension is representative of some molten metals). The legend of Fig. 2.27 reveals which parameter or pair of parameters is being varied for a particular set of data points. It can be seen from Fig. 2.27 that the chosen normalization works quite well in generalizing the results.

Table 2.4 Overview of the parameter ranges used for simulations.

Name	Symbol	Range
Elastic modulus	E'	1-50 GPa
Liquid surface tension	γ	10-500 mN/m
r.m.s. surface roughness	σ	0.1-2 μm
Liquid volume	V_0	0.001-0.1 cm^3

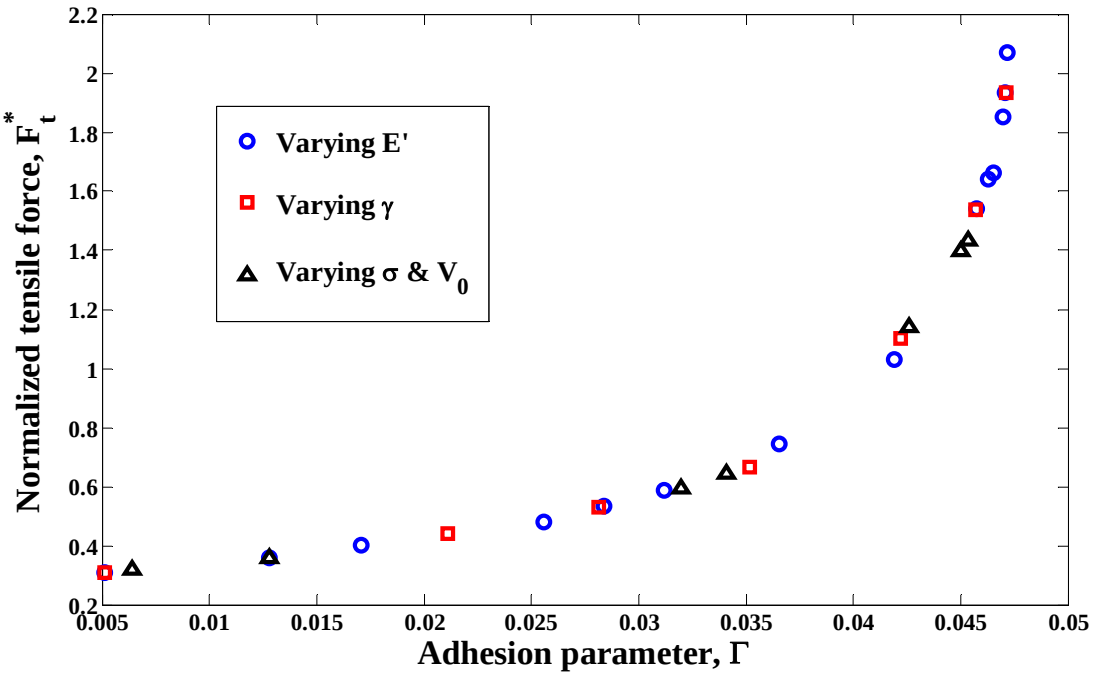

Fig. 2.27 Normalized tensile force results versus adhesion parameter for the range of parameters given in Table 2.3.

The results for the normalized tensile force, F_t^*, versus the adhesion parameter, Γ, for different values of normalized liquid volume, V_0^*, in the absence of external load

($P^* = 0$) are shown in Fig. 2.28. As expected, the normalized tensile force increases with the adhesion parameter, Γ, for different values of the normalized liquid volume, V_0^*, until it reaches a near vertical slope, suggestive of surface collapse. As the normalized liquid volume increases, the instability occurs at higher values of the adhesion parameter; also, the normalized tensile force at the point of instability decreases as the normalized liquid volume increases.

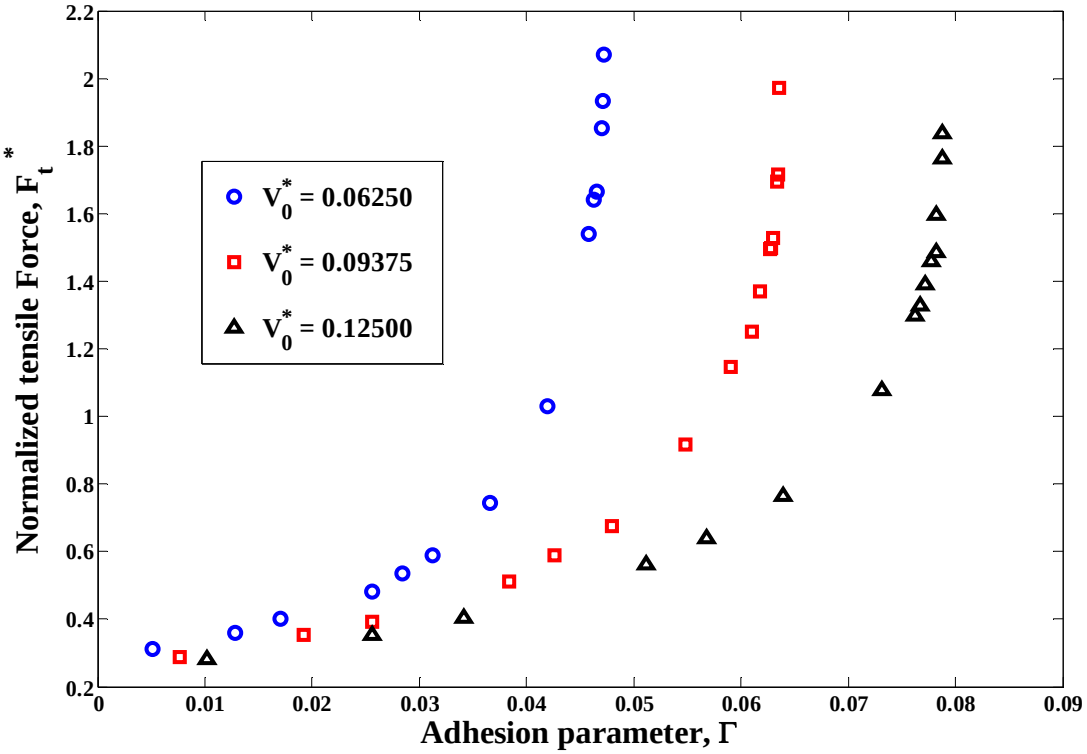

Fig. 2.28 Normalized tensile force results versus adhesion parameter for different values of normalized liquid volume.

Results for the normalized average gap, h^*, versus the adhesion parameter, Γ, are shown in Fig. 2.29 for different values of normalized liquid volumes, V_0^*. As observed in Fig. 2.29, the normalized average gap, h^*, decreases as the adhesion parameter, Γ,

increases until the slope of the curve becomes near vertical. The instability occurs at higher values of adhesion parameter, Γ, as the liquid volume, V_0^*, increases, also the normalized average gap at the point of instability increases as the normalized liquid volume increases.

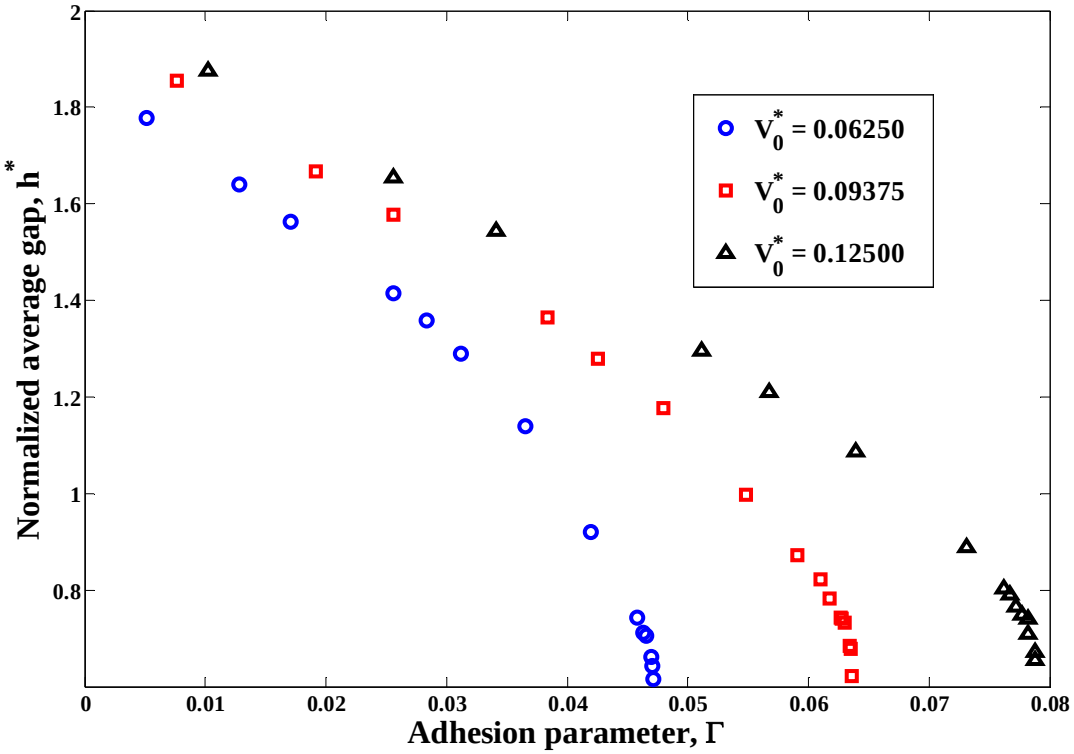

Fig. 2.29 Normalized average gap results versus adhesion parameter for different values of normalized liquid volume.

The results for normalized contact area, A_r^*, versus the adhesion parameter, Γ, are shown in Fig. 2.30, for different values of normalized liquid volume, V_0^*. As the normalized liquid volume, V_0^*, increases, the normalized contact area, A_r^*, at the point of instability increases (Fig. 2.30). As it can be seen from Fig. 2.30, the ratio of real contact

area to nominal contact area is small even for values of adhesion parameter near the instability point ($A_r^* = A_r / A_n < 6\%$).

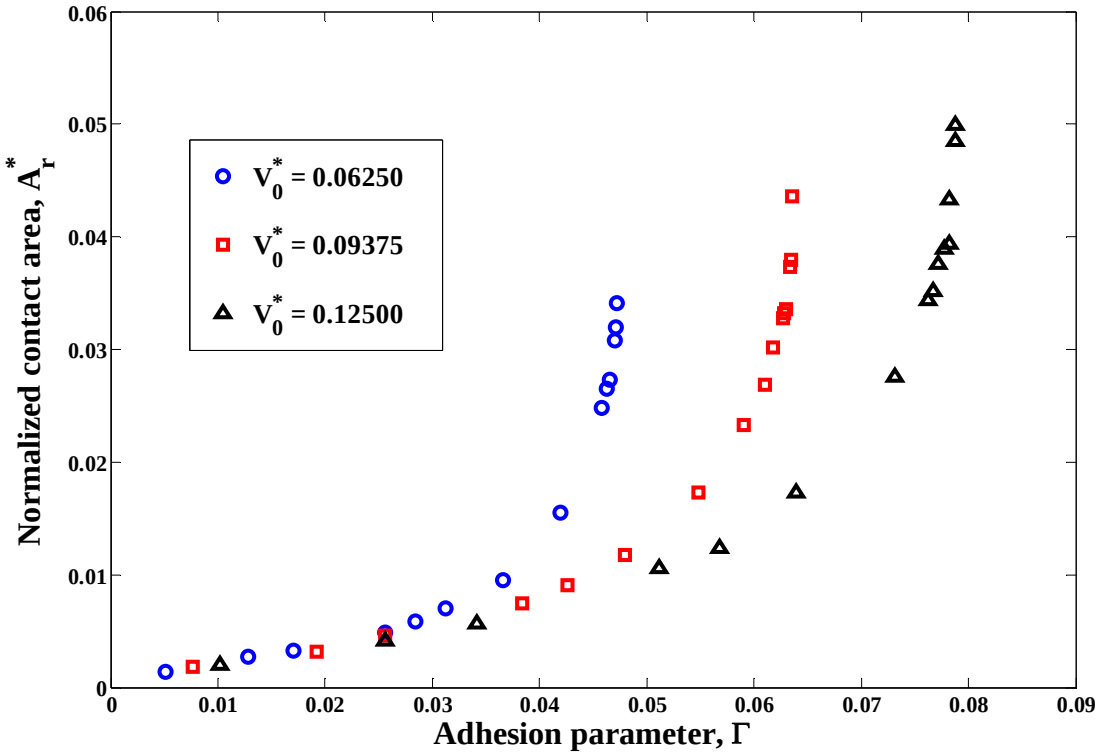

Fig. 2.30 Normalized contact area results versus adhesion parameter for different values of normalized liquid volume.

Fig. 2.31 shows the results for the normalized tensile force, F_t^*, versus the adhesion parameter, Γ, for different values of normalized external load, P^*. A constant value is selected for the normalized liquid volume for all cases in Fig. 2.34 ($V_0^* = 0.0625$). It can be seen in Fig. 2.31, as the normalized external load, P^*, increases the instability occurs at lower values of the adhesion parameter, Γ. Also, the normalized tensile force, F_t^*, at the point of instability increases as the normalized external load, P^*, increases.

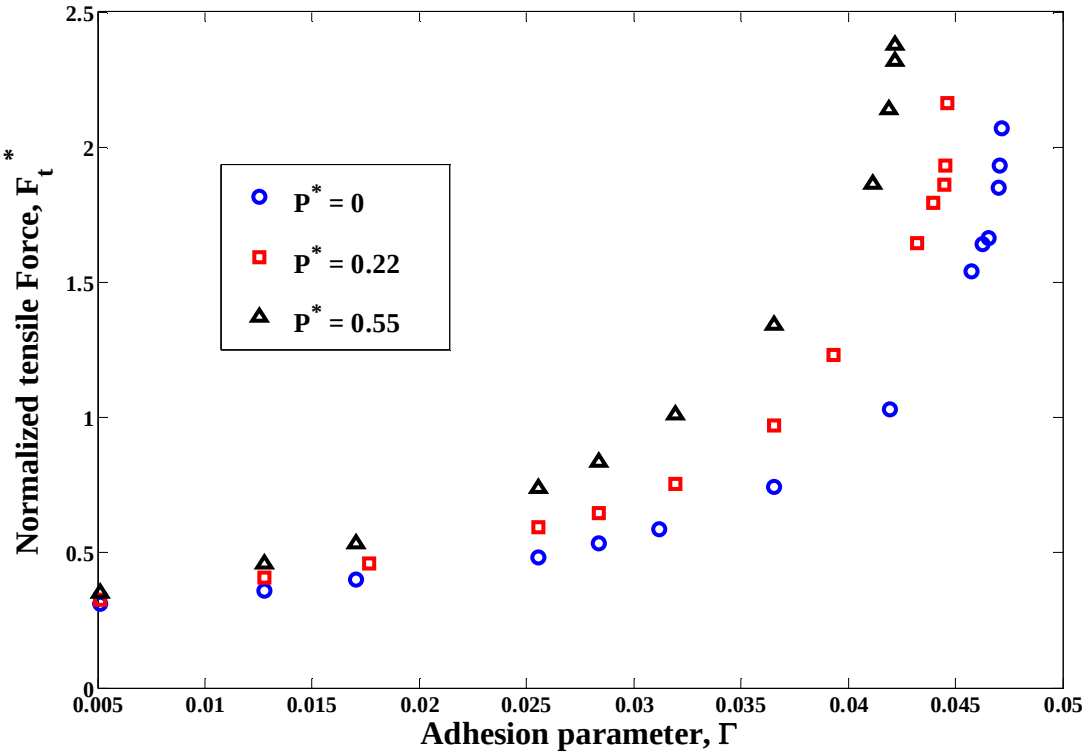

Fig. 2.31 Normalized tensile force results versus adhesion parameter for different values of normalized external load.

Results for the normalized average gap, h^*, versus the adhesion parameter, Γ, are shown in Fig. 2.32 for different values of normalized external load, P^*. As the adhesion parameter, Γ, increases, the normalized average gap, h^*, between the two surfaces decreases until it reaches an approximate vertical slope. It can be seen that the instability happens at lower values of the adhesion parameter, Γ, as the normalized external load, P^*, increases. Also, Fig. 2.32 shows that as the normalized external load, P^*, increases, the normalized average gap, h^*, at the point of instability decreases.

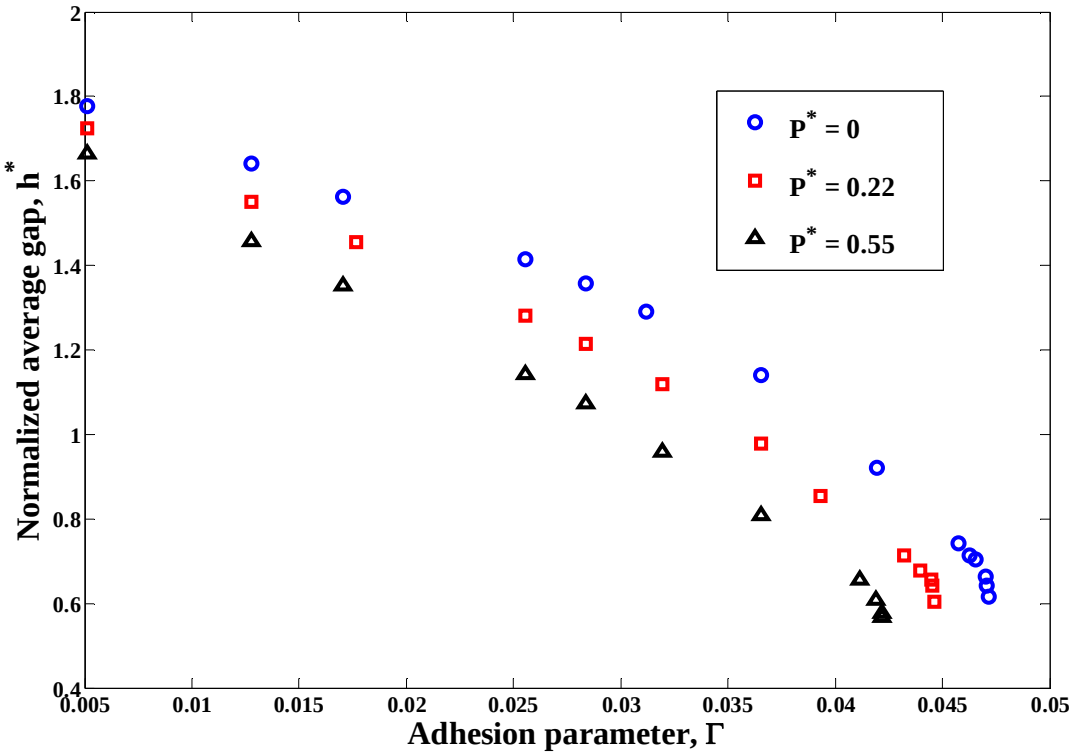

Fig. 2.32 Normalized average gap results versus adhesion parameter for different values of normalized external load.

The results for normalized contact area, A_r^*, versus the adhesion parameter, Γ, are shown in Fig. 2.33, for different values of normalized external load, P^*. As the normalized external load, P^*, increases, the normalized contact area, A_r^*, at the point of instability increases (Fig. 2.33). As it can be seen from Fig. 2.33, the ratio of real contact area to nominal contact area is small even for values of adhesion parameter near the instability point ($A_r^* = A_r / A_n < 5\%$).

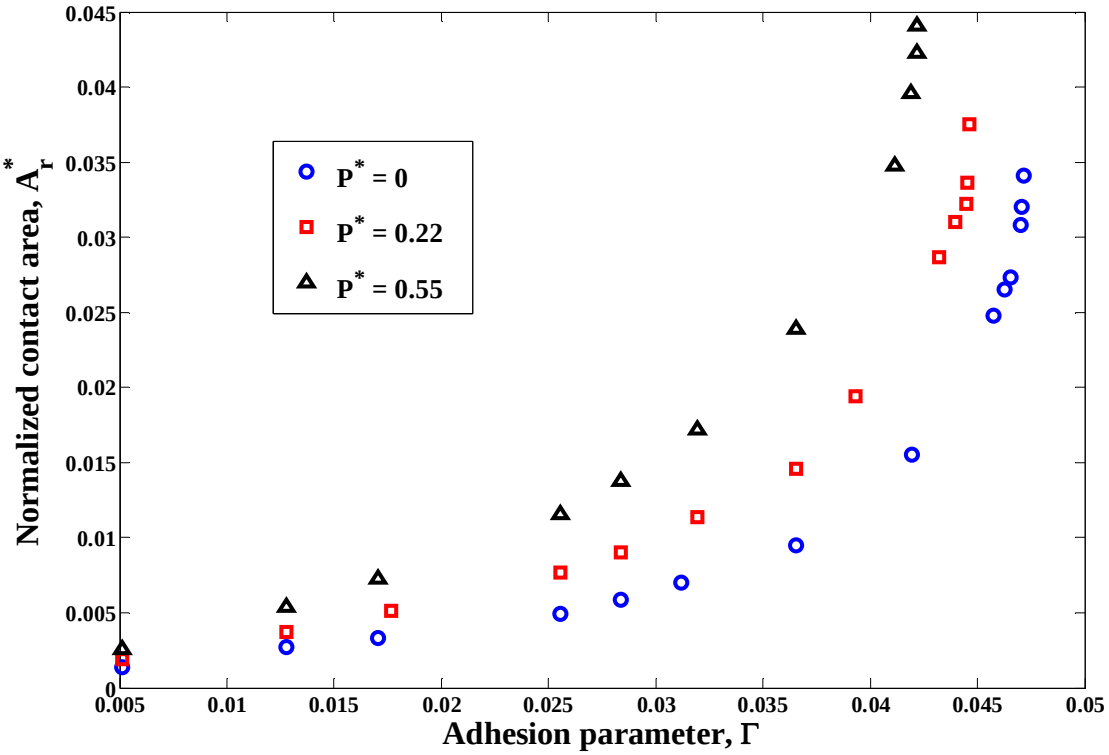

Fig. 2.33 Normalized contact area results versus adhesion parameter for different values of normalized external load.

2.3 Comparison between Spectral and Deterministic Approaches

A comparison between the critical adhesion parameter, Γ_{cr}, predicted by the deterministic model and the spectral model is shown in Fig. 2.34. The two models are applied to the same simulated 3D rough surface used in the current work (Surface 1) and a new simulated surface with the same values of r.m.s. roughness and correlation length (Surface 2). As explained earlier, the Rostami and Streator spectral model is based on characterizing the rough surface in different scales of roughness using a fast Fourier transform (FFT) of the surface heights. It can be seen from Fig. 2.34, that the two models show the same trend for the critical adhesion parameter, Γ_{cr}, versus the normalized

liquid volume, V_0^*, and the normalized external load, P^*, but with quantitative differences. Note that for Surface 1, the current deterministic model predicts lower values of Γ_{cr} than does the spectral model, whereas for Surface 2, the opposite is true.

The quantitative difference between the two model predictions can perhaps be explained, noticing that the deterministic model is restricted in the number of nodal points (surface data) due to computational cost, which overlooks the effect of higher resolution data in the calculations. Also, results of the deterministic model depends on the spatial distribution of the peaks and valleys (at various scales), something that is not included in the spectral description (which is based simply on the amplitude versus wavelength profile).

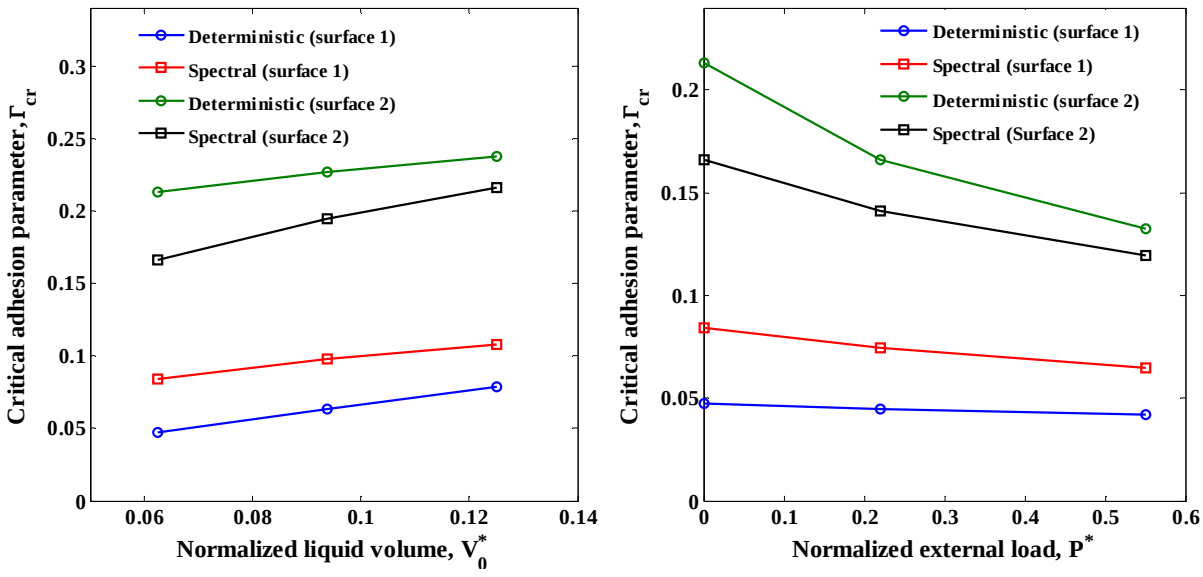

Fig. 2.34 Critical adhesion parameter predicted by deterministic and spectral models versus (a) normalized liquid volume and (b) normalized external load for surfaces 1 and 2.

2.4 Experiments

In this section, an experimental approach is discussed to investigate the tensile (adhesive) force and liquid film spread in the liquid-mediated adhesion between two contacting rough surfaces. Two different experimental approaches, i.e. 1. Pull-off test and 2. Friction force test, are used to measure the tensile force between surfaces. The results are presented for different values of intervening liquid volume, and surface roughness. Also, a digital camera is used to record images of the contact interface and image processing is performed on the images to measure the liquid film spread or wetted area between the two contacting surfaces. Each test is explained in further details in the following sections.

2.4.1 Pull-Off test

The pull-off test is performed to measure the force required to separate two contacting surfaces in the presence of liquid film. The basic concept is illustrated in Fig. 2.35. The external load, P_{ext}, is applied between the two surfaces until they lose contact. The pull-off force, F_p, is defined as the equilibrium tensile force, F_t, between two surfaces immediately before they lose contact. The pull-off force is an indication of tensile (adhesive) force between the contacting surfaces, but, it does not necessarily represent the maximum tensile force between the surfaces.

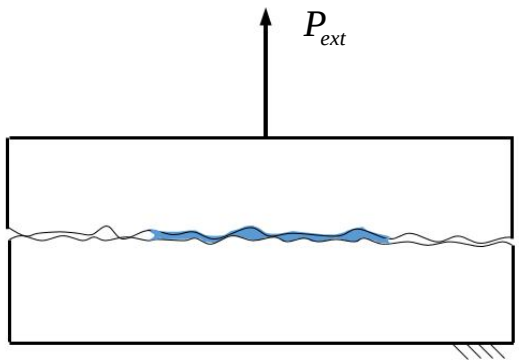

Fig. 2.35 Interface subjected to a separating external load.

2.4.1.1 Pull-off point

The pull-off point corresponds to the moment that the two contacting surfaces in the presence of liquid film lose contact. The estimation of the pull-off point can be obtained from the spectral approach developed for the liquid mediated adhesion between contacting rough surfaces. In this case, an external load, P_{ext}, is applied between the two surfaces and acts in the direction to separate the two surfaces. As P_{ext} increases, the average gap, $\bar{h}$, between the two surfaces also increases. Both the compressive force, F_c, and the tensile force, F_t, between the two surfaces decreases with decreasing average gap, $\bar{h}$. The pull-off force between the two surfaces is applied by using a spring and hook which is connected to the center of the upper surface. A schematic of the pull-off test is shown in Fig. 2.36.

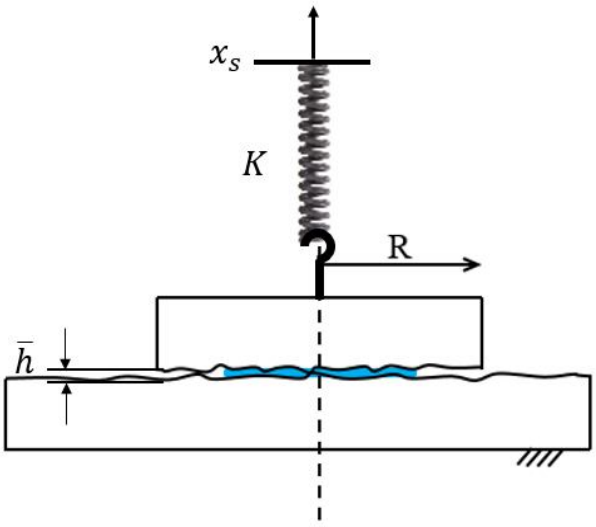

Fig. 2.36 Schematic of the pull-off process.

The location of the top of the spring is denoted by x_s. The initial location of top of the spring, x_{s0}, corresponds to the case where the average spacing between the surfaces is equal to the maximum surface roughness, $z_{\max}$, where there is no liquid film between the contacting surfaces. As the external load, P_{ext}, is applied between the two surfaces, the top of the spring moves in the upward direction. The relation between the external load, P_{ext}, and the average gap, $\bar{h}$, for any position, x_s, of the spring is linear, $P_{ext} = K(x_s - x_{s0}) - K(\bar{h} - z_{\max})$, where the slope of the line is equal to K, which is the spring constant. The term $x_s - x_{s0}$ shows the change in the location of top of the spring, and $\bar{h} - z_{\max}$ shows the change in the location of the bottom of the spring or the upper surface. . The average spacing $\bar{h}_i$, corresponds to the case where the compressive force, F_c, balances the tensile force, F_t, and therefore $F_t - F_c = 0$. A qualitative account of the pull-off process associated with the system of Fig. 2.36 is depicted in Fig. 2.37. The position of the upper end of the spring is prescribed by the stage and each dashed green line reveals how the external load P_{ext} varies with changes in the average spacing, $\bar{h}$, for a fixed x_s. The dashed black curve provides the difference between the tensile force and the compressive force ($F_t - F_c$), which must equate with the external load at equilibrium. Thus, the intersection of the given green dashed line with the black dashed curve establishes the equilibrium average spacing, $\bar{h}$, for a given stage position x_s. By considering perturbations in the average gap about equilibrium it can be seen that the equilibrium points are stable until the compressive force becomes zero. At this point,

a small increase in the average gap causes the external load to exceed the net downward load ($F_t - F_c$). Thus the gap will further increase, leading to pull-off.

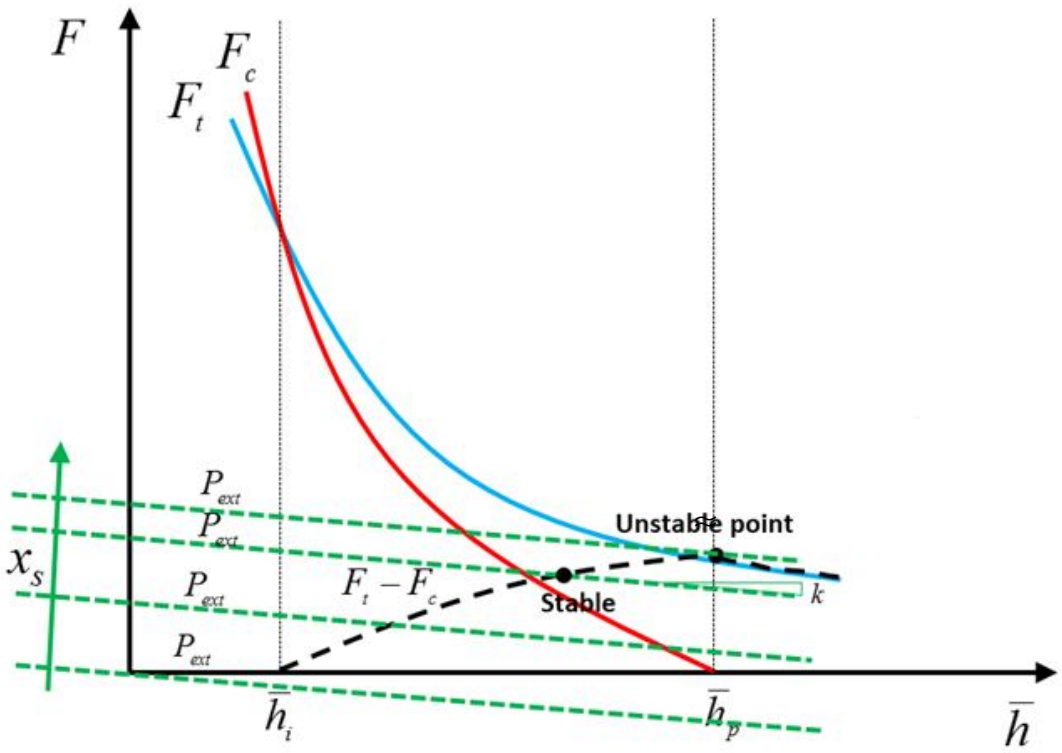

Fig. 2.37 Dependence of tensile force, compressive force, and external load with the average gap.

At the critical point, where the compressive stresses vanish, the tensile stresses are the only source of deformation, and we have from Eq. (2.34)

$$\bar{h}_p = z_{\max} - \frac{\Delta V_t}{\pi r_w^2} \tag{2.60}$$

where $\bar{h}_p$ is the average gap corresponding to the pull-off point. Substituting for ΔV_t from Eq. (2.30), we have

$$\bar{h}_p = z_{\max} - \frac{16\gamma\left(\cos\theta_A + \cos\theta_B\right)}{3\pi\bar{h}E^*} r_w \tag{2.61}$$

Substituting for wetted radius, r_w from $V_0 = \pi r_w^2 \bar{h}$, we have

$$\bar{h}_p = z_{\max} - \frac{16\gamma\left(\cos\theta_A + \cos\theta_B\right)V_0^{1/2}}{3E^*\pi^{3/2}\bar{h}_p^{3/2}} \tag{2.62}$$

Rearranging Eq. (2.62) we have

$$\left(\frac{\bar{h}_p}{z_{\max}}\right)^{5/2} - \left(\frac{\bar{h}_p}{z_{\max}}\right)^{3/2} + \frac{16\gamma\left(\cos\theta_A + \cos\theta_B\right)V_0^{1/2}}{3E^*\pi^{3/2}z_{\max}^{5/2}} = 0 \tag{2.63}$$

It can be seen from Eq. (2.63) that the normalized average gap, $h_p^* = \bar{h}_p / z_{\max}$, is a function of the normalized adhesion parameter $\Gamma' = \frac{16\gamma\left(\cos\theta_A + \cos\theta_B\right)V_0^{1/2}}{3E^*\pi^{3/2}z_{\max}^{5/2}}$. The plot for the normalized gap, h_p^*, versus the adhesion parameter, Γ', is shown in Fig. 2.38.

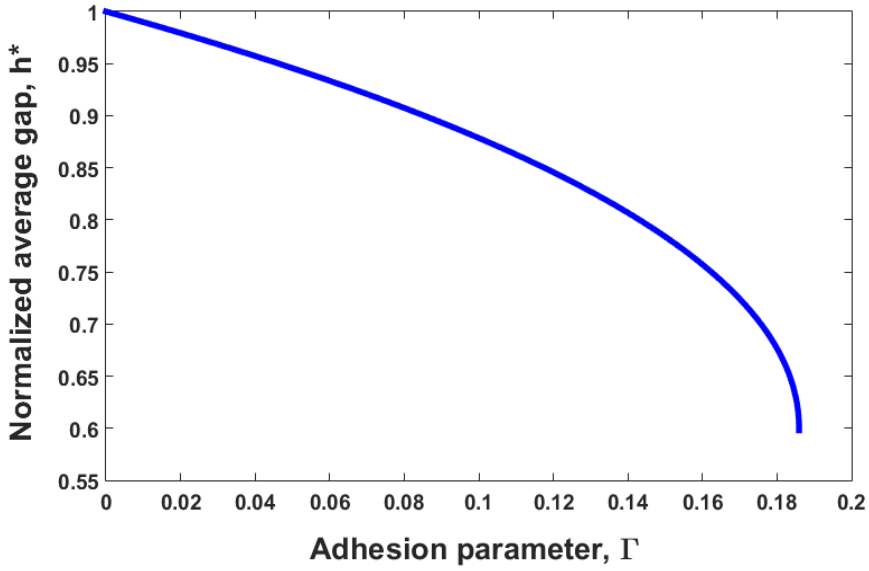

Fig. 2.38 The results for the normalized average gap, h_p^*, versus the adhesion parameter, Γ'.

It can be seen from Fig. (2.38), that no equilibrium normalized gap, h_p^*, can be found for the adhesion parameter, $\Gamma > 0.1859$. Curve-fitting to the results of the Fig. (2.38)

$$h_p^* = \left(\frac{0.1859 - \Gamma}{1.295} \right)^{\frac{1}{2.133}} + 0.598 \tag{2.64}$$

Then, the pull-off force is given by

$$F_p = \Delta p.A_w = \frac{\gamma\left(\cos\theta_A + \cos\theta_B\right)}{\bar{h}_p} \pi r_w^2 = \frac{\gamma V_0\left(\cos\theta_A + \cos\theta_B\right)}{\bar{h}_p^{\,2}} \tag{2.65}$$

Introducing the normalized format of the pull-off force

$$F_p^* = \frac{F_p}{\gamma V_0\left(\cos\theta_A + \cos\theta_B\right)/ z_{\max}^{\,2}} = \left(\frac{z_{\max}}{\bar{h}_p} \right)^2 = h_p^{*-2} \tag{2.66}$$

Substituting for h_p^* from Eq. (2.64) in Eq. (2.66)

$$F_p^* = \left(\left(\frac{0.1859 - \Gamma}{1.295} \right)^{\frac{1}{2.133}} + 0.598 \right)^{-2} \tag{2.67}$$

The plot for the normalized pull-off force F_p^* versus the adhesion parameter, Γ, is shown in Fig. 2.39. It can be shown that the maximum value of normalized pull-off force can be achieved is $F_{p\max}^* = 2.8$, where the maximum pull-off force can be calculated by $F_{p\max} = 2.8\gamma V_0\left(\cos\theta_A + \cos\theta_B\right)/ z_{\max}^{\,2}$.

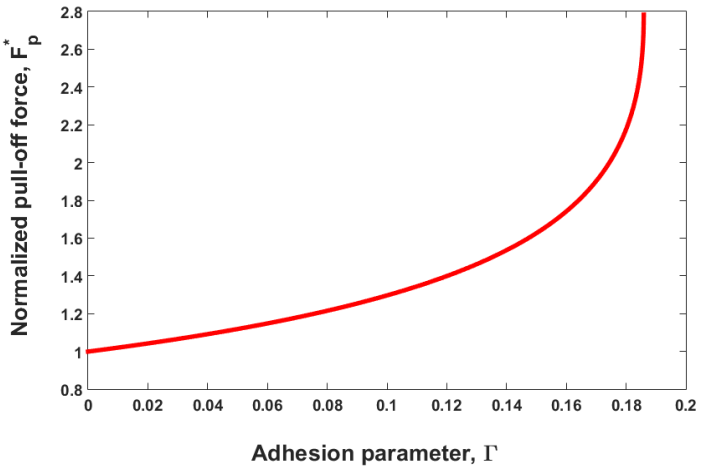

Fig. 2.39 The results for the normalized pull-off force, F_p^*, versus the adhesion parameter Γ.

2.4.1.2 Experimental Setup

The experimental setup used to measure the pull-off force between contacting rough surfaces in the presence of liquid film is shown in Fig. 2.40. The setup consists of a vertical stage, mounting plate, force gauge, L-shaped screw-in hook spring, contacting surfaces, and liquid film. The force gauge is fixed on the vertical stage by the mounting plate which moves in the upward and downward directions. A spring is used to link the force gauge to the top surface. The bottom surface is fixed on the table. A known amount of liquid film is deposited on top of the bottom surface. The top surface is moved in the downward direction using the vertical stage, makes the contact with the bottom surface under enough resting time for the liquid film to spread between the surfaces, and then is moved in the upward direction until the separation happens.

Fig. 2.40 Experimental setup to measure the pull-off force.

The liquid film used for the experiments, PSF-200cSt, is a Pure Silicone Fluid (PSF). These lubricants are clear, colorless and odorless linear 100% Polydimethylsiloxane Silicone Fluids/PDMS Silicone oils that has a variety of viscosities. The surface tension, γ, of the PSF-200cSt is 21 mN/m.

2.4.1.3 Results

The results for the pull-off force, F_p, obtained from the experiments for different material of contacting surfaces, different liquid film volumes, V_0, and different surface roughness are presented in this section. The effect of relative humidity of the environment on the amount of liquid volume between the contacting surfaces, is neglected here. Based on the argument in [63], the establishment of thermodynamic equilibrium for the formation of liquid film due to humidity needs a considerable amount of time, such as hours, or even days. In the interim, the adhesive forces will be dictated

by the current amount of liquid within the interface. The roughness of the contacting surfaces is obtained by performing profilomtery. A stylus profilometer is used to measure the surface roughness as is shown in Fig. 2.41. The surface roughness for different steel disks and fused silica glass are shown in Fig. 2.42.

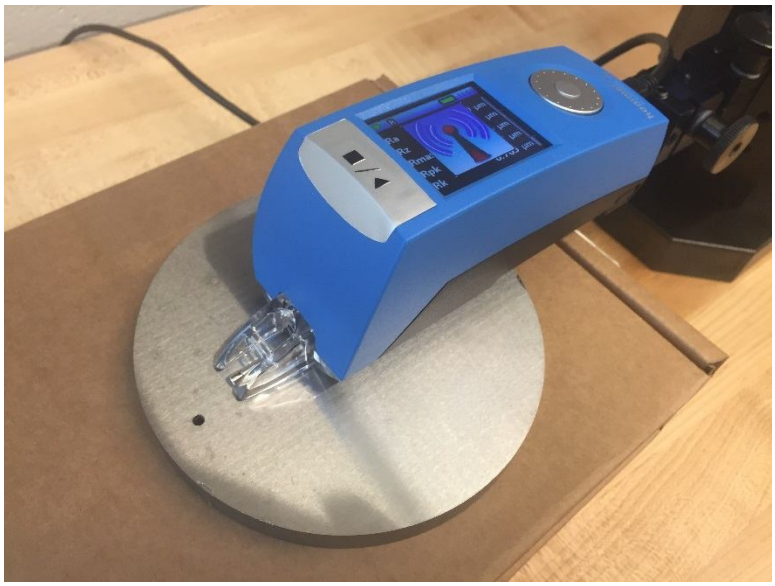

Fig. 2.41 Stylus profilometer used to measure the surface roughness.

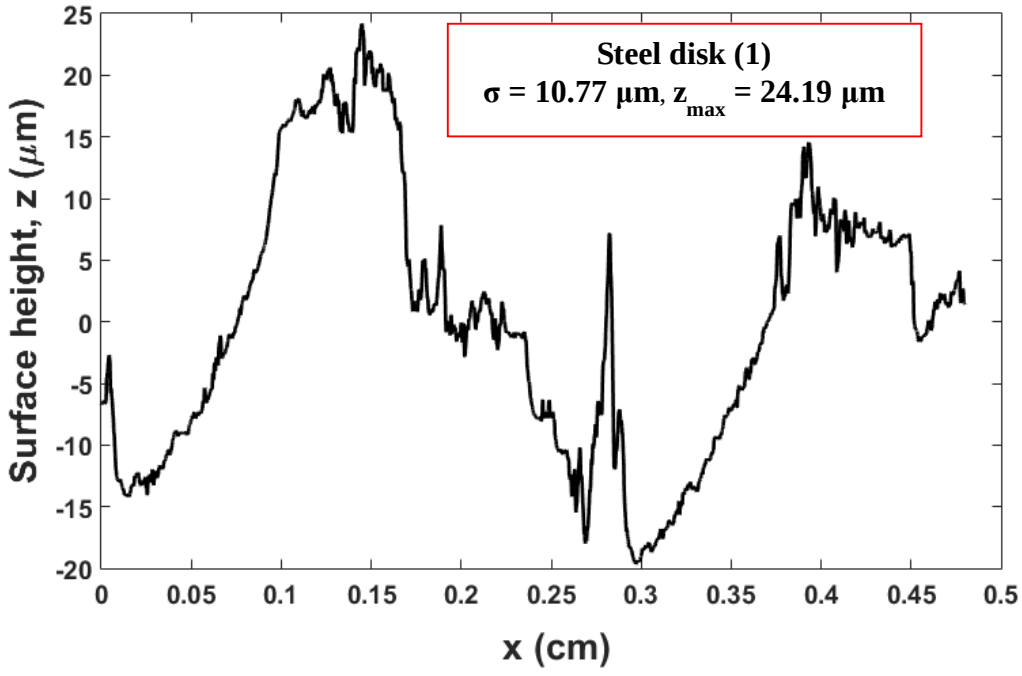

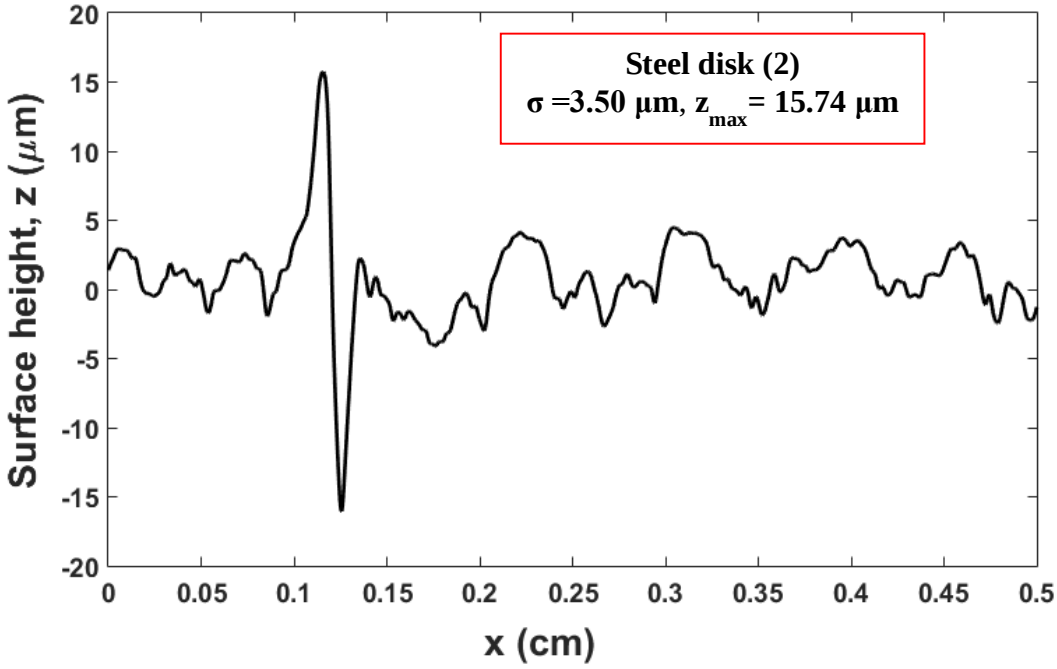
Steel disk (2)
σ =3.50 µm, z_max = 15.74 µm
Surface height, z (µm)
x (cm)
20
15
10
5
0
-5
-10
-15
-20
0
0.05
0.1
0.15
0.2
0.25
0.3
0.35
0.4
0.45
0.5

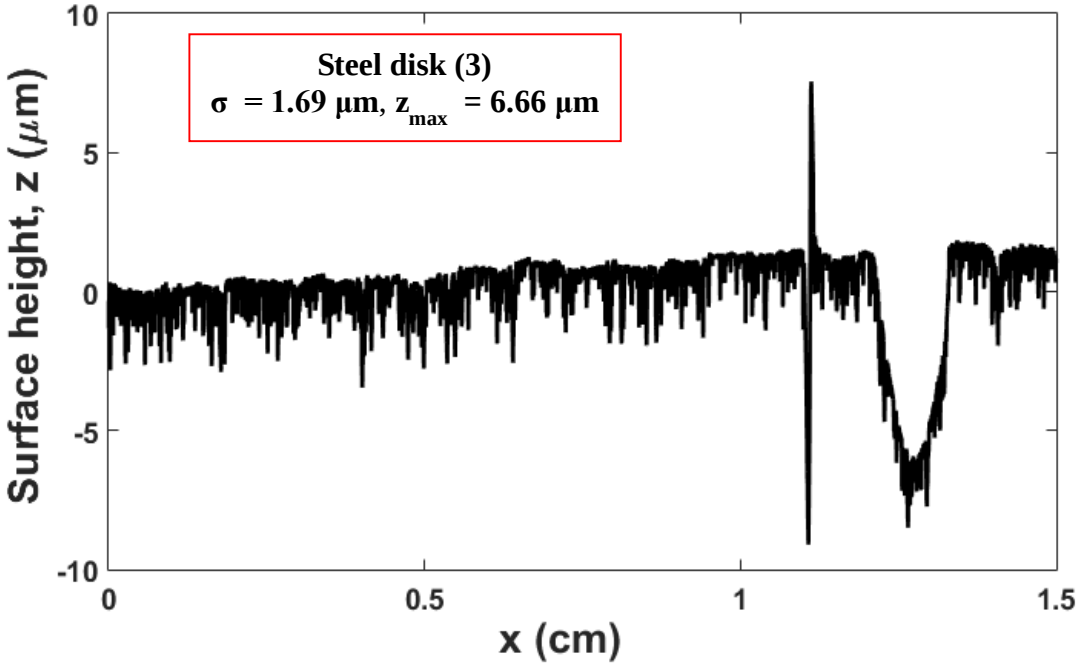
Steel disk (3)
σ = 1.69 µm, z_max = 6.66 µm
Surface height, z (µm)
x (cm)
10
5
0
-5
-10
0
0.5
1
1.5

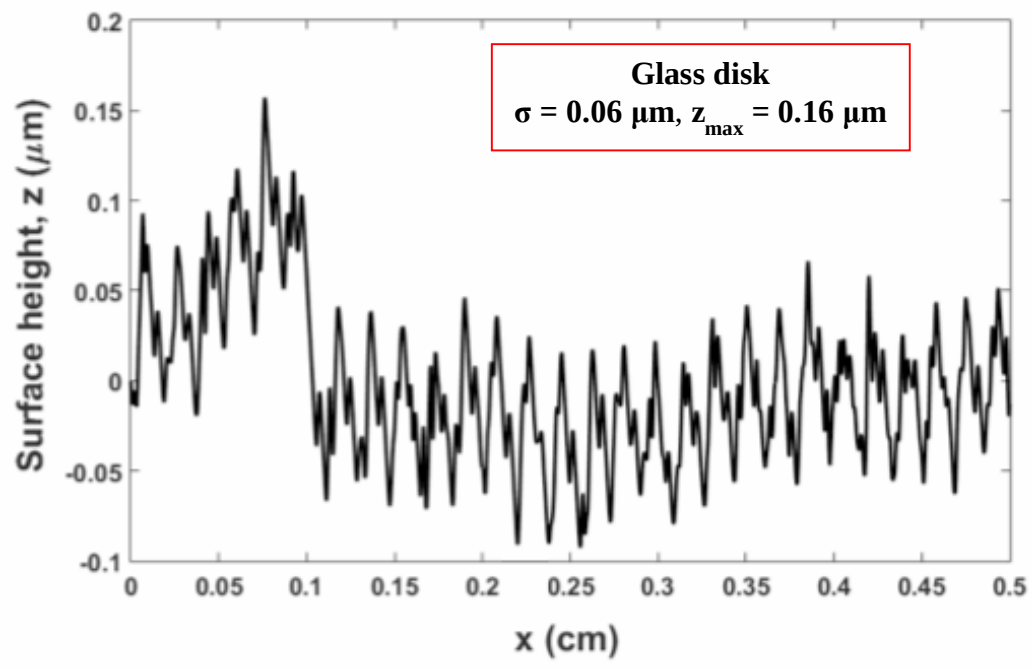

Fig. 2.42 Surface roughness for different contacting surfaces.

The results for the pull-off force, F_p, versus liquid volume, V_0, for the contact between the steel surface with maximum surface roughness of $z_{\max} = 24.19\mu m$ and fused silica glass are shown in Fig. 2.43. It can be seen that the pull-off force increases as the liquid volume between the two surfaces increases. The results for the pull-off force, F_p, versus the liquid volume, V_0, for the contact between the steel surfaces with maximum surface roughness of $z_{\max} = 15.74\mu m$ and $z_{\max} = 6.66\mu m$ and fused silica glass are shown in Figs. 2.44 and 2.45. It can be seen from Figs. 2.44 and 2.45 that as the roughness of contacting surfaces decreases, the pull-off force increases. Lower maximum surface roughness means smaller average gap between the contacting surfaces which leads to more negative capillary pressure inside the liquid film and higher pull-off forces.

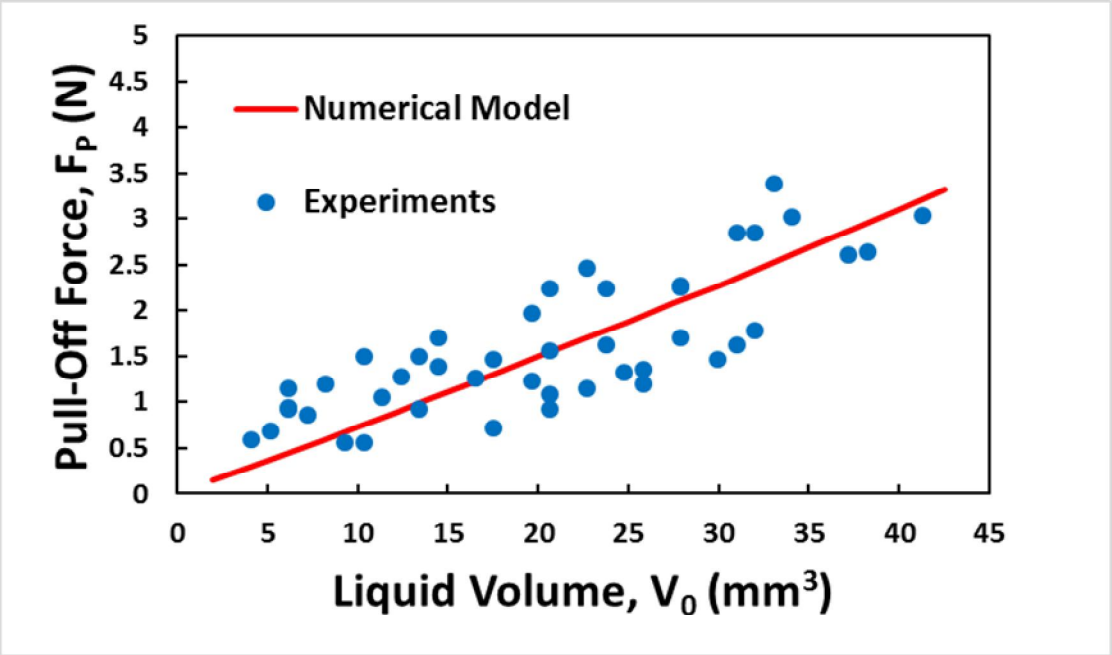

Fig. 2.43 The results for the pull-off force versus the liquid volume for $z_{\max} = 24.19\mu m$.

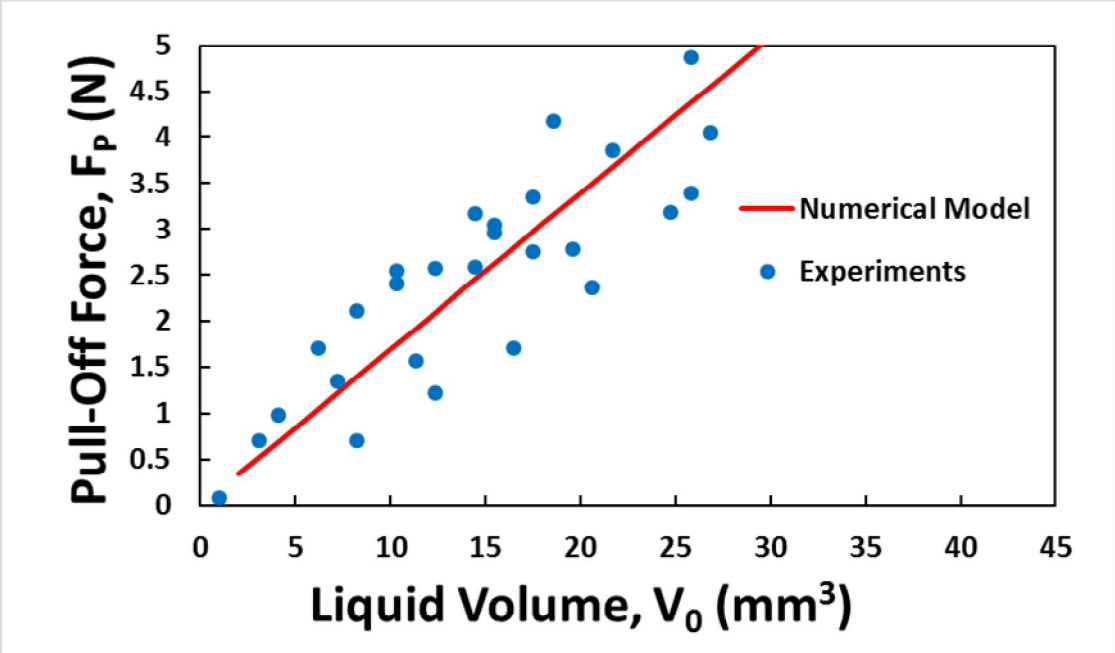

Fig. 2.44 The results for the pull-off force versus the liquid volume for $z_{\max} = 15.74\mu m$.

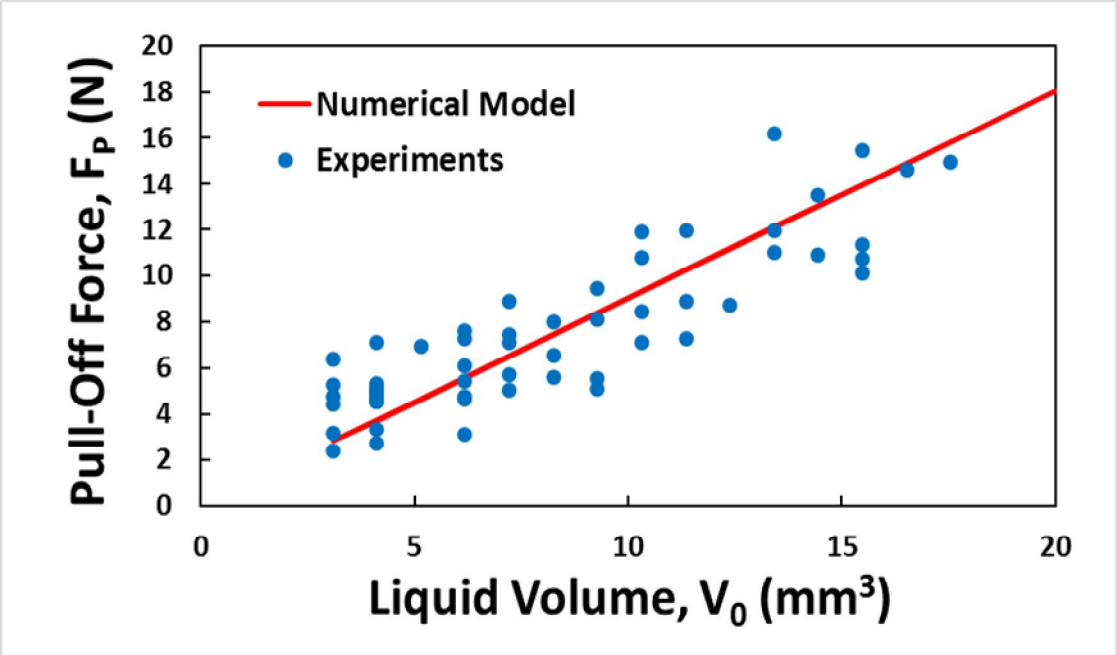

Fig. 2.45 The results for the pull-off force versus the liquid volume for $z_{\max} = 6.66 \mu m$.

The results for the pull-off force, F_p, between two plastic acrylic disks versus the liquid volume, V_0, are also obtained and is compared with the numerical approximation (See Fig. 2.46). The average spacing between the two surfaces are obtained by calculating the wetted area, A_w, between the two surfaces for different liquid volumes.

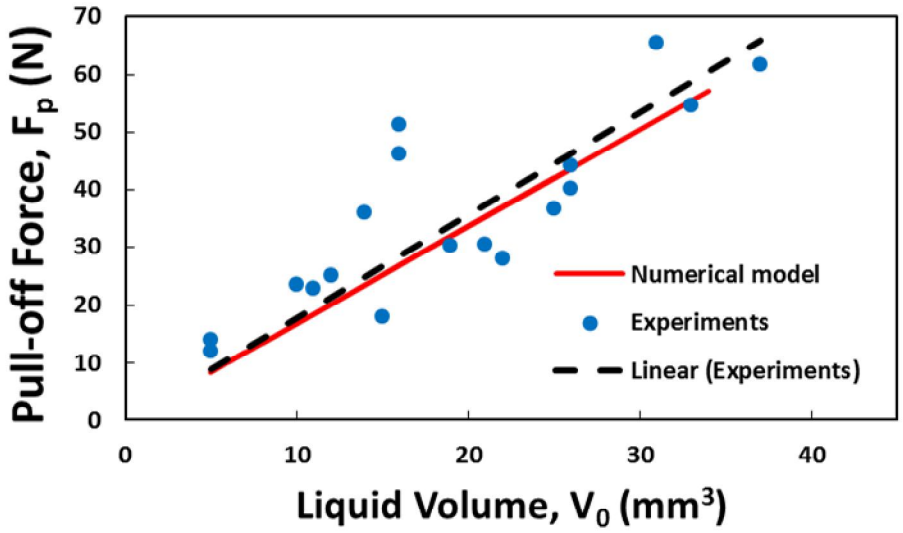

Fig. 2.46 The results for the pull-off force versus the liquid volume between two acrylic disks.

As it can be seen from Fig. 2.46 good agreement can be seen between the experimental results and the numerical model. Linear fit to the experimental results is shown to better see the difference between experimental results trend and the numerical model.

2.4.2 Friction force test

The friction force test between two contacting surfaces in the presence of the liquid film is performed by applying lateral force to the upper surface, while the position of the lower surface is fixed (Fig. 2.47). The friction force between the two surfaces at the point of slip is recorded. The test is performed for different values of liquid film volume, surface roughness and also under different external loading. This procedure will provide an estimate for the tensile force when its results are compared to the friction force test under dry conditions.

In this vein, one can consider the force equilibrium of the upper surface. Taking the external load, P_{ext}, as positive when brings the two surfaces into more contact, and the force exerted by the liquid, F_t, as positive when tensile, and the force exerted by the lower solid at the contact points (compressive force), F_c, as positive when compressive, we know

$$P_{ext} + F_t = F_c \tag{2.68}$$

The above equation expressed the fact that the force exerted on the upper sample by the liquid film, F_t, operates in conjunction with the external load, P_{ext}. These two force contributions must be balanced by the response force, F_c, of the solid-solid contact points. If it can be assumed that an intrinsic static friction coefficient, μ_s, may be assigned to the solid-solid contact points, then the horizontal applied force, F_f, required to initiate slip is then given by

$$F_f = \mu_s F_c \tag{2.69}$$

Substituting Eq. (2.69) in Eq. (2.68) and rearranging, the tensile force can be expressed as

$$F_t = F_c - P_{ext} = F_f / \mu_s - P_{ext} \tag{2.70}$$

The expression on the right-hand side of the above equation show that the tensile force can be obtained from a measurement of the horizontal force required to initiate slip for a given applied external load, assuming that the intrinsic solid-solid friction coefficient, μ_s, is known. This latter parameter can be obtained by performing a similar slip initiation measurement in the absence of the liquid film.

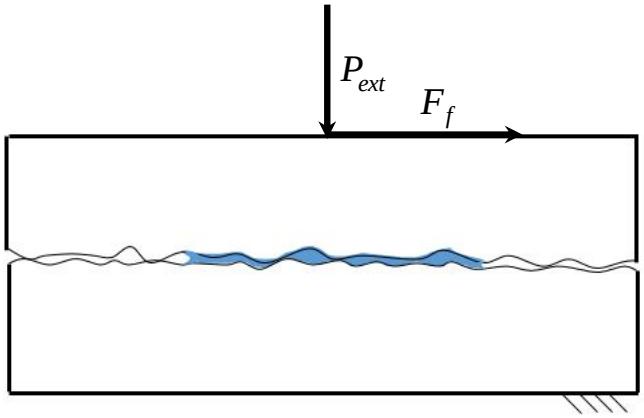

Fig. 2.47 The schematic of the friction force test.

2.4.2.1 Experimental setup

The experimental setup consists of a horizontal stand, mounting plate, force gauge, vertical positioner, L-shaped screw-in hook, spring, contacting surfaces, and liquid film. The experimental setup is shown in Fig. 2.48.

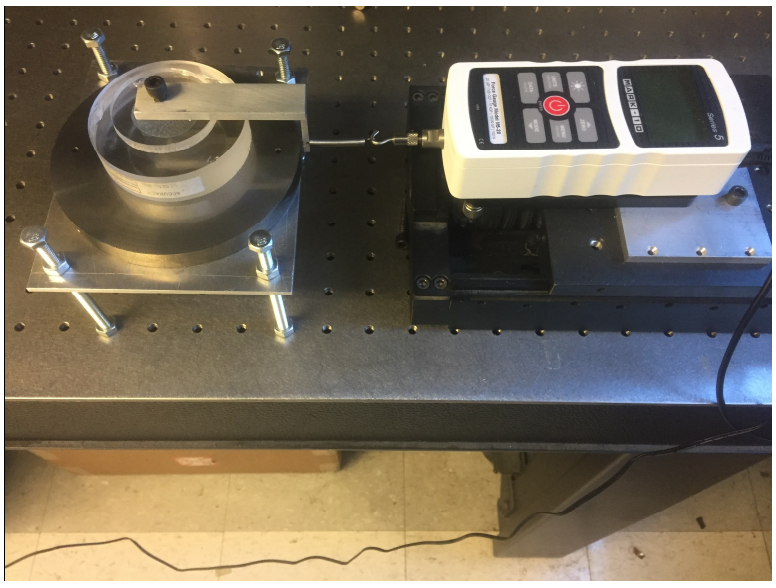

Fig. 2.48 Experimental setup to measure the friction force.

2.4.2.2 Results

Initially, the friction force test is performed under the dry contact condition i.e. in the absence of liquid film ($F_c = P_{ext}$). The friction force is applied by quasi-statically moving the top surface horizontally relative to the bottom surface. The bottom surface is fixed on the vertical positioner. The measurements are performed between the same steel disks and fused silica glass used in the pull-off force measurements. The friction force, F_f, results versus solid-solid contact force, F_c, under dry contact condition for the surface with maximum roughness of $z_{\max} = 6.66 \mu m$ is shown in Fig. 2.49. The static coefficient of friction can be obtained by calculating the slope of a linear fit to the results. The same friction test is performed for the surfaces with the roughness of $z_{\max} = 15.74 \mu m$ and $z_{\max} = 24.19 \mu m$, which are shown in Figs. 2.50 and 2.51.

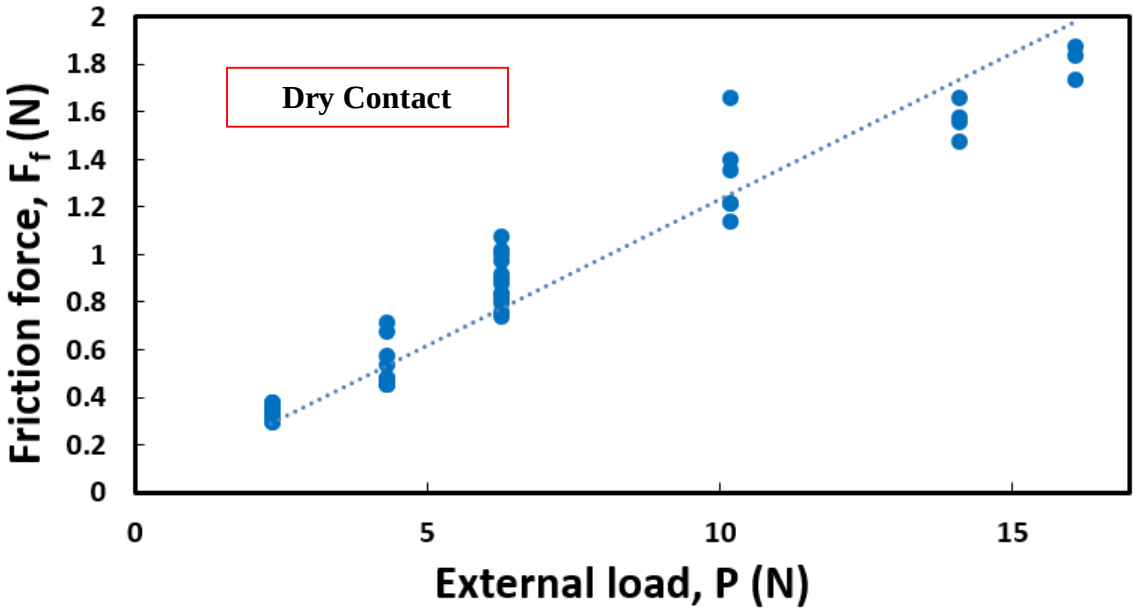

Fig. 2.49 The results for the friction force versus the external load for $z_{\max} = 6.66 \mu m$.

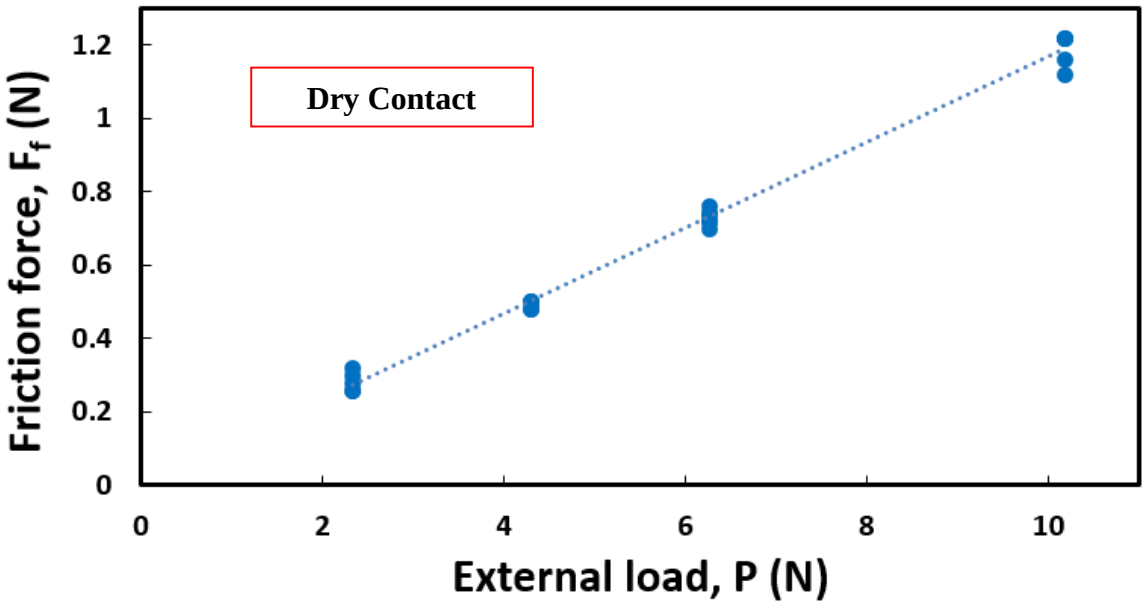

Fig. 2.50 The results for the friction force versus the external load for $z_{max} = 15.74 \mu m$.

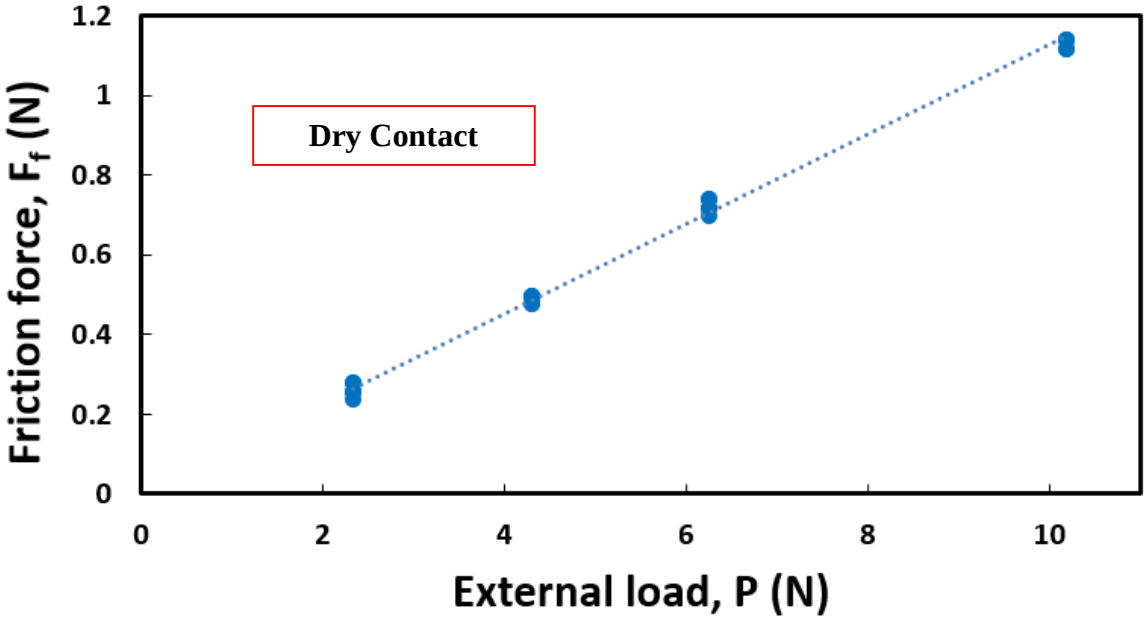

Fig. 2.51 The results for the friction force versus the external load for $z_{max} = 24.19 \mu m$.

The static coefficient of friction of $\mu_s = 0.1231, 0.1167,$ and 0.1127 are obtained for maximum surface roughness of $z_{max} = 6.66, 15.74,$ and $24.19 \mu m$, respectively, from

Figs. 2.49-2.51. It can be seen that the static coefficient of friction reduces with the maximum surface roughness.

The results for the tensile force, F_t, obtained knowing the static coefficient of friction, μ_s, and the friction force, F_f, in the presence of liquid film (see Eq. 2.3) are presented versus different liquid film volumes, V_0, for maximum surface roughness of $z_{\max} = 6.66 \mu m$ in Fig. 2.52. The external load, P_{ext}, acting on the contacting surfaces is the weight of the upper disk and the connections. The tensile force results for the maximum surface roughness of $z_{\max} = 15.74 \mu m$ and $z_{\max} = 24.19 \mu m$ are shown in Figs. 2.53 and 2.54.

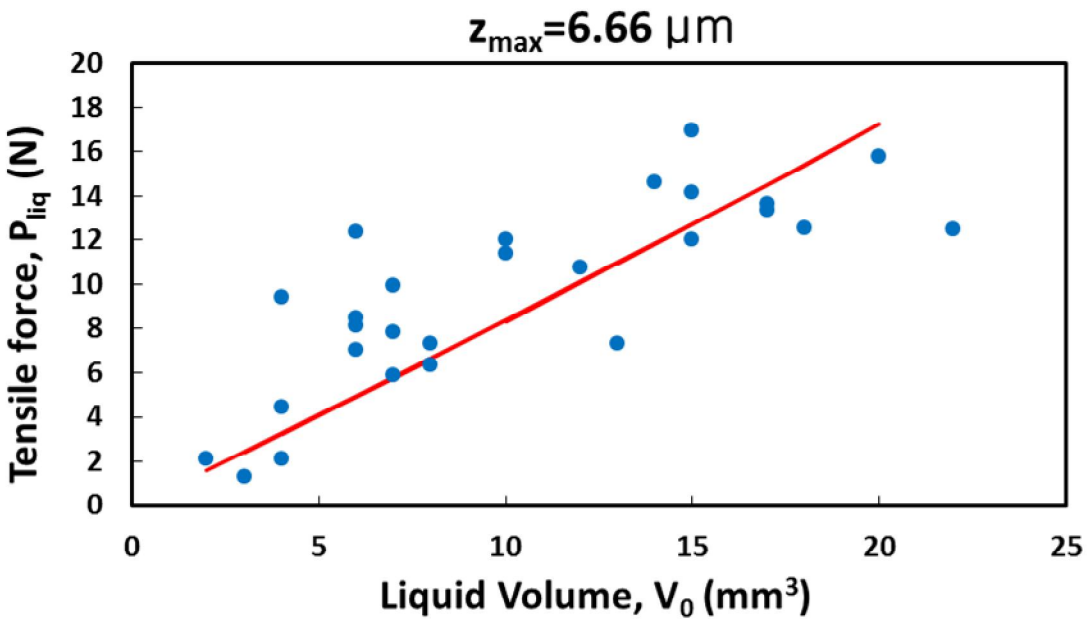

Fig. 2.52 The results for the tensile force versus the liquid film volume for surface roughness of $z_{\max} = 6.66 \mu m$.

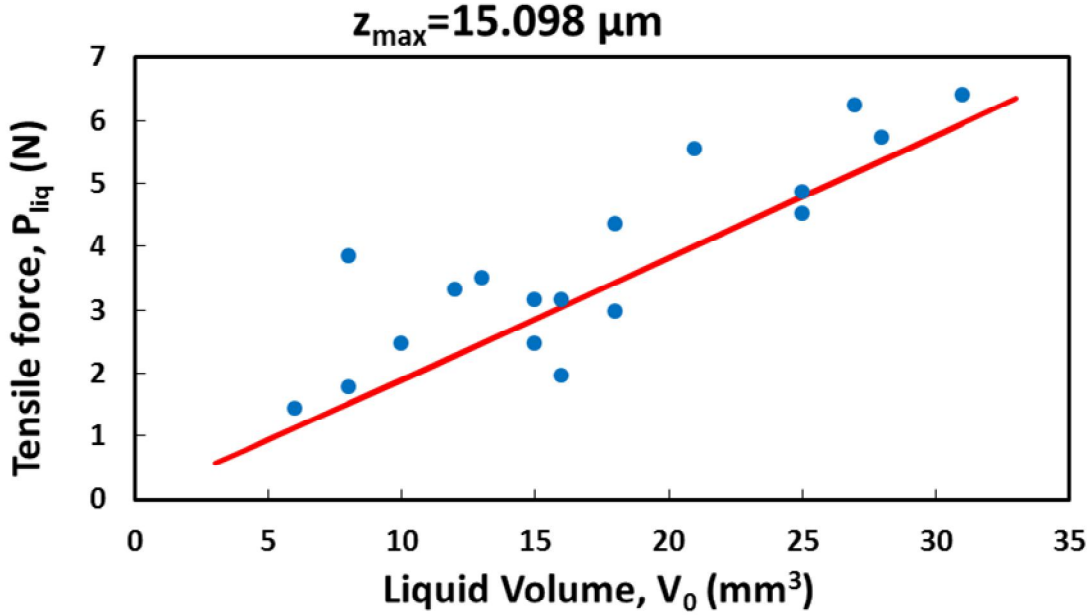

Fig. 2.53 The results for the tensile force versus the liquid film volume for surface roughness of $z_{max} = 15.74 \mu m$.

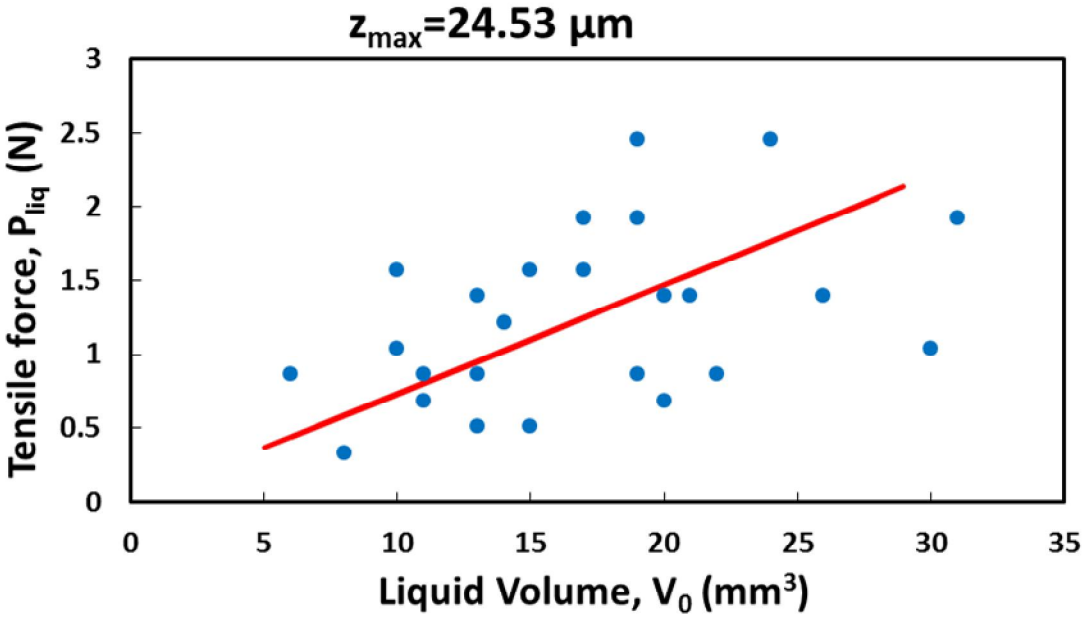

Fig. 2.54 The results for the tensile force versus the liquid film volume for surface roughness of $z_{max} = 24.19 \mu m$.

As it can be seen from Figs. 2.51-2.53, the tensile force increases as the liquid film volume between the two surfaces increases. Also, as the surface roughness increases, the tensile force between the two surfaces decreases.

The friction force test is also performed between thin transparency sheets and acrylic disks in order to achieve smaller average gap, $\bar{h}$, between the surfaces and also smaller effective elastic modulus, E'. The results for the dry friction force between the transparency sheet and the acrylic disk is shown in the Fig. 2.54.

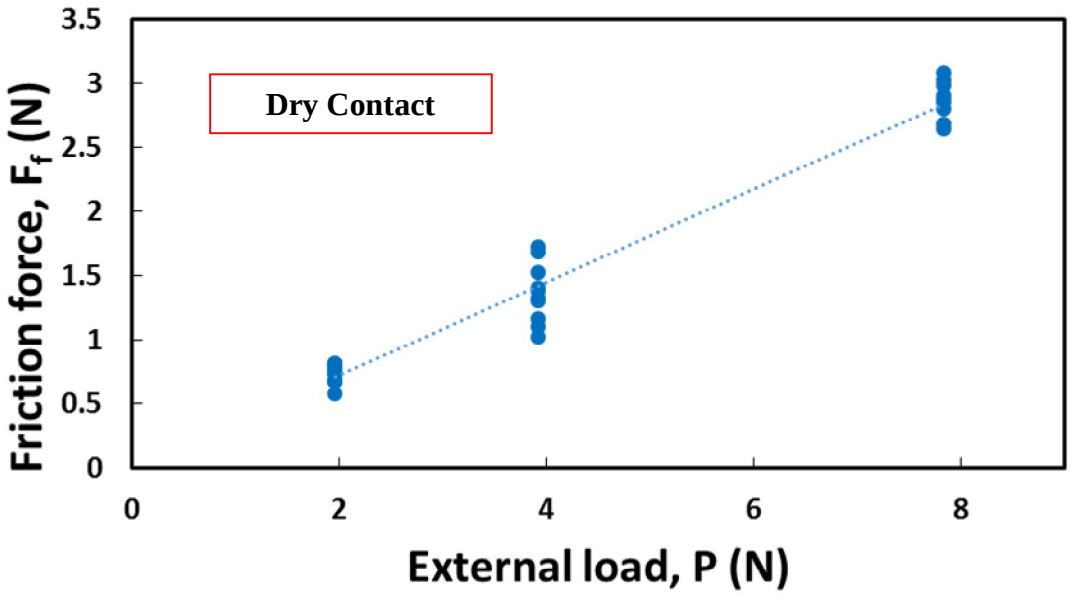

Fig. 2.55 The results for the friction force versus the external load for the contact of two acrylic disks.

The static coefficient of friction of 0.3622 can be calculated from the results of Fig. 2.55. This value agrees with the literature which suggests a range of coefficient of friction between 0.3 and 0.4 for the contact between plastic surfaces.

The results for the tensile force between the transparency sheet and the acrylic disk obtained from Eq. (2.70) are shown in Fig. 2.56. These results are compared to the

numerical approximation of the tensile force between contacting surfaces, $2\gamma V_0 / \bar{h}^2$. The average gap, $\bar{h}$, is calculated to be $5\ \mu m$ from the liquid film spread measurements between the two surfaces.

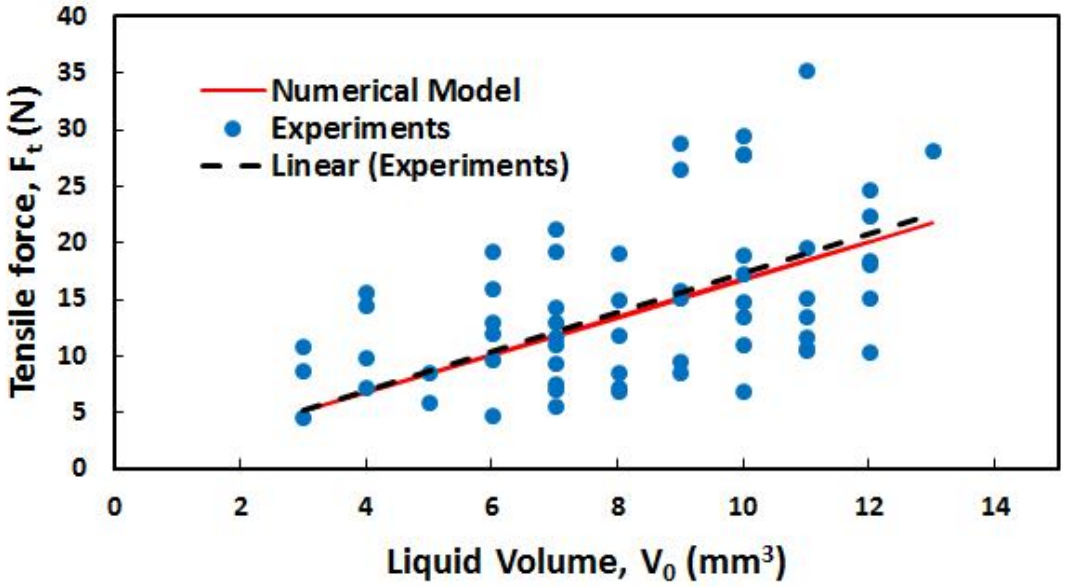

Fig. 2.56 The results for the tensile force versus the liquid film volume for the contact between transparency sheet and acrylic disks.

As it can be seen from Fig. 2.55, the experimental results are distributed around the numerical approximation, but, there is a good agreement between the linear fit (dashed black line) of the experimental results and the numerical approximation.

2.4.3 Wetted area Measurements

The spread of liquid film or wetted area, A_w, between two contacting surfaces is measured experimentally and is compared to the results of the developed numerical model. The results are obtained for different liquid film volume, V_0, and different maximum surface roughness, z_{max}.

2.4.3.1 Experimental setup

The experimental setup used in the current work is shown in Fig. 2.57. The setup consists of a digital camera, light source with adjustable control of light intensity, flexible light cords, contacting surfaces (the top surface should be transparent), and liquid film.

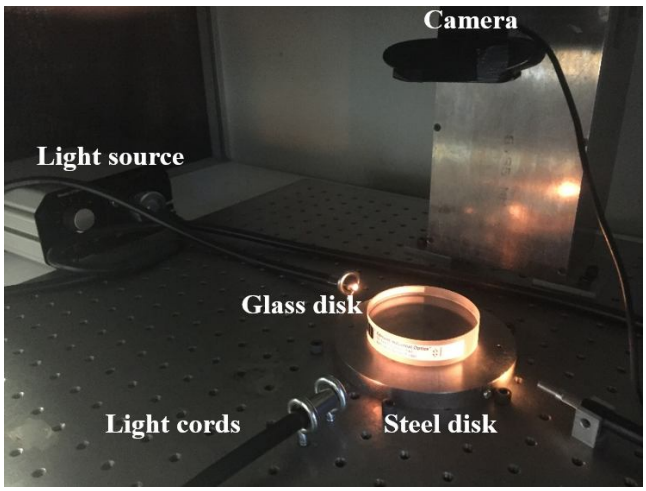

Fig. 2.57 The experimental setup used to measure the liquid film radius.

A known amount of liquid film is introduced between the two contacting surfaces. The light intensity of the light source along with the direction of the light cords are adjusted in order to differentiate between the wetted area and dry area. Due to the transparency of the top surface, the camera can capture images of the interface between surfaces. An image of the interface showing the wetted area for a known amount of intervening PSF oil is shown in Fig. 2.58. The red color is used to show the front line of the liquid film.

Fig. 2.58 Measured wetted area between two contacting surfaces.

Image processing is performed on the captured images to calculate the liquid film wetted area between the two surfaces. A threshold method, based on the light intensity at each pixel, is applied to detect the boundary of the wetted area. After finding the x and y coordinates of the various boundary points (pixels), the following mathematical relation is used to calculate the wetted area

$$A_w = \frac{1}{2}\left(\oint y_b dx_b - x_b dy_b\right) \tag{2.71}$$

where x_b, y_b are the coordinates of the boundary points. The discretized version of the Eq. (2.71) is given below

$$A_w = \frac{1}{2}\left(\sum_{i=1}^{N} y_i\left(x_{i+1} - x_i\right) - \sum_{i=1}^{N} x_i\left(y_{i+1} - y_i\right)\right) \tag{2.72}$$

where $i = 1$ to N is the index corresponding to the points on the boundary. It can be easily seen that $x_{N+1} = x_1, y_{N+1} = y_1$, so, Eq. (2.72) reduces to

$$A_w = \frac{1}{2}\left(\sum_{i=1}^{N}\left(y_i x_{i+1} - x_i y_{i+1}\right)\right) \tag{2.73}$$

2.4.3.2 Results

Results for the wetted area obtained from the experiments are compared with the results of the numerical model. For the simulations we set the liquid-solid contact angles to zero. We have made no attempt to precisely measure the contact angles. However, upon visual inspection it is clear that the contact angle is quite small so that the corresponding cosine values are very close to unity.

The results for the wetted area, A_w, between the steel surfaces and fused silica glass versus the liquid volume, V_0, for different values of maximum surface roughness, $z_{\max}$, are shown in Figs. 2.59-2.61. It can be seen as the liquid volume between the two surfaces increase, the wetted area also increases. The results also suggest as the maximum surface roughness increases, for a specific liquid film volume, the wetted area between the two surfaces decreases.

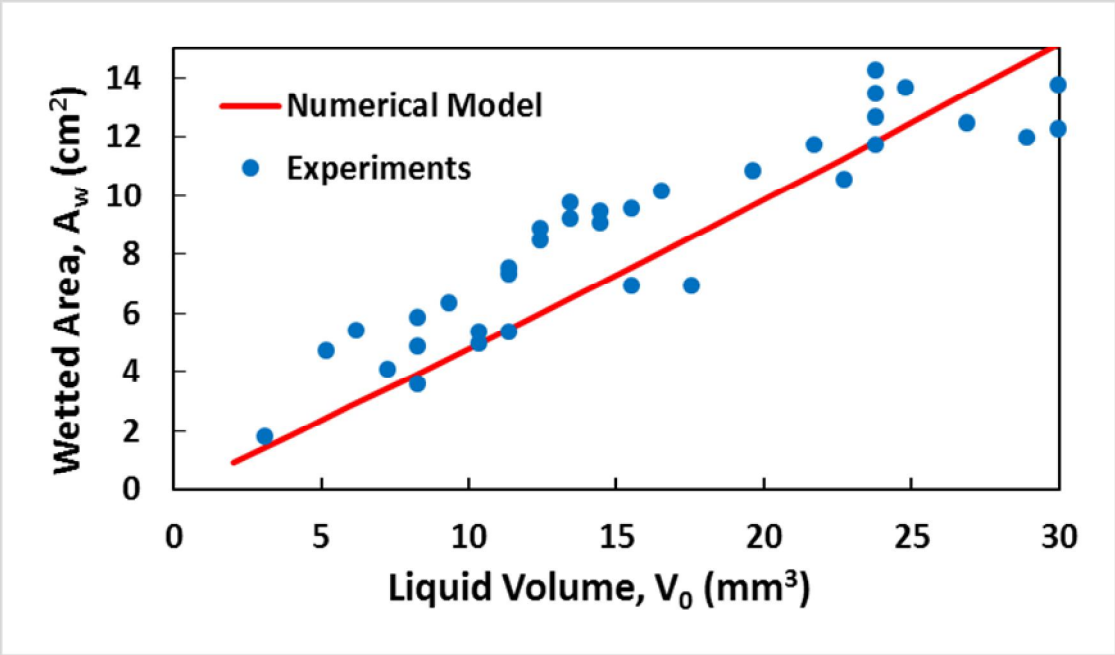

Fig. 2.59 The results for the wetted area versus the liquid volume for $z_{\max} = 24.19\mu m$.

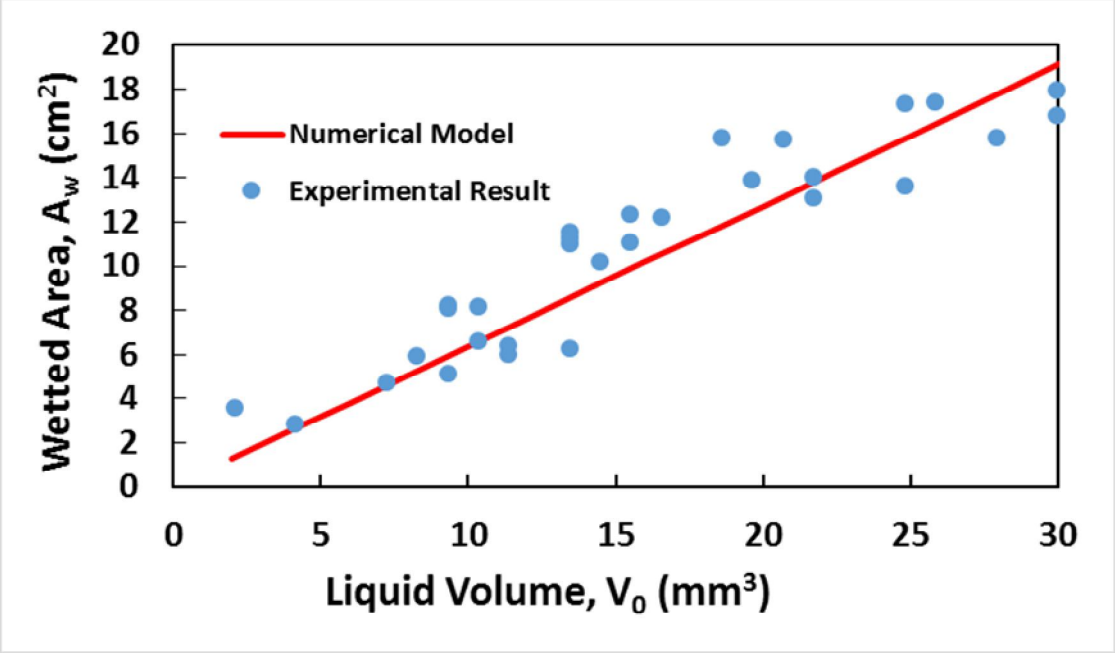

Fig. 2.60 The results for the wetted area versus the liquid volume for $z_{\max} = 15.74\mu m$.

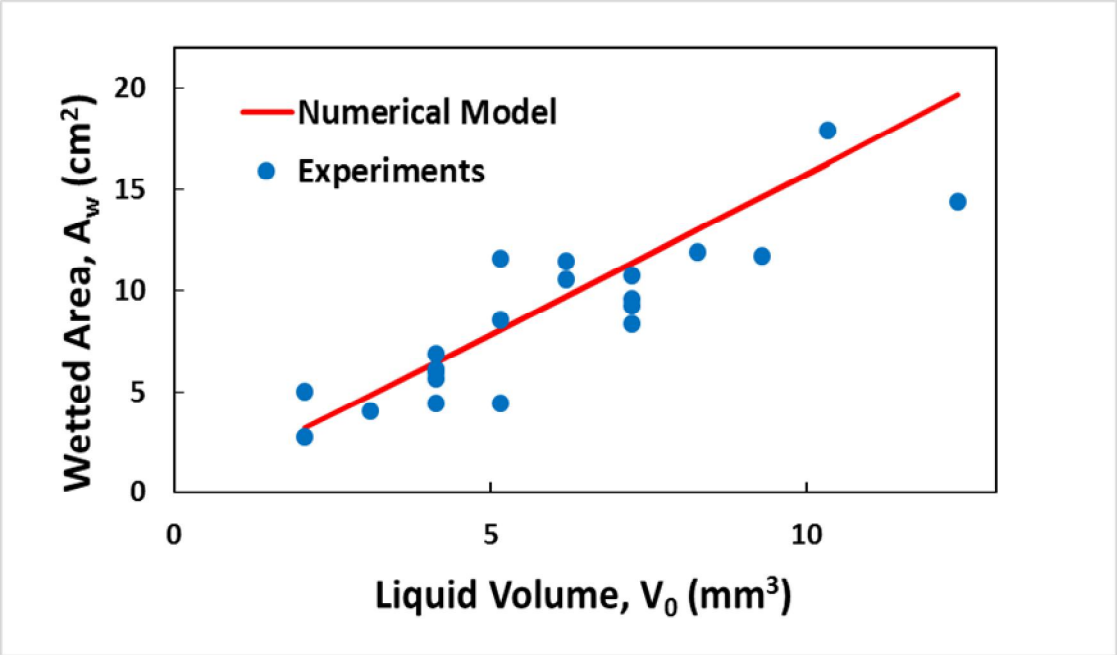

Fig. 2.61 The results for the pull-off force versus the liquid volume for $z_{max} = 6.66 \mu m$.

2.5 Conclusions

Liquid-mediated adhesion between contacting rough surfaces under static condition is studied both numerically and experimentally. Two different contact models i.e. spectral and deterministic are used to model the compressive stresses at the solid-solid contact spots which are solved simultaneously with the capillary equation for the tensile stresses developed at the wetted area. A numerical algorithm is designed to solve the interaction between tensile and compressive stresses simultaneously. The results for the tensile force, average gap, liquid film spread or wetted area, and contact area are obtained from both contact models and discussed. The normalization is performed to present the results in the most general way. It is shown that the normalized tensile force increases with the adhesion parameter until the interface reaches a point of instability. Beyond this point, no equilibrium configuration could be found because the compressive force in the contacting

surfaces is overwhelmed by the tensile force within the liquid film. This condition is called surface collapse, whereby there is an expected upward jump in the tensile force, wetted radius, and contact area as well as a downward jump in the average gap. An empirical relation for the adhesion parameter at the point of instability is obtained based on the material and geometrical properties of the contacting rough surfaces and the liquid film. It is shown that the critical adhesion parameter, Γ_{cr}, depends on the non-dimensional liquid volume, V_0^*, non-dimensional external load, P_{ext}^*, and the non-dimensional maximum height, $z_{\max}^*$ as in

$$\Gamma_{cr} = \frac{1}{\left(8.94V_0^* + 17.15\right) z_{\max}^{*\,-1.55V_0^{*0.11}} P^{*0.85}} + \frac{1}{0.011\, V_0^{*0.32} z_{\max}^{*\,2.87}}$$

, which is valid for the range of parameters given below the Eq. (2.54). The results for the critical adhesion parameter obtained from spectral and deterministic contact models showed good agreement.

The tensile force between two contacting surfaces in the presence of liquid film is obtained experimentally from pull-off and friction force tests. The results are obtained for different contacting rough surfaces and different volume of liquid film. The results show that the tensile force between surfaces increases with the liquid volume. Also, higher tensile forces are achieved for smoother surfaces. The tensile force calculated experimentally showed good agreement with the predictions of the numerical model.

The liquid film spread or the wetted area is also measured experimentally by recording images of the interface and performing image processing on the images. The wetted area increases with the liquid volume, and is higher between smoother surfaces. The experimental results showed good agreement with the results of the numerical model.

CHAPTER 3

LIQUID MEDIATED ADHESION: CAPILLARY FLOW CONDITION

In this section, the liquid-mediated adhesion between two contacting rough surfaces is considered where the liquid film flows between the two surfaces. The liquid flows due to the pressure gradient within the liquid film which is caused by capillary effects. A negative pressure distribution exists inside the liquid film compared to the ambient pressure which brings the two surfaces into closer proximity. Opposing these tensile stresses are the compressive stresses at the solid-solid contact spots.

The liquid flow within narrow spaces has studied extensively, such as found in capillary tubes and porous media. The classic model governing flow in capillaries is presented by Washburn [64]:

$$l(t) = \sqrt{t \frac{\gamma R \cos\theta}{2\eta}} \tag{3.1}$$

where l is the position of the free surface in the tube, t is time, γ is the liquid surface tension, R is the tube radius, θ is the liquid-solid contact angle and η is the liquid dynamic viscosity. The Washburn equation is based on a simple balance between (negative) capillary pressures and a velocity-dependent viscous drag that arises during laminar (Poiseiulle) flow in cylindrical tubes (see Fig. 3.1). The essential validity of the Washburn equation has been supported experimentally [65-67], and via molecular dynamics (MD) calculations [68]. In this study we are interested in how liquids flow within the confined region defined by the interface between contacting (rough) surfaces.

Such a region has similarities to that of a capillary tube, but is more complex: there are random variations in the local gap, and depending on the rigidity of the surface, there is the potential for elastic deformation to strongly couple with the liquid flow. Nevertheless, the Washburn equation will provide the frame of reference with which to develop to interpret the experimental and numerical results. That is, it is possible to conceive of an effective capillary radius for a rough-surface interface, similar to what has been done in the analysis of the wetting of soils [69] and drainage through rocks [70]. Expanding the point a bit further, it will be of interest to compare the perspective of the Washburn theory to what is obtained from a numerical simulation of the flow through the interface defined by the contacting surfaces.

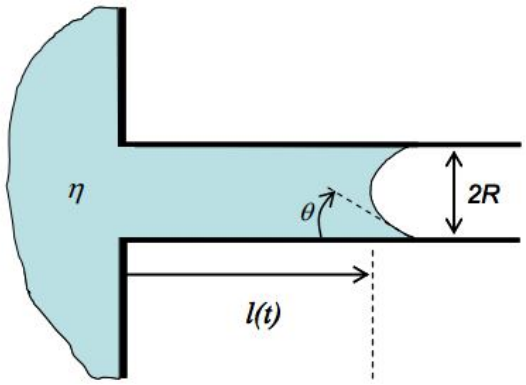

Fig. 3.1 Flow in a horizontal capillary tube.

3.1 Methodology

A schematic view of the interface of interest is shown in Fig. 3.2: A volume of liquid is introduced via a central hole having radius R_1 of an annular rigid flat. The wetting liquid spreads between the annular rigid flat in contact with a rough plate until the liquid film radius, b, reaches the outer radius of the rigid flat, R_2. The capillary

effect is the driving force for the liquid flow, which depends on the affinity of the liquid with the contacting solid surfaces, or how well it “wets” them. Capillary effects will first draw the liquid into the channel and then into the interface between the surfaces. Owing to small spacing between the surfaces, the liquid film has a free surface with large values of curvature (i.e. small values of radius of curvature). These large curvatures are associated with large pressure drops across the free surface of the liquid film [53]. For a liquid film that wets the two contacting surfaces, the free surface is concave from the perspective of the liquid film, leading to film pressures that are significantly less than that of the ambient. Assigning a reference value of zero to the ambient, the associated negative film pressures represent positive tensile stresses that tend to pull the two solid surfaces together. Moreover, the decreasing proximity of the surfaces can lead to increases in solid-solid contact. It should be noted that a combination of a rigid flat surface and a rough surface used in this work is a model of two hypothetical elastic rough surfaces, whereby the rough surface of the model is given the combined roughness and flexibility of the hypothetical surface pair.

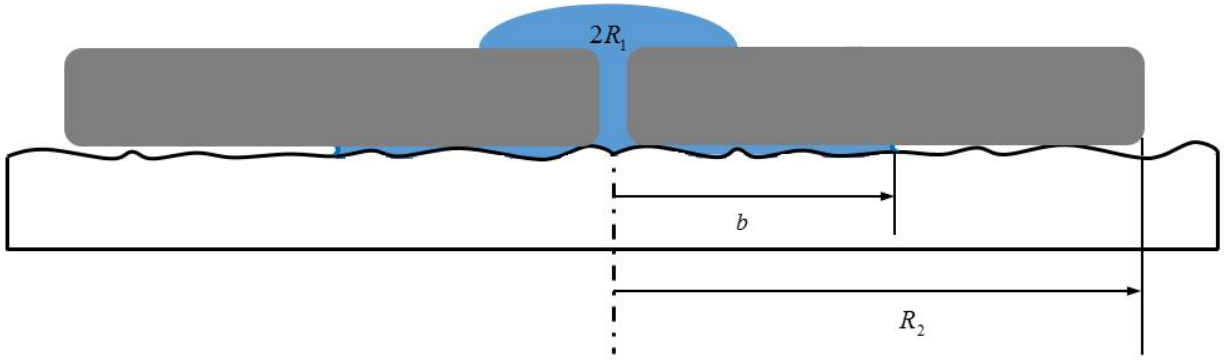

Fig. 3.2 Schematic depiction of the modeled interface.

The modeling approach should solve equations of lubrication, capillarity and linear elasticity simultaneously to simulate the capillary flow between contacting rough surfaces. A numerical model comprised of a macro-contact model, a mixed lubrication model, and a micro-contact model is developed to solve this problem. The macro-contact model is used to determine the pressure distribution within the nominal region of contact due to external load acting on the contacting surfaces. In the macro-contact model, the effect of surface roughness is neglected, so that the contacting surfaces are assumed to be nominally smooth. The pressure distribution within the liquid film is obtained from a mixed lubrication model. The deformation of the surface topography and the resulting film thickness are determined in the micro-contact model using a volume loss approach [56]. An iterative numerical algorithm is implemented to solve these sub-models simultaneously to obtain results for the tensile force, liquid film thickness, and liquid flow rate between the two contacting surfaces.

3.1.1 Macro-Contact Model

The macro-contact model is used to determine the pressure distribution between the annular rigid flat and the flexible disk due to external loading, P_{ext}. The macro-contact model considers only the gross dimensions of the annular interface, which is depicted in Fig. 3.3. Thus, within this sub model, any effect of surface roughness is neglected. A numerical approach based on influence coefficients is used in the current work to obtain the pressure distribution under the rigid flat.

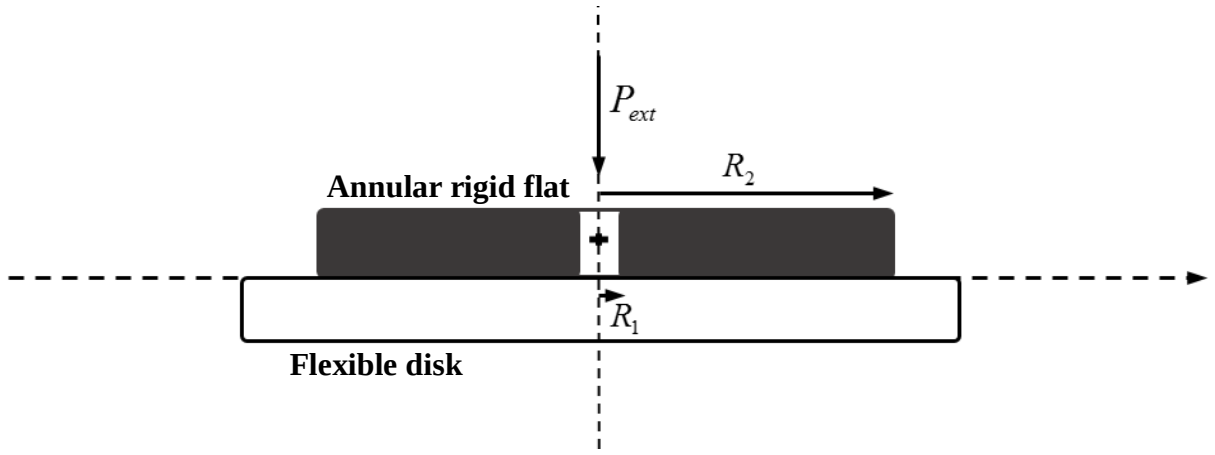

Fig. 3.3 Contact between an annular rigid flat and a flexible disk.

To obtain the influence coefficients, a solution for the case of constant pressure acting over a thin annulus is needed. To get this result, we make use of the solution for a uniform pressure acting over a circular region: The deformation, u, of a homogeneous, isotropic, elastic half-space with elastic modulus E and Poisson's ratio ν under a uniform pressure of p acting within a circular region of radius a is given by (e.g., [60])

$$u(r)=\begin{cases}\dfrac{4(1-\nu^2)}{\pi E}\,paE_c(r/a), & r\le a\\[2ex] \dfrac{4(1-\nu^2)}{\pi E}\,pr\left[E_c(a/r)-(1-a^2/r^2)K_c(a/r)\right] & r>a\end{cases} \tag{3.1}$$

where K_c, E_c are the complete elliptic integrals of the first and second kind, respectively. For the axisymmetric contact problem of Fig. 3.3, the region is divided into small annular elements, each having width Δr, as shown in Fig. 3.4. The position of each element is specified by the radial position of the center of the element. The surface deformation and the pressure distribution are represented by adjacent columns of uniform

deformation or pressure. For example, for the i[th] annular element, the radial position is r_i, the surface deflection is u_i, and the pressure is p_i.

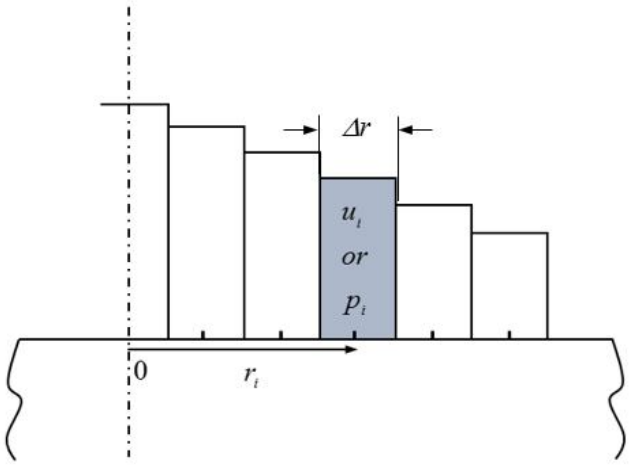

Fig. 3.4 Discrete pressure and deformation elements.

Thus, the influence coefficient C_{ij} is defined as the deflection at r_i due to a unit pressure applied at r_j. The influence coefficients, C_{ij}, can be computed as described below. Suppose we wish to find the normal deflection at some radial position r_i caused by a thin circular ring of constant pressure applied at r_j. By superposition we can view the pressurized ring as a combination of a uniform positive pressure acting within a circle of radius $r_j + \Delta r/2$ with a uniform negative pressure with the same magnitude acting within a circle of radius $r_j - \Delta r/2$ (Fig. 3.5). Then the influence coefficients can be written as

$$C_{ij}=\frac{u(r_i)}{p(r_j)}=\begin{cases}\dfrac{4r_j}{\pi E}\left[(1+\dfrac{\Delta r}{2r_j})E_c(\dfrac{r_i}{r_j+\Delta r/2})-(1-\dfrac{\Delta r}{2r_j})E_c(\dfrac{r_i}{r_j-\Delta r/2})\right], & r_i\le r_j \\ \dfrac{4r_j}{\pi E}\left[(1+\dfrac{\Delta r}{2r_j})E_c(\dfrac{r_i}{r_j+\Delta r/2})-\dfrac{r_i}{r_j}E_c(\dfrac{r_j-\Delta r/2}{r_i})+\dfrac{r_i}{r_j}(1-\dfrac{(r_j-\Delta r/2)^2}{r_i^2})K_c(\dfrac{r_j-\Delta r/2}{r_i})\right], & r_j-\Delta r/2<r_i\le r_j+\Delta r/2 \\ \dfrac{4r_j}{\pi E}\left[\dfrac{r_i}{r_j}E_c(\dfrac{r_j+\Delta r/2}{r_i})-\dfrac{r_i}{r_j}E_c(\dfrac{r_j-\Delta r/2}{r_i})+\dfrac{r_i}{r_j}(1-\dfrac{(r_j-\Delta r/2)^2}{r_i^2})K_c(\dfrac{r_j-\Delta r/2}{r_i})-\dfrac{r_i}{r_j}(1-\dfrac{(r_j+\Delta r/2)^2}{r_i^2})K_c(\dfrac{r_j+\Delta r/2}{r_i})\right], & r_i>r_j+\Delta r/2\end{cases}$$

(3.2)

This equation can be applied to the contact between two elastic surfaces by defining a composite elastic modulus, E^*. For our purposes, the deformation, u, represents the sum of the deformations of two surfaces, and p represents the contact pressure at the interface.

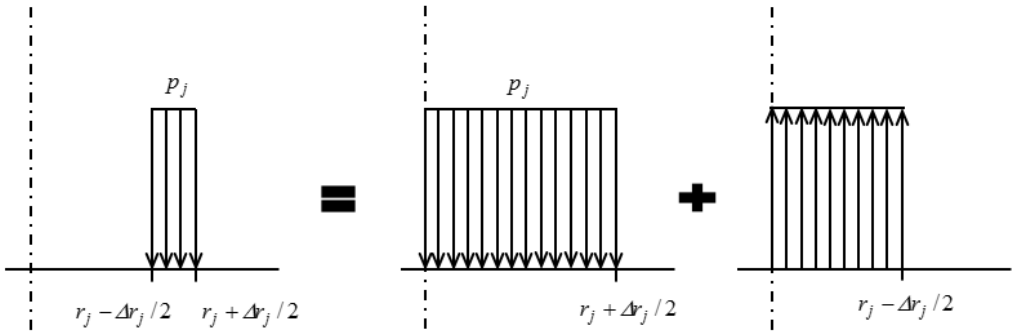

Fig. 3.5 Equivalency of a pressurized ring to the superposition of a uniform positive pressure circle of radius $r_j+\Delta r_j/2$ with a uniform negative pressure circle of radius $r_j-\Delta r_j/2$.

In the current work, smooth edges are assumed for the contacting surfaces as suggested by Fig. 3.3, in order to avoid unbounded pressures at the inner and outer radii of the contact. Moreover, in real applications, every disk has a nonzero value of edge radius. In the current work an edge radius of 0.1 mm is used in the calculations. Fig. 3.6 depicts the

pressure distribution corresponding to a composite elastic modulus, E^*, of 50 GPa, an inner radius, R_1, equal to 0.1 cm, an outer radius, R_2, equal to 2 cm, and an external load, P_{ext}, equal to 20 N. As observed the pressure distribution reaches high values at the inner and outer radii due to edge effects.

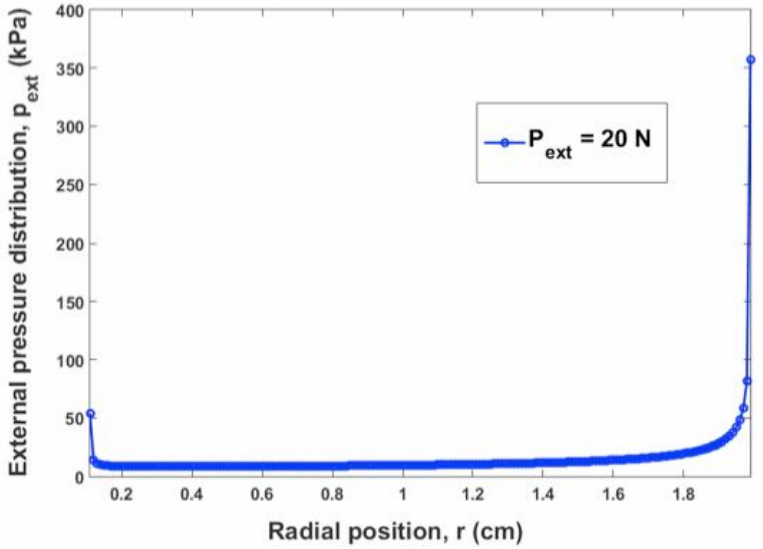

Fig. 3.6 Results for the pressure distribution for an external load of $P_{ext} = 20N$.

3.1.2 Mixed Lubrication Model

A mixed lubrication model is used to determine the pressure distribution within the liquid film. Assuming incompressible, axisymmetric flow with isotropic surface roughness, the average Reynolds equation [71] is given by

$$\frac{\partial}{\partial r}\left(\varphi r h^3 \frac{\partial p_f}{\partial r}\right) = 12\eta r \frac{\partial h}{\partial t} \tag{3.3}$$

where r is the radial coordinate, p_f is the liquid film pressure, h is the film thickness, φ is the pressure flow factor, and η is the dynamic viscosity of the liquid film. It is

assumed that the squeeze film effects are negligible, which means that the rate of change of film thickness in any radial position is sufficiently small in Eq. (3.3) to have an insignificant impact on the liquid film pressure. Thus, Eq. (3.3) simplifies to the form

$$\frac{d}{dr}\left(\varphi r h^3(r)\frac{dp_f}{dr}\right)=0 \tag{3.4}$$

Patir and Chang [72] developed a model for pressure induced flow between nominally smooth surfaces. The transverse pressure flow factor, φ, for isotropic rough surfaces is given by

$$\varphi = 1-0.9e^{-0.56h/\sigma} \tag{3.5}$$

where σ is the composite r.m.s. roughness of contacting surfaces. The boundary conditions for Eq. (3.4) includes ambient pressure at the inner radius of the annular region and the capillary pressure at the flow radius, b, which is given by $p_f(b)=-\gamma(\cos\theta_A+\cos\theta_B)/h_b$ [53], where h_b is the film thickness at the location of the free surface(where $r=b$). In order to solve for the liquid film pressure distribution, the domain is discretized into annular segments with width Δr. Each annular segment located at radial position, r_j, has the uniform pressure, p_{fj}, and film thickness, h_j as illustrated in Fig. 3.7. The discretized form of Eq. (3.4) is given by

$$p_{f\,j}=\frac{\left(\varphi_j+\frac{3\varphi_j r_j}{h_j}\frac{h_{j+1}-h_j}{\Delta r}+r_j\frac{\varphi_{j+1}}{\Delta r}\right)p_{f\,j+1}+\frac{\varphi_j r_j}{\Delta r}p_{f\,j-1}}{\varphi_j+\frac{3\varphi_j r_j}{h_j}\frac{h_{j+1}-h_j}{\Delta r}+r_j\frac{\varphi_{j+1}}{\Delta r}+\frac{\varphi_j r_j}{\Delta r}} \tag{3.6}$$

where $\varphi_j = 1 - 0.9e^{-0.56(h_j/\sigma)}$. Equation (3.6) is solved iteratively using the familiar Gauss-Seidel method (e.g., [51]).

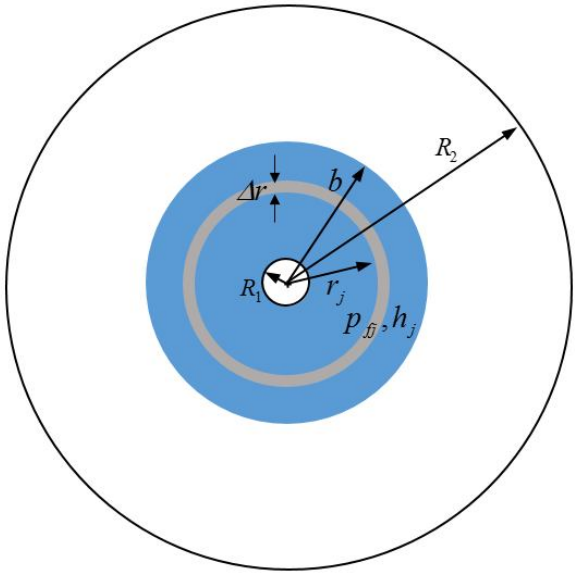

Fig. 3.7 The schematic explanation of the parameters involved in the Eq. (3.6).

3.1.3 Micro-Contact Model

The pressure distribution due to external loading from the macro-contact model and liquid film pressure distribution from the mixed lubrication model cause micro-scale surface deformation. In the current work, the Jackson-Streator (JS) multiscale contact model is used to determine the surface deformation within a circumferential band of width Δr at each radial location in the annular contact zone. The JS contact model is based on representing the rough surface in multiple scales of roughness based upon the fast Fourier transform (FFT) of the surface heights.

For the parametric analysis, rough surface data is generated using a method outlined by Garcia and Stoll [59]. One of the rough surfaces generated using this method is shown in

Fig. 3.8. A two dimensional FFT is then performed on the generated surfaces using the following equation

$$F(k_x, k_y) = \frac{1}{N_x N_y} \sum_{n_x=0}^{N_x-1} \sum_{n_y=0}^{N_y-1} z(n_x, n_y) e^{-i2\pi(k_x n_x / L_x + k_y n_y / L_y)} \tag{3.7}$$

where z is the surface heights, N_x and N_y are the number of nodes in x and y directions, k_x and k_y correspond to the spatial frequency levels in x and y directions, while n_x and n_y correspond to the spatial coordinates in x and y directions. The output is a $N_x \times N_y$ matrix comprising of complex elements. As the micro-contact model requires a single amplitude for each frequency level, an equivalent 1D amplitude at frequency level k is defined which is given by $\Delta_k = \left[\sqrt{\sum_{k_y=0}^{N_y-1} \left| F(k, k_y) \right|^2} + \sqrt{\sum_{k_x=0}^{N_x-1} \left| F(k_x, k) \right|^2} \right]$, based on taking the r.m.s. values of 1D transforms in x and y directions and then averaging the two values [56].

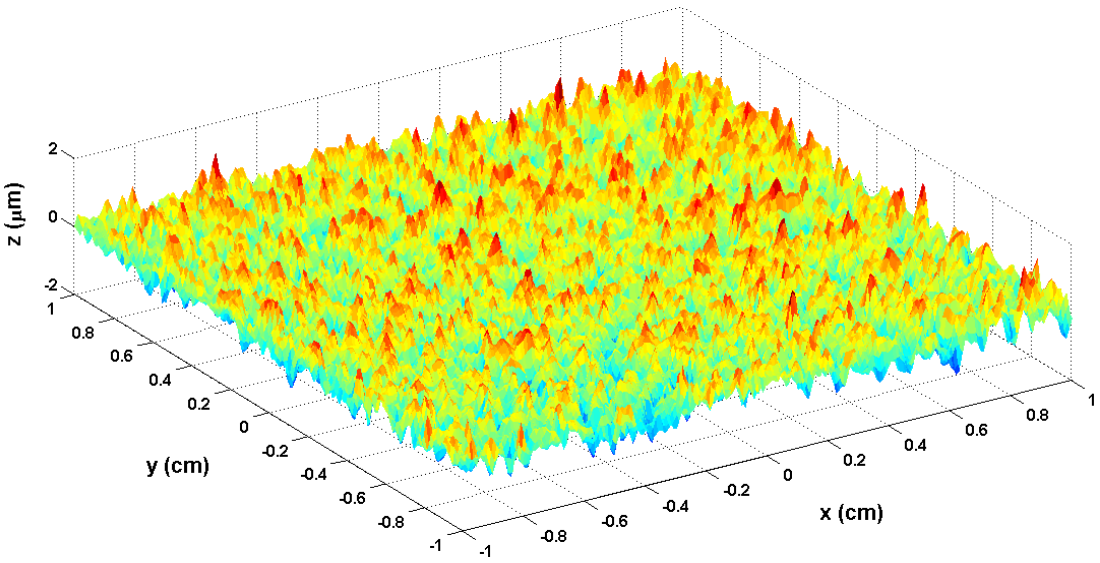

Fig. 3.8 A 3D plot of a generated Gaussian isotropic rough surface.

At each frequency level k, the asperities are modeled as three-dimensional sinusoidal shape geometries of wavelength λ_k and amplitude Δ_k. Johnson, Greenwood, and Higginson (JGH) [54] developed two analytical asymptotic solutions for early and nearly complete contact of sinusoidal asperities. Later, Jackson and Streator [55] presented an empirical equation connecting the two asymptotic solutions based on the numerical results of JGH [54]. At each frequency level, k, the average pressure acting on the surfaces is denoted by $\overline{p}_k$, and p_k^* is defined as the average pressure that causes complete contact between the two sinusoidal asperities as explained in the previous sections. Since each frequency level carries the same load, the average pressure, $\overline{p}_k$ is given by $\overline{p}_k = \dfrac{p_{comp}(r_j) 2\pi r_j \Delta r}{A_{k-1}}$.

That is, the nominal contact area is divided into many annular bands with width, Δr, and the load supported by each band is the product of the band area and the compressive stress $p_{comp}(r_j)2\pi r_j \Delta r$. The JS [52] empirical relations are used to calculate the contact area, $\overline{A}_k$ at each scale k and the relations developed by Rostami and Jackson [55] are used to calculate the average spacing, $\overline{g}_k$, at each frequency scale k.

3.1.4 Film thickness

In order to complete the model for the capillary flow between contacting surfaces, the film thickness between the contacting surfaces at each radial position is needed. The volume-loss approach developed by Green et al. [56] is used to calculate the gap at each radial position. This approach considers the reduction in the available interfacial volume caused by asperity deformation due to both compressive and tensile stresses within annular band of width Δr. The volume loss due to compressive stresses at each radial position, $(\Delta V_{loss-comp})_{r_j}$, can be obtained by summing up the volume loss reduction at each frequency level, k, which can be obtained from the JS contact model by

$$(\Delta V_{loss-comp})_{r_j} = \sum_{k=1}^{N^*} (\Delta V_{loss})_k \tag{3.8}$$

where N^* is the Nyquist limit. The volume loss due to tensile stress within the annular segment located at location r_j with thickness Δr can be calculated by

$$(\Delta V_{loss-tens})_{r_j} = -\int_{r_j-\Delta r_j/2}^{r_j+\Delta r_j/2} u_t(\zeta) 2\pi\zeta d\zeta \tag{3.9}$$

where u_t is the deformation within the annular region with width Δr at location r_j due to uniform fluid pressure $\left(p_f\right)_j$, ζ is the dummy integral variable, and $\left(\Delta V_{loss-tens}\right)_{r_j}$ is the volume loss due to tensile stresses at location r_j. The expression for deformation, u_t, within the annular element, Δr, due to uniform pressure $\left(p_f\right)_j$ is given by

$$u_t(\zeta)=\frac{4}{\pi E'}\left(p_f\right)_j\left(r_j+\Delta r_j/2\right)E_c\left(\frac{\zeta}{r_j+\Delta r_j/2}\right)-\frac{4}{\pi E'}\left(p_f\right)_j\zeta\left\{E_c\left(\frac{r_j-\Delta r_j/2}{\zeta}\right)-\left(1-\left(\frac{r_j-\Delta r_j/2}{\zeta}\right)^2K_c\left(\frac{r_j-\Delta r_j/2}{\zeta}\right)\right)\right\} \tag{3.10}$$

Next, the film thickness or gap, $h\left(r_j\right)$, assigned within radial spacing, Δr, at radial position r_j can be calculated by

$$h\left(r_j\right)=z_{\max}-\frac{\left(\Delta V_{loss-comp}\right)_{r_j}+\left(\Delta V_{loss-tens}\right)_{r_j}}{2\pi r_j\Delta r} \tag{3.11}$$

where $z_{\max}$ is the average gap corresponding to initial contact in the absence surface deformation.

3.1.5 Liquid flow rate

Upon solving the equation of mixed lubrication for the pressure field (see Section 3.1.2), one can compute the velocity profile at the location of the free surface of the film. Equating the rate of change of liquid film radius with the average of radial velocity across the film thickness, we obtain

$$\frac{db}{dt}=\bar{v}_r=\frac{1}{h_b}\int_0^{h_b}\frac{\varphi_{h_b}}{2\eta}\left(\frac{dp_f}{dr}\right)_{r=b}\left(z'^2-h_bz'\right)dz'=\frac{-\varphi_{h_b}h_b^2}{12\eta}\left(\frac{dp_f}{dr}\right)_{r=b} \tag{3.12}$$

The discretized version of Eq. (3.12) is given as

$$b^{t+1} = b^t - \frac{\varphi_{h_b} \Delta t}{12 \Delta r} \frac{h_b^2}{\eta} \left(p_{f\,j}{}^t - p_{f\,j-1}{}^t \right)_b \tag{3.13}$$

At each value of b, the rough surface is assumed to be in mechanical equilibrium with the liquid film, even though the liquid film is not at steady state. Thus, the liquid flow rate, Q, at each time, t, can be computed from

$$Q^t = -2\pi b^t \frac{\varphi_{h_b} h_b^3}{12\eta} \frac{\left(p_{f\,j}{}^t - p_{f\,j-1}{}^t \right)_b}{\Delta r} \tag{3.14}$$

3.1.6 Numerical algorithm

The flowchart of the numerical algorithm is shown in Fig. 3.9. After introducing the material properties of the contacting surfaces and liquid film, and the geometrical properties of the contacting surfaces, an initial value, b_0, is selected for the radius of liquid film. Next, the pressure distribution due to external loading is obtained using the macro-contact model. The initial value for the film thickness or gap at each radial position is set to be the maximum surface height, $z_{\max}$, within the nominal contact region. The average Reynolds equation (Eq. 3.6) is solved for the liquid film pressure distribution. Since the pressure within the liquid film is negative, it induces tensile stresses between the surfaces. These tensile stresses, which act in surface regions where there is no solid-solid contact, serves to intensify the solid-solid contact pressures. Thus, the liquid film tensile stress and the pressure distribution due to external loading are summed to yield the compressive stress that is inserted into the JS multiscale model to compute the film thickness at each radial position:

$$p_{comp} = p_{ext} + \left| p_f \right| \tag{3.15}$$

The tensile force, which is the integral of liquid film pressure over the wetted region, is calculated and a convergence test is performed on the tensile force. If the tensile force has not converged, the recently calculated values for the film thickness at each radial location are used in the average Reynolds equation to calculate the new liquid film pressure distribution. Once the tensile force has converged, a value of b is calculated based on Eq. (3.13).

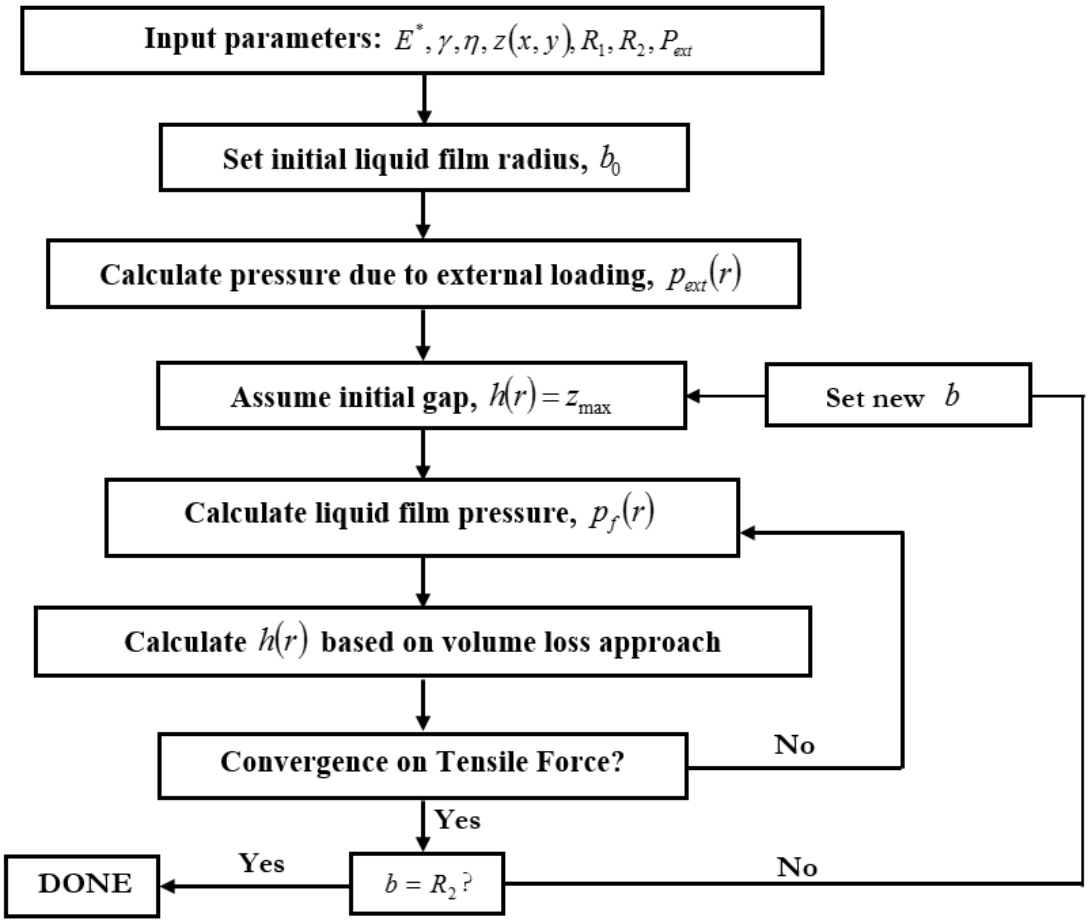

Fig. 3.9 Flowchart of the numerical algorithm.

3.1.7 Results

Results are now presented for the liquid film pressure distribution, p_f, liquid film thickness, h, liquid tensile force, F_t, and liquid flow rate, Q. A table of the material and geometrical properties used for the contacting surfaces and the liquid film is included as Table 3.1. The values for the material properties of contacting surfaces are representative of metal-metal interfaces. The surface tension and dynamic viscosity values of the liquid considered in this work are that of polydimethylsiloxane fluid (PSF-200) at 22.5℃ which is the approximate temperature in the laboratory. For convenience, the contact angles of the liquid film with upper and lower surfaces are assigned values of zero (i.e., $\Theta_{A,B} = 0$). The results are obtained with and without an external load, P_{ext}, acting on the contacting surfaces.

Table 3.1: Reference material and geometrical properties

Name	Symbol	Value
Rigid flat inner radius	R_1	0.1 cm
Rigid flat outer radius	R_2	2 cm
Edge radius	r'	0.1 mm
Effective elastic modulus	E^*	50 GPa
Liquid surface tension	γ	21 mN/m
Liquid dynamic viscosity	η	204.3 mPa.s
r.m.s. surface roughness	σ	0.4 μm

3.1.7.1 Results in the absence of external load

In the case of no external load, the negative fluid pressure distribution within the liquid film induces tensile stresses within the wetted region, which are balanced by the

compressive stresses arising at the solid-solid contact spots. Both the compressive and tensile stresses cause deformation in the contacting surfaces, which leads to a reduction in the spacing between them. The domain of interest is divided into multiple annular elements of width $\Delta r = 0.01$ cm based on the results of a convergence test on the radial grid spacing. The initial liquid film radius, b_0, is selected to be 1 cm. Fig. 3.10 shows the liquid film pressure distribution (Fig. 3.10a), and film thickness (Fig. 3.10b), versus radial position at time $t = 0$.

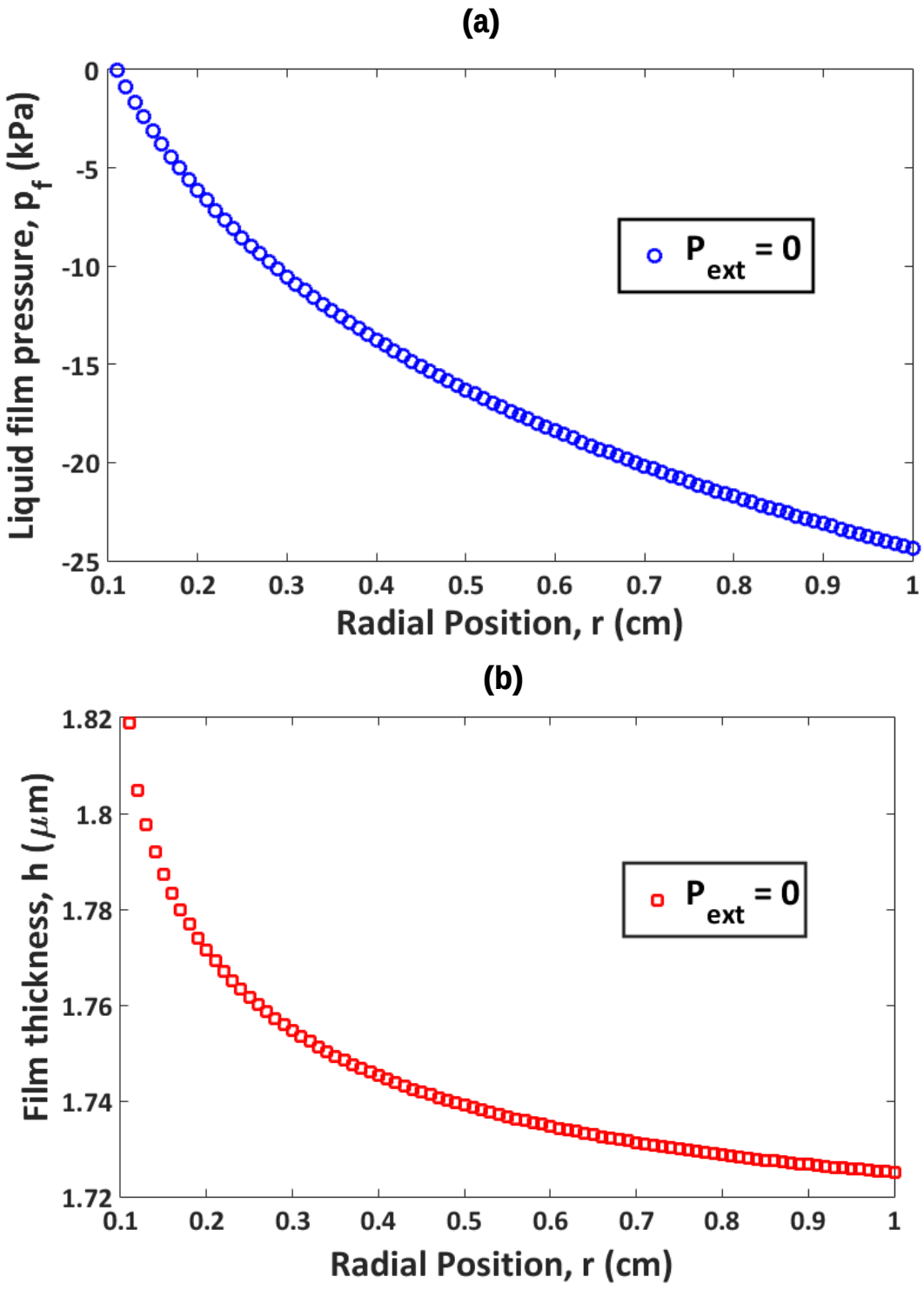

Fig. 3.10 (a) Liquid film pressure, and (b) liquid film thickness versus the radial position at time $t = 0$.

As can be seen from Fig. 3.9a, the pressure distribution starts at zero value (ambient) at the inner radius ($r = R_1 = 0.1$ cm) and decreases to the negative Laplace-Young pressure at the film radius ($r = b_0 = 1$ cm). In Fig. 3.9b, the film thickness, h, is equal to the maximum surface height, $z_{max} = 1.82$ μm, at the inner radius, R_1, where the liquid film pressure is least tensile, and it decreases to its minimum value of 1.725 μm at the liquid film radius, b_0, where the most negative fluid pressure exists.

The results for the liquid tensile force, F_t, and liquid flow rate, Q, between the contacting surfaces versus time, t, are shown in Fig. 3.11. The results are obtained until the liquid film radius reaches 2 cm. As can be seen from Fig. 3.11, the tensile force increases with time as the liquid spreads between the two surfaces. As time passes, the areal coverage of the liquid film increases, which leads to an increase in the tensile force. On the other hand, the liquid flow rate decreases with time.

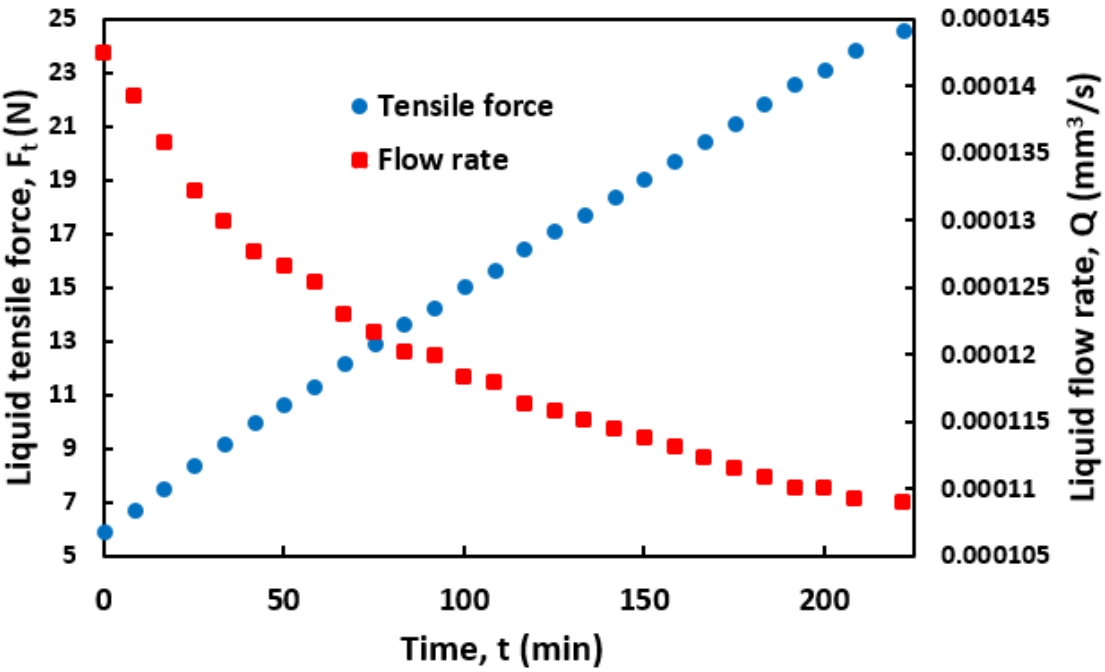

Fig. 3.11 The results for the liquid tensile force and flow rate between the two contacting surfaces versus time.

3.1.7.2 Results in the presence of external load

In this section, liquid flow between contacting surfaces in the presence of external loading is considered. The results are presented for the external loading of $P_{ext} = 20N$ for the reference parameters given in Table 3.1. The contact pressure distribution due to external loading is shown in Fig 3.6. In this case, the pressure distribution due to external loading and the liquid film pressure distribution induces stresses which are balanced by the compressive stresses arising at the solid-solid contact parts. The results for the liquid film pressure distribution and the film thickness at $t = 0$ are shown in Fig. 3.12. The liquid film pressure starts from zero at the inner radius and decreases to the capillary pressure at the outer radius. High values of external pressure due to the edge effect causes a low value of the film thickness at the inner radius, but further away from edge, the film thickness increases. Then, the film thickness decreases due to the effect of the liquid film pressure distribution.

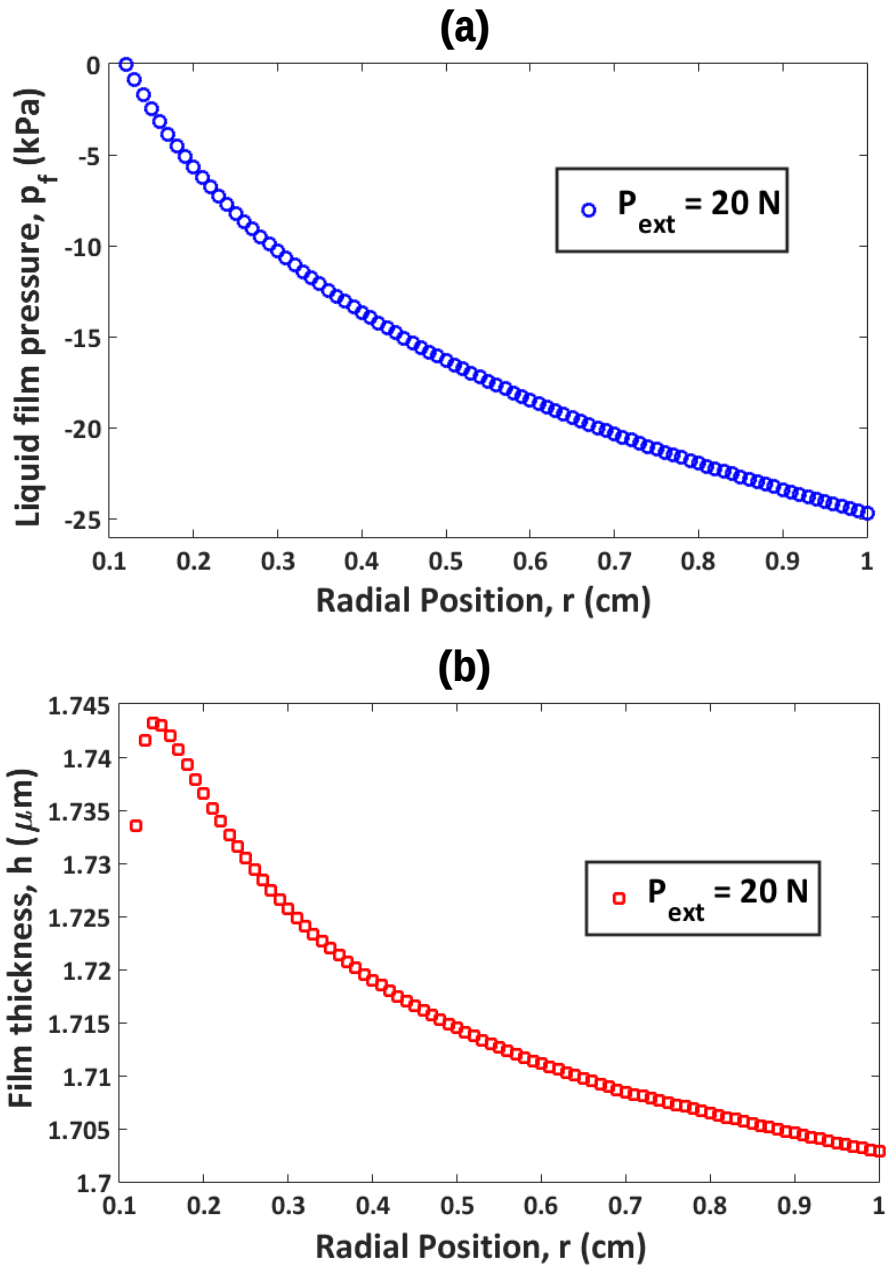

Fig. 3.12 (a) Liquid film pressure, and (b) liquid film thickness versus the radial position at $t = 0$.

3.1.7.3 Parametrical study

A parametric study is performed to investigate the effect of different parameters on the liquid tensile force and liquid flow rate between two contacting surfaces. The

external load, composite surface roughness, and effective elastic modulus were varied according to the ranges listed in Table 3.2. The results are obtained using the same material and geometrical properties given in Table 3.1 except the varied parameter. The results for the maximum tensile force, $F_{t\max}$, and time averaged flow rate, Q_{avg}, versus the external load, P_{ext}, are shown in Fig. 3.13. As observed, the tensile force between the two surfaces increases with external load while the average flow rate generally decreases. Higher external loads cause a reduction in the gap between the two contacting surfaces, which leads to more negative pressures inside the wetted region due to capillary effects and therefore more resistance to liquid flow between the two surfaces.

Table 3.2: Parameter ranges used in the parametric study

Parameter	**Range**
External load	$0 \le P_{ext} \le 500$ N
Composite surface roughness (r.m.s.)	$0.2 \le \sigma \le 2$ μm
Effective elastic modulus	$10 \le E^{*} \le 200$ GPa

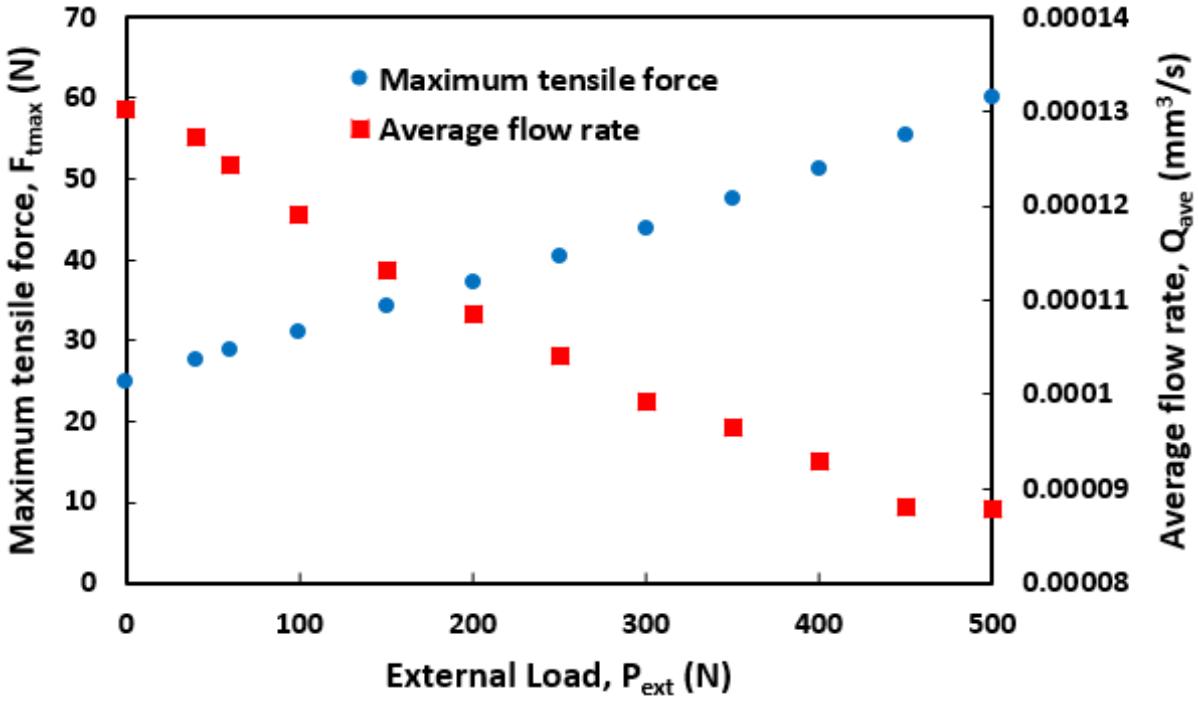

Fig. 3.13 The results for the maximum tensile force and average flow rate versus the external load.

The results for the maximum tensile force, $F_{t\max}$, and average flow rate, Q_{avg}, versus the surface roughness in the absence of external load are shown in Fig. 3.14. The tensile force between the two surfaces increases as the contacting surfaces become smoother while the average flow rate decreases. As the roughness of the surfaces decreases, the gap between the two surfaces also decreases, which leads to more negative pressures while it causes more resistance to the liquid flow.

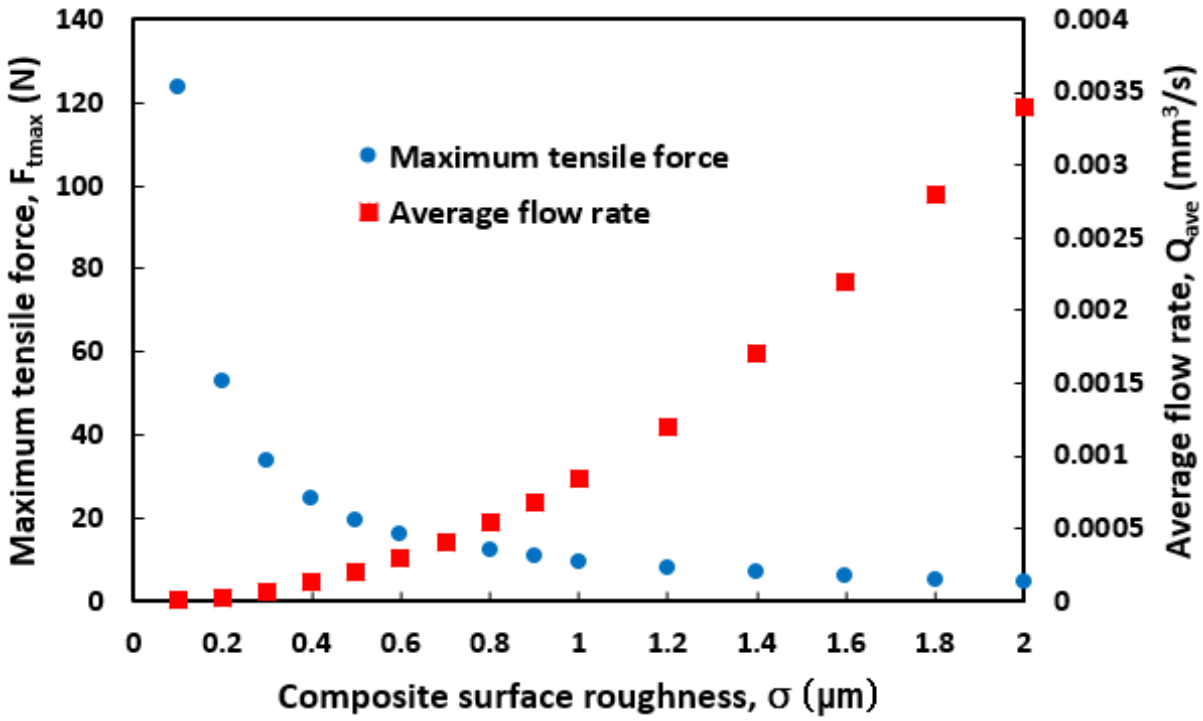

Fig. 3.14 The results for the maximum tensile force and average flow rate versus the composite surface roughness.

The results for the maximum tensile force, $F_{t\max}$, and average flow rate, Q_{avg}, versus the effective elastic modulus, E', in the absence of external load are shown in Fig. 3.15. It can be seen that the tensile force between the two surfaces decreases as the effective elastic modulus increases while the average flow rate decreases. As the elastic modulus of the surfaces decreases, the gap between the two surfaces decreases due to more deformation which leads to more negative pressures inside the wetted region and also more flow resistance.

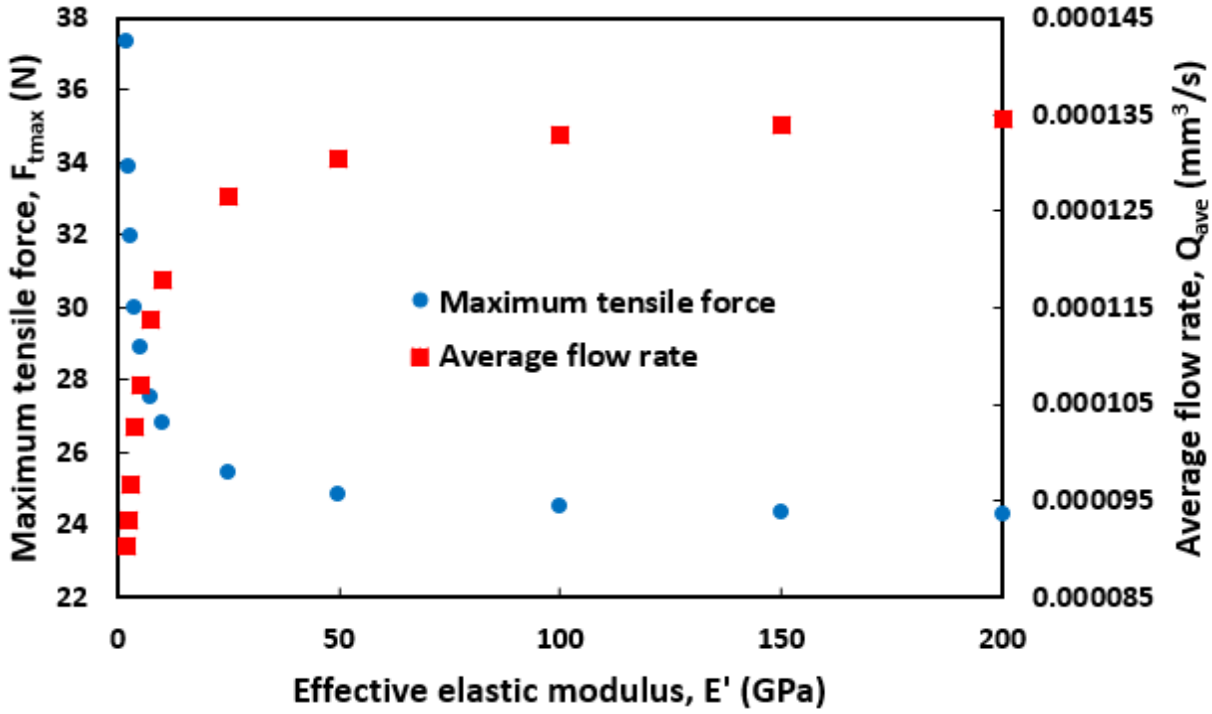

Fig. 3.15 The results for the maximum tensile force and average flow rate versus the effective elastic modulus.

3.1.8 Liquid film spread

A semi-analytical relation for the capillary flow between the two contacting surfaces is developed here. The relation for the rate of change of liquid film radius is given as in Eq. (3.12)

$$\frac{db}{dt} = -\frac{\varphi_{h_b} h_b^2}{12\eta}\left(\frac{dp_f}{dr}\right)_{r=b} \tag{3.16}$$

For the contact between two rigid rough surfaces with separation, h_b, the liquid film pressure distribution can be calculated from Eq. (3.4)

$$p_f(r) = -\frac{\gamma(\cos\theta_A + \cos\theta_B)}{h_b}\frac{\ln(r/R_1)}{\ln(b/R_1)} \tag{3.17}$$

Substituting the derivative of Eq. (3.17) ($\frac{\partial p_f(r)}{\partial r}\Big|_{r=b} = -\frac{\gamma(\cos\theta_A + \cos\theta_B)}{h_b}\frac{1}{b\ln(b/R_1)}$) into Eq. (3.16):

$$\frac{db}{dt} = \frac{\varphi_{h_b} h_b \gamma(\cos\theta_A + \cos\theta_B)}{12\eta b \ln(b/R_1)} \tag{3.18}$$

Rearranging Eq. (3.18), and assuming h_b is a known function of $\gamma, E^*, z_{\max}$, and b:

$$\varphi_{h_b} \frac{b\ln(b/R_1)}{h_b} db = \frac{\gamma(\cos\theta_A + \cos\theta_B)}{12} dt \tag{3.19}$$

Integrating Eq. (3.19), we have

$$t = \frac{12}{\gamma(\cos\theta_A + \cos\theta_B)} \int_{R_1}^{b} \frac{\varphi_{h_{b'}} b' \ln(b'/R_1)}{h_b'} db' \tag{3.20}$$

By performing a parametric study, the following dependency is found for h_b :

$$\frac{h_b}{z_{\max}} = -2049\ (b - R_1)^{-0.3}\left(\frac{\gamma}{E^* z_{\max}}\right)^{0.8} + 1 \tag{3.21}$$

Eq. (3.21) is obtained for the range of parameters $2.5 \le E^* \le 500$ GPa, $1 \le \gamma \le 500$ mN/m, and $4.18 \le z_{\max}/\sigma \le 5.92$. Substituting for h_b from Eq. (3.21) into Eq. (3.20), the liquid film spread between any elastic contacting surfaces can be obtained. The comparison between the $\frac{h_b}{z_{\max}}$ results versus $\frac{\gamma}{E^* z_{\max}}$ obtained from the numerical model and the curve-fit equation (3.21) for different liquid film radius, b, is shown in the Fig. 3.16. The average error between the numerical results and the curve-fit equation is 1.06 %.

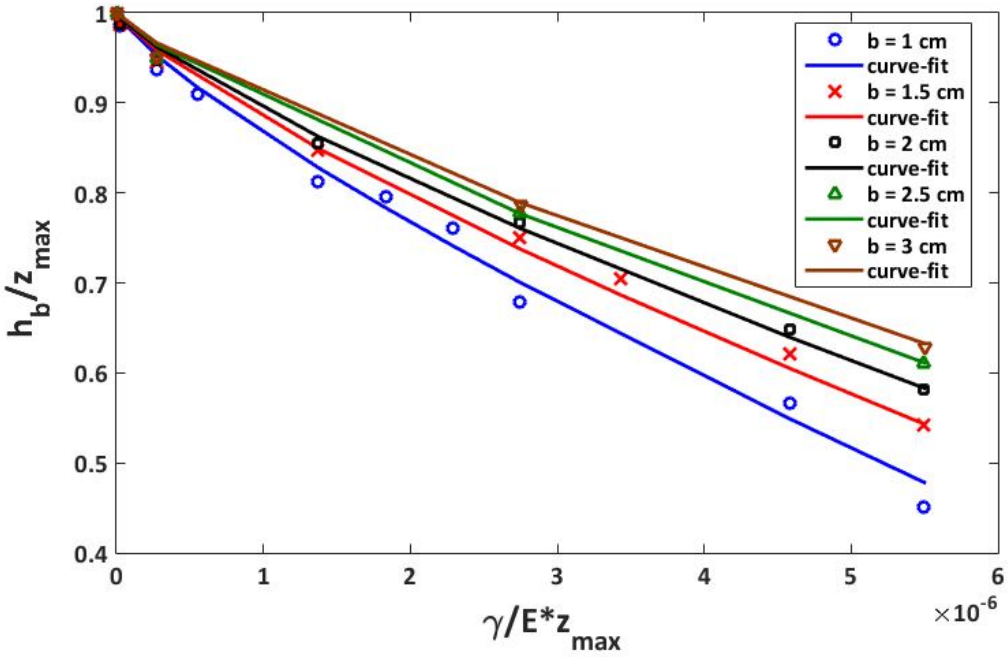

Fig. 3.16 The comparison between results from the numerical model and curve-fit Eq. (3.21).

3.2 Experiments

3.2.1 Liquid film spread

The developed numerical model is validated by comparing the results of the liquid film radius, b, as the liquid spreads between the two surfaces with the experiments. The experimental setup in Fig. 3.17 is the same as section 2.3.2. The setup consists of a camera, light source, several light cords, liquid film, and contacting surfaces. The surface roughness of the metallic disk and the optical flat is measured using a contact stylus profilometer. A scan length of 2.5 cm is set on the profilometer and 13162 surface heights data are obtained for a given scan. Scans are performed on both the optical flat and the metallic disk. These profiles are summed to give a composite profile, which yielded a value of maximum surface height of 8.3 µm and a r.m.s. roughness of 3.4 µm.

Several liquids of varying viscosities are introduced via the central hole in the top optical flat which is in contact with the metallic surface. The relevant properties of the liquids, which are all Pure Silicone Fluids (PSFs), are given in Table 3.3.

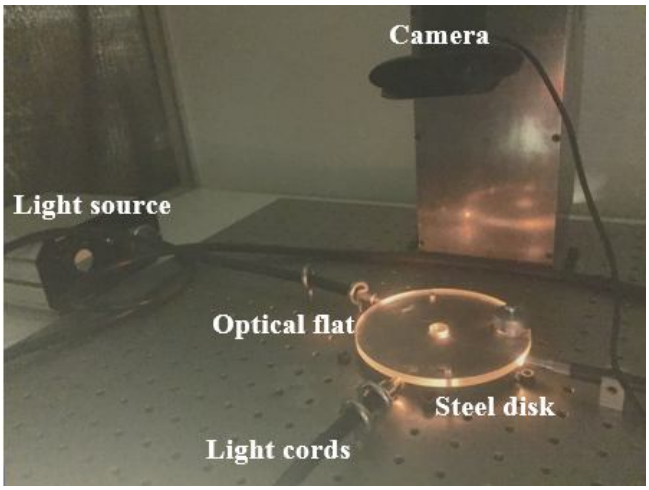

Fig. 3.17 The Experimental setup used to measure the liquid film radius.

The liquid film is introduced via the hole in the optical flat and then begins to spread inside the contact interface due to capillary effect. The images of the spread of a PSF oil at different times are shown in Fig. 3.18. The red color is used to show the front line of the liquid film.

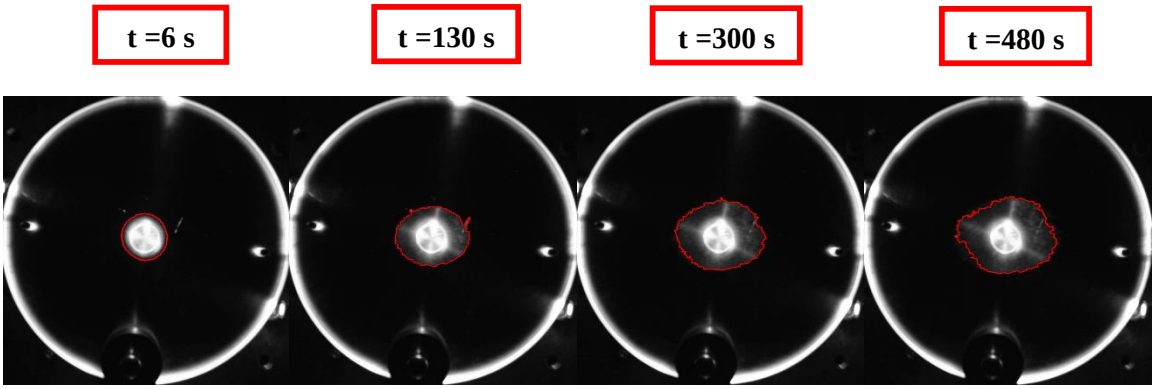

Fig. 3.18 The spread of liquid film between the contacting surfaces.

Table 3.3: Properties of the liquid films (http://www.clearcoproducts.com/pdf/pure-silicone/polydimethylsiloxanes-properties.pdf).

Lubricant	Dynamic viscosity (mPa.s)	Surface tension (mN/m)
PSF-50cSt	50.66	20.8
PSF-100cSt	101.95	20.9
PSF-200cSt	204.32	21.0
PSF-500cSt	512.38	21.1
PSF-1000cSt	1024.76	21.2
PSF-5000cSt	5144.90	21.3

Image processing is performed on the video records to calculate the liquid film radius between the two surfaces at each time step. After finding the x and y coordinates of the various boundary points, the same discretized equation in section 2.3 is used here

$$A_w = \frac{1}{2}\left(\sum_{i=1}^{N}\left(y_i x_{i+1} - x_i y_{i+1}\right)\right) \tag{3.24}$$

Then the liquid film radius corresponding to this wetted area can be easily obtained by

$$b = \sqrt{\frac{A_w}{\pi}}\,.$$

Results for liquid film radius obtained from the experiments are compared with the results of the numerical model (see Fig. 3.19) for six different PSFs ranging in viscosity from 0.051 Pa-s to 5.1 Pa-s (Table 3.3). For the simulations we set the liquid-solid contact angles to zero. We have made no attempt to precisely measure the contact angles. However, upon visual inspection it is clear that the contact angle is quite small so that the corresponding cosine values are very close to unity. As it can be seen the model does a good job of capturing the spread of different liquid films between the two contacting optical flat and the metallic surface.

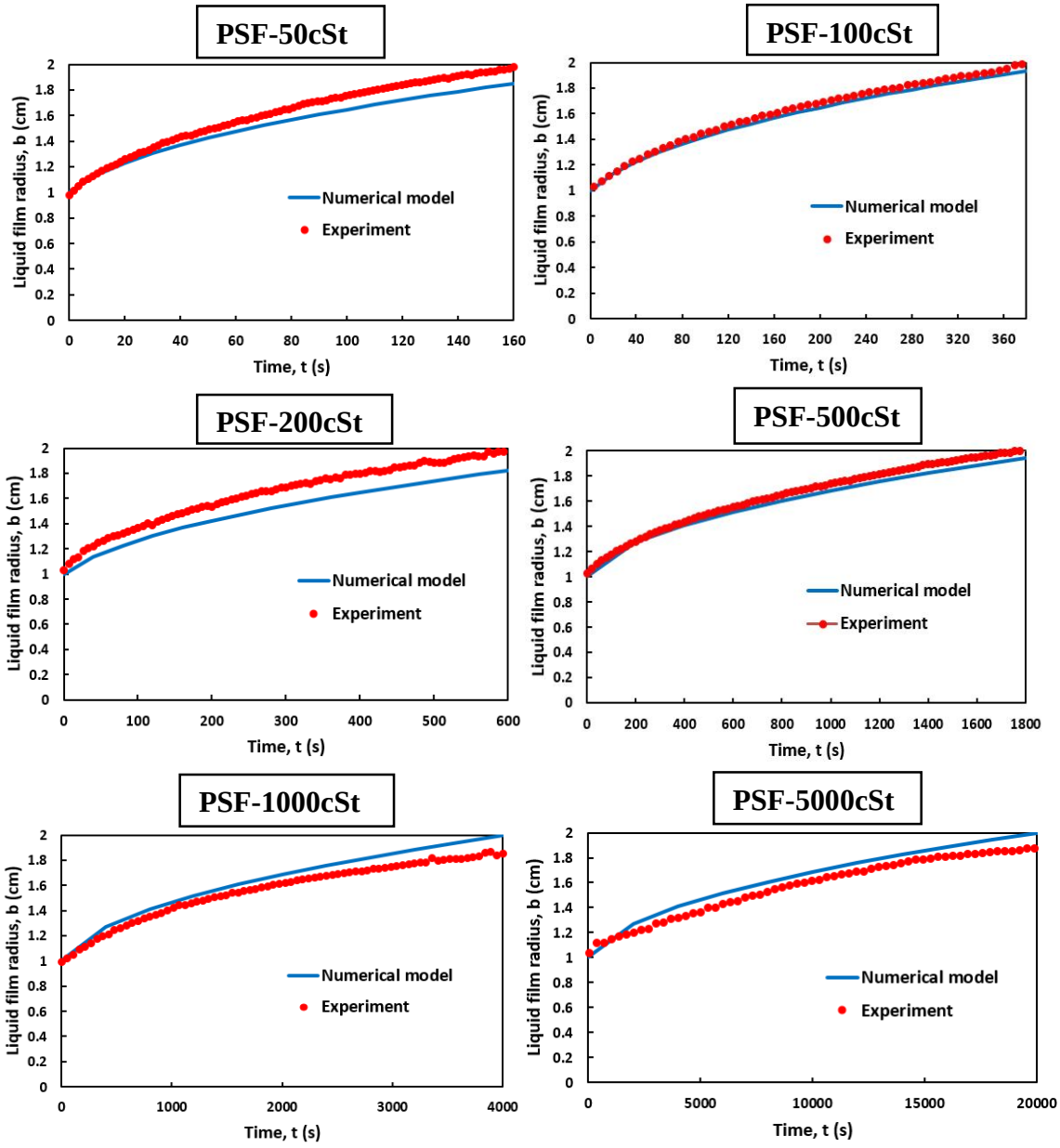

Fig. 3.19 The liquid film radius versus time results as predicted by the numerical model and experiment for different PSF lubricants.

3.3 Conclusions

Liquid-mediated adhesion between contacting surfaces under capillary flow condition is investigated through both numerical and experimental approaches. The numerical model needs to solve equations of elasticity, capillary and lubrication simultaneously. The numerical model consists of three sub-models including a macro- and micro- contact models along with a mixed lubrication model. The results are obtained for the characteristic parameters of the liquid flow using an iterative numerical algorithm. It is shown as the liquid spreads between the two contacting surfaces, the liquid tensile force increases while the liquid flow rate decreases with time in the case of no external load. As the external loading increases, the tensile force increases while the average liquid flow rate decreases. Higher tensile forces and lower flow rates happen for smoother surfaces. For more flexible surfaces, higher tensile forces and lower flow rates happen. A semi analytical equation is developed for the capillary-driven flow between two contacting surfaces. The spread of liquid film between the contacting surfaces is visualized using a digital camera and the spread of the liquid film is measured as a function of time by using image processing on the images recorded. Good agreement between the numerical model and the experimental results is observed.

CHAPTER 4

CONCLUSIONS AND RECOMMENDATIONS

The liquid-mediated adhesion between contacting rough surfaces is studied through both numerical and experimental approaches. Liquid-mediated adhesion under two different conditions is considered: (1) no-flow condition or static condition, where the liquid film has a uniform pressure throughout, and (2) capillary flow condition, where a pressure gradient exists inside the liquid film. In order to model the compressive stresses that arise at solid-solid contact spots, two different contact models, i.e.: spectral or multiscale and deterministic, are employed.

1. For the static condition, results are obtained for the tensile force, average spacing, liquid film spread, and contact area for different material and geometrical properties of the contacting surfaces and liquid film. It is shown under certain circumstances, a contact instability could happen, where the tensile stresses dominate the compressive stresses. This condition is called surface collapse, whereby there is an unexpected upward jump in the tensile force, liquid film spread, and contact area, as well as a downward jump in the average gap. Based on the normalization, an empirical relation for the adhesion parameter at the point of instability is obtained which is a combination of the material and geometrical properties of the contacting rough surfaces and the liquid film. It is shown that the critical adhesion parameter, Γ_{cr}, depends on the non-dimensional liquid volume,

V_0^*, non-dimensional external load, P^*, and the non-dimensional maximum height, $z_{\max}^*$ as in $\Gamma_{cr} = \dfrac{1}{\left(8.94V_0^* + 17.15\right) z_{\max}^{*\,-1.55V_0^{*0.11}} P^{*0.85}} + \dfrac{1}{0.011\, V_0^{*0.32}\, z_{\max}^{*\,2.87}}$.

Also, tensile force between the two contacting surfaces are measured experimentally through both a pull-off test and a friction force test. Two different experimental setups are used to measure the pull-off and friction forces between different contacting surfaces in the presence of different amount of liquid volume. It is shown as the liquid film volume increases between the two surfaces, the tensile force also increases. The results showed that the tensile force is higher between the smoother surfaces. The liquid film spread or wetted area between the surfaces is also measured by performing image processing on the images captured by a digital camera from the interface. The results are obtained for different contacting surfaces and different amount of intervening liquid film. The results suggested that the wetted area increases as the liquid film volume increases between the surfaces, and also higher wetted area happens between smoother surfaces due to small spacing between them. The experimental results are compared with results of the numerical model. Good agreement is observed between the two approaches.

2. For the capillary flow condition, it was shown as the liquid film spreads between the two contacting surfaces, the liquid tensile force increases while the liquid flow rate decreases with time. As the external loading increases, the tensile force increases while the average flow rate decreases. Higher tensile forces and lower flow rates happen for smoother surfaces. For more flexible surfaces, higher tensile forces and lower flow rates happen. A semi analytical equation is developed for the capillary-driven flow between

two contacting surfaces. The spread of liquid film is visualized using a digital camera, and the wetted area is measured as a function of time. The results are compared with results of the numerical model. Good agreement between the numerical model and the experimental results is observed.

REFERENCES

1. Maboudian, R., Howe, R.T.: Critical review: adhesion in surface micromechanical structures. Journal of Vacuum Science & Technology B **15**(1), 1-20 (1997).

2. Maboudian, R.: Surface processes in MEMS technology. Surface Science Reports **30**(6), 207-269 (1998).

3. Komvopoulos, K.: Adhesion and friction forces in microelectromechanical systems: mechanisms, measurement, surface modification techniques, and adhesion theory. Journal of adhesion science and technology **17**(4), 477-517 (2003).

4. van Spengen, W.M.: MEMS reliability from a failure mechanisms perspective. Microelectronics Reliability **43**(7), 1049-1060 (2003).

5. Raccurt, O., Tardif, F., d'Avitaya, F.A., Vareine, T.: Influence of liquid surface tension on stiction of SOI MEMS. Journal of Micromechanics and Microengineering **14**(7), 1083 (2004).

6. Koppaka, S.B., Phinney, L.M.: Release processing effects on laser repair of stiction-failed microcantilevers. Microelectromechanical Systems, Journal of **14**(2), 410-418 (2005).

7. Wu, D., Fang, N., Sun, C., Zhang, X.: Stiction problems in releasing of 3D microstructures and its solution. Sensors and Actuators A: Physical **128**(1), 109-115 (2006).

8. Maboudian, R., Carraro, C.: Surface chemistry and tribology of MEMS. Annu. Rev. Phys. Chem. **55**, 35-54 (2004).

9. Zhu, L., Xu, J., Zhang, Z., Hess, D.W., Wong, C.: Lotus effect surface for prevention of microelectromechanical system (MEMS) stiction. In: Electronic Components and Technology Conference, 2005. Proceedings. 55th 2005, pp. 1798-1801. IEEE

10. Zhu, L., Xiu, Y., Xu, J., Hess, D.W., Wong, C.: Optimizing geometrical design of superhydrophobic surfaces for prevention of microelectromechanical system (MEMS) stiction. In: Electronic Components and Technology Conference, 2006. Proceedings. 56th 2006, p. 7 pp. IEEE

11. Sammoura, F., Hancer, M., Yang, K.: The Effect of Surface Chemistry on MEMS Stiction in an Ultralow-Humidity Environment. Microelectromechanical Systems, Journal of **20**(2), 522-526 (2011).

12. Liu, C., Chou, B.C., Tsai, R.-F., Shen, N.Y., Chen, B.S., Cheng, E.C., Tuan, H.C., Kalnitsky, A., Cheng, S., Lin, C.-H.: MEMS technology development and manufacturing in a CMOS foundry. In: Solid-State Sensors, Actuators and Microsystems Conference (TRANSDUCERS), 2011 16th International 2011, pp. 807-810. IEEE

13. Hariri, A., Zu, J., Ben Mrad, R.: Modeling of wet stiction in microelectromechanical systems (MEMS). Microelectromechanical Systems, Journal of **16**(5), 1276-1285 (2007).

14. Bhushan, B.: Tribology and mechanics of magnetic storage devices. Springer Science & Business Media, (2012)

15. Bullock, J.M., Drechsler, P., Federle, W.: Comparison of smooth and hairy attachment pads in insects: friction, adhesion and mechanisms for direction-dependence. Journal of Experimental Biology **211**(20), 3333-3343 (2008).

16. Zheng, J., Streator, J.: A liquid bridge between two elastic half-spaces: A theoretical study of interface instability. Tribology Letters **16**(1-2), 1-9 (2004).

17. Zheng, J., Streator, J.L.: A micro-scale liquid bridge between two elastic spheres: Deformation and stability. Tribology Letters **15**(4), 453-464 (2003).

18. Zheng, J., Streator, J.L.: A generalized formulation for the contact between elastic spheres: applicability to both wet and dry conditions. Journal of tribology **129**(2), 274-282 (2007).

19. Matthewson, M., Mamin, H.: Liquid mediated adhesion of ultra-flat solid surfaces. In: MRS Proceedings 1988, vol. 1. Cambridge Univ Press

20. Megias-Alguacil, D., Gauckler, L.J.: Capillary forces between two solid spheres linked by a concave liquid bridge: regions of existence and forces mapping. AIChE journal **55**(5), 1103-1109 (2009).

21. Matthewson, M.: Adhesion of spheres by thin liquid films. Philosophical Magazine A **57**(2), 207-216 (1988).

22. Persson, B.: Capillary adhesion between elastic solids with randomly rough surfaces. Journal of Physics: Condensed Matter **20**(31), 315007 (2008).

23. Rostami, A., Streator, J.L.: Study of liquid-mediated adhesion between 3D rough surfaces: A spectral approach. Tribology International **84**(0), 36-47 (2015). doi:http://dx.doi.org/10.1016/j.triboint.2014.11.019

24. Rostami, A., Streator, J.L.: A Deterministic Approach to Studying Liquid-Mediated Adhesion Between Rough Surfaces. Tribology Letters **58**(1), 1-13 (2015).

25. DelRio, F.W., Dunn, M.L., de Boer, M.P.: Capillary adhesion model for contacting micromachined surfaces. Scripta Materialia **59**(9), 916-920 (2008).

26. Wang, L., Régnier, S.: A More General Capillary Adhesion Model Including Shape Index: Single-Asperity and Multi-Asperity Cases. Tribology Transactions **58**(1), 106-112 (2015).

27. Peng, Y., Guo, Y., Hong, Y.: An adhesion model for elastic-contacting fractal surfaces in the presence of meniscus. Journal of Tribology **131**(2), 024504 (2009).

28. De Boer, M., De Boer, P.: Thermodynamics of capillary adhesion between rough surfaces. Journal of colloid and interface science **311**(1), 171-185 (2007).

29. De Boer, M.: Capillary adhesion between elastically hard rough surfaces. Experimental mechanics **47**(1), 171-183 (2007).

30. Men, Y., Zhang, X., Wang, W.: Capillary liquid bridges in atomic force microscopy: Formation, rupture, and hysteresis. The Journal of chemical physics **131**(18), 184702 (2009).

31. Butt, H.-J., Barnes, W.J.P., Del Campo, A., Kappl, M., Schönfeld, F.: Capillary forces between soft, elastic spheres. Soft Matter **6**(23), 5930-5936 (2010).

32. Roemer, D.B., Johansen, P., Pedersen, H.C., Andersen, T.O.: Fluid stiction modeling for quickly separating plates considering the liquid tensile strength. Journal of Fluids Engineering **137**(6), 061205 (2015).

33. Marmur, A.: Tip-surface capillary interactions. Langmuir **9**(7), 1922-1926 (1993).

34. Poon, C.Y., Bhushan, B.: Numerical contact and stiction analyses of Gaussian isotropic surfaces for magnetic head slider/disk contact. Wear **202**(1), 68-82 (1996).

35. Tian, X., Bhushan, B.: The micro-meniscus effect of a thin liquid film on the static friction of rough surface contact. Journal of Physics D: Applied Physics **29**(1), 163 (1996).

36. Streator, J.: A model of mixed lubrication with capillary effects. Tribology Series **40**, 121-128 (2002).

37. Streator, J.L., Jackson, R.L.: A model for the liquid-mediated collapse of 2-D rough surfaces. Wear **267**(9), 1436-1445 (2009).

38. Streator, J.L.: A model of liquid-mediated adhesion with a 2D rough surface. Tribology International **42**(10), 1439-1447 (2009).

39. Streator, J.: Analytical Instability Model for the Separation of a Sphere From a Flat in the Presence of a Liquid Film. In: ASME/STLE 2004 International Joint Tribology Conference 2004, pp. 1217-1224. American Society of Mechanical Engineers

40. Cai, S., Bhushan, B.: Meniscus and viscous forces during separation of hydrophilic and hydrophobic surfaces with liquid-mediated contacts. Materials Science and Engineering: R: Reports **61**(1), 78-106 (2008).

41. Bhushan, B., Dugger, M.: Liquid-mediated adhesion at the thin film magnetic disk/slider interface. ASME J. Tribol **112**, 217-223 (1990).

42. Yang, S.H., Nosonovsky, M., Zhang, H., Chung, K.-H.: Nanoscale water capillary bridges under deeply negative pressure. Chemical Physics Letters **451**(1), 88-92 (2008).

43. Yang, S., Zhang, H., Nosonovsky, M., Chung, K.-H.: Effects of contact geometry on pull-off force measurements with a colloidal probe. Langmuir **24**(3), 743-748 (2008).

44. Nosonovsky, M., Bhushan, B.: Capillary effects and instabilities in nanocontacts. Ultramicroscopy **108**(10), 1181-1185 (2008).

45. Rabinovich, Y.I., Esayanur, M.S., Johanson, K.D., Adler, J.J., Moudgil, B.M.: Measurement of oil-mediated particle adhesion to a silica substrate by atomic force microscopy. Journal of adhesion science and technology **16**(7), 887-903 (2002).

46. Rabinovich, Y.I., Adler, J.J., Esayanur, M.S., Ata, A., Singh, R.K., Moudgil, B.M.: Capillary forces between surfaces with nanoscale roughness. Advances in colloid and interface science **96**(1), 213-230 (2002).

47. Rabinovich, Y.I., Esayanur, M.S., Moudgil, B.M.: Capillary forces between two spheres with a fixed volume liquid bridge: theory and experiment. Langmuir **21**(24), 10992-10997 (2005).

48. Tian, H., Matsudaira, T.: The role of relative humidity, surface roughness and liquid build-up on static friction behavior of the head/disk interface. Journal of tribology **115**(1), 28-35 (1993).

49. Ata, A., Rabinovich, Y.I., Singh, R.K.: Role of surface roughness in capillary adhesion. Journal of adhesion science and technology **16**(4), 337-346 (2002).

50. Xiao, X., Qian, L.: Investigation of humidity-dependent capillary force. Langmuir **16**(21), 8153-8158 (2000).

51. Grobelny, J., Pradeep, N., Kim, D.-I., Ying, Z.: Quantification of the meniscus effect in adhesion force measurements. Applied physics letters **88**(9), 091906 (2006).

52. Jackson, R.L., Streator, J.L.: A multi-scale model for contact between rough surfaces. Wear **261**(11), 1337-1347 (2006).

53. Adamson, A.W., Gast, A.P.: Physical chemistry of surfaces. (1967).

54. Johnson, K., Greenwood, J., Higginson, J.: The contact of elastic regular wavy surfaces. International journal of mechanical sciences **27**(6), 383-396 (1985).

55. Rostami, A., Jackson, R.L.: Predictions of the average surface separation and stiffness between contacting elastic and elastic–plastic sinusoidal surfaces. Proceedings of the Institution of Mechanical Engineers, Part J: Journal of Engineering Tribology **227**(12), 1376-1385 (2013).

56. Green, C.K., Streator, J.L., Haynes, C., Lara-Curzio, E.: A Computational Leakage Model for Solid Oxide Fuel Cell Compressive Seals. Journal of fuel cell science and technology **8**(4), 041003 (2011).

57. Johnson, K.L., Johnson, K.L.: Contact mechanics. Cambridge university press, (1987)

58. Whitehouse, D.J., Archard, J.: The properties of random surfaces of significance in their contact. Proceedings of the Royal Society of London. A. Mathematical and Physical Sciences **316**(1524), 97-121 (1970).

59. Garcia, N., Stoll, E.: Monte Carlo calculation for electromagnetic-wave scattering from random rough surfaces. Physical review letters **52**(20), 1798 (1984).

60. Johnson, K.: Contact mechanics, 1985. Cam-bridge University Press, Cambridge (1974).

61. Love, A.E.H.: The stress produced in a semi-infinite solid by pressure on part of the boundary. Philosophical Transactions of the Royal Society of London. Series A, Containing Papers of a Mathematical or Physical Character, 377-420 (1929).

62. Webster, M., Sayles, R.: A numerical model for the elastic frictionless contact of real rough surfaces. Journal of Tribology **108**(3), 314-320 (1986).

63. Zheng, J.: Effects of capillarity on the mechanical stability of small-scale interfaces. (2004).

64. Washburn, E.W.: The dynamics of capillary flow. Physical review **17**(3), 273 (1921).

65. Fisher, L.R., Lark, P.D.: An experimental study of the Washburn equation for liquid flow in very fine capillaries. Journal of Colloid and Interface Science **69**(3), 486-492 (1979).

66. Van Honschoten, J., Escalante, M., Tas, N., Jansen, H., Elwenspoek, M.: Elastocapillary filling of deformable nanochannels. Journal of applied physics **101**(9), 094310 (2007).

67. Van Honschoten, J., Escalante, M., Tas, N., Elwenspoek, M.: Formation of liquid menisci in flexible nanochannels. Journal of colloid and interface science **329**(1), 133-139 (2009).

68. Dimitrov, D., Milchev, A., Binder, K.: Capillary rise in nanopores: molecular dynamics evidence for the Lucas-Washburn equation. Physical review letters **99**(5), 054501 (2007).

69. Czachor, H.: Applicability of the Washburn theory for determining the wetting angle of soils. Hydrological processes **21**(17), 2239-2247 (2007).

70. Cerepi, A., Humbert, L., Burlot, R.: Dynamics of capillary flow and transport properties in porous media by time-controlled porosimetry. Colloids and Surfaces A: Physicochemical and Engineering Aspects **206**(1), 425-444 (2002).

71. Hamrock, B.J., Schmid, S.R., Jacobson, B.O.: Fundamentals of fluid film lubrication. CRC press, (2004)

72. Patir, N., Cheng, H.: An average flow model for determining effects of three-dimensional roughness on partial hydrodynamic lubrication. Journal of Tribology **100**(1), 12-17 (1978).